Optimizing Lipid Nanoparticles for Fetal Gene Delivery In Vitro, Ex Vivo, and Aided by Machine Learning

by

Amr Abostait

A thesis submitted to the Faculty of Graduate Studies of

The University of Manitoba

in partial fulfillment of the requirements of the degree of

MASTER OF SCIENCE

College of Pharmacy, Rady Faculty of Health Sciences

University of Manitoba

Winnipeg, MB, CANADA.

Abstract

Background:

There is a clinical need to develop lipid nanoparticles (LNPs) to deliver prenatal therapies to the developing fetus during pregnancy. The aim of these therapies is to restore normal fetal development and prevent irreversible conditions after birth. As a first step, LNPs need to be optimized for transplacental transport, safety, and transfection efficiency in fetal cells.

Methods:

We developed and characterized a library of LNPs of varying compositions and used machine learning (ML) models to delineate the determinants of LNPs size and zeta potential. Utilizing different in vitro placental models with the help of the Random Forest algorithm, we studied the features driving percentage LNPs transport and kinetics, using a dataset of 18 input features encompassing 48 different transport experiments. We further evaluated the LNPs for safety and transfection efficiency in placental trophoblasts and fetal lung fibroblasts. Finally, we assessed toxicity of the LNPs in a tracheal occlusion fetal lung explant ex-vivo model.

Results:

LNPs showed little to no toxicity to fetal and placental cells. Immunoglobin G (IgG) orientation on the surface of LNPs, PEGylated lipids, and ionizable lipids had significant effects on placental transport. The Random Forest algorithm identified the top features driving LNPs placental transport percentage and kinetics; zeta potential emerged as one of the top driving features. Building on the ML model results, we developed new LNPs formulations to further optimize the transport leading to a 622% increase in transport. To induce preferential siRNA transfection of fetal lungs, we further optimized cationic lipid percentage and the lipid-to-siRNA ratio. Studying LNPs in an integrated placental and fetal lung fibroblasts model showed a strong correlation between zeta potential and fetal lung transfection and ensured the integrity of the LNPs following transplacental transport. Finally, the optimized formulations appeared to be safe in ex vivo fetal lungs as indicated by insignificant changes in apoptosis (Caspase-3) and proliferation (Ki67) markers.

Conclusion:

We have optimized an LNPs formulation that is safe, with high transplacental transport and preferential transfection in fetal lung cells. Our research findings represent an important step toward establishing the safety and effectiveness of LNPs for gene delivery to the fetal organs.

Preface

This thesis has been written in the grouped manuscript style (sandwich thesis). It includes submitted and published manuscripts. Amr Abostait is the first author on these manuscripts. He conducted and gathered most of the work presented in this MSc thesis. The first chapter of the thesis provides an introduction about the topic and highlights the gaps we attempted to address in chapter two and three. Chapter two represents a submitted manuscript that's currently under review at the Journal of Controlled Release. While chapter three represents a published manuscript at the Molecular Pharmaceutics journal. Finally, the fourth chapter gives a conclusion and summary for what has been achieved in this work. The thesis follows the AMA (American Medical Association) citation style.

Acknowledgements

I offer my sincerest gratitude to my advisor, Dr. Hagar Labouta, for her unwavering support and for providing guidance, insights, and mentorship at various stages of my degree. I am also deeply thankful to my co-supervisor, Dr. Richard Keijzer, for his expert insights and continuous support throughout the project. Additionally, I express special thanks to my advisory committee members, Dr. Ted Lakowski and Dr. Francis Lin, for their valuable feedback and encouragement.

I'm grateful for the outstanding research teams and collaborators who enriched this project. Many thanks to the Keijzer Lab members at CHRIM—Dr. Andrew Tse, Dr. Yuichiro Miyake, Dr. Arzu Ozturk, Mr. Daywin Patel, and Jackie Wang—for their training and the fruitful discussions we had. Special thanks to the Allen Lab members at the University of Toronto—Dr. Christine Allen, Zeqing Bao, and Dr. Anish Hiresha Verma—who inspired and led the machine learning work. I also extend my gratitude to Dr. Tina Buerki for providing essential research materials. Finally, thanks to the amazing core specialists at Unity Health Toronto— Dr. Caterina Di Ciano-Oliveira, Mr. Xiaofeng Lu, and Dr. Dario Bogojevic—for their training and support with various techniques.

We also acknowledge the financial support by New Frontiers Research Fund – Exploration Grant NFRFE-2019-00210), SickKids Foundation in partnership with the Canadian Institutes of Health Research (NI22-1088R), and the Natural Sciences and Engineering Research Council (NSERC Discovery Grant-RGPIN-2020-05679 and NSERC RTI-2021-00374). I am grateful for the financial support provided by the Rady Faculty of Health Science Master Studentship, Research Manitoba Master Studentship, Women's Health Research Foundation of Canada Graduate Scholarship, and St. Michael's Hospital Research Training Centre Award.

Furthermore, I was glad to share my research journey with my colleagues at Labouta Lab and the College of Pharmacy. I would like to extend special thanks to Jack, Mahmoud, Yasmin, Luis, Klaidi, Laila, and Alkyah for their camaraderie and support.

Lastly, I am profoundly thankful to my parents (Mostafa Abostait & Soheir Sobeh), sister (Marwa), mother-in-law (Sanaa Elshehawy), brothers (Ahmed & Hasanien), nephews (Ziad, Ibrahim, and Eyad), nieces (Karma & Lujy), my dear friends (Skawa & Fayez), and of course my dear lovely wife (Yomna) for their love, support, and encouragement that continues to carry me forward in life.

Dedication

To my beloved wife, “Yomna Zidan”,

Your love, endless patience, and support have been my greatest source of strength throughout this journey. This thesis is dedicated to you, with all my love and gratitude.

Table of Contents:

List of Tables

List of Figures

List of Abbreviations

LNPs - Lipid Nanoparticles

NPs - Nanoparticles

IgG - Immunoglobulin G

FDA - Food and Drug Administration

CDH - Congenital Diaphragmatic Hernia

mRNA - Messenger ribonucleic acid

siRNA - Small Interfering RNAs

miRNA - Micro RNA

HUVEC - Human Umbilical Vein Endothelial Cells

FITC - Fluorescein isothiocyanate

AF488 - Alexa Flour 488

AF647 - Alexa Flour 647

ZO-1 - Zonula occludens-1

FcRn- Neonatal fragment crystallizable receptor

ML- Machine Learning

SHAP- Shapley Additive Explanations

RF- Random Forest

PEG- Polyethylene glycol

SORT- Selective organ targeting

Chapter I: Introduction

1.1 Fetal Gene Therapies

Congenital diseases are a considerable challenge in maternal-fetal health and one of the leading causes of infant mortality and lifelong morbidity [1]. Congenital diseases are characterized by phenotypic changes due to genetic mutations, chromosomal abnormalities, epigenetic changes, or environmental factors [2]. Additionally, there have been promising advancements in Magnetic Resonance Imaging (MRI), ultrasonography, and genetic testing, which enable early diagnosis of congenital diseases [1,3]. Therefore, early interference using prenatal gene therapies could revert the course of the disease and prevent irreversible damage [4].

Besides the obvious benefit of early interference, prenatal gene therapies pose several advantages from the gene delivery perspective, such as the small fetus size, immunological immaturity, and abundant populations of stem cells [5]. However, direct injection of nucleic acids could fail due to multiple biological factors, including the rapid degradation by extracellular DNAases and RNAases. Besides, nucleic acid molecules can't cross the plasma membrane and exit the endosomes to reach the site of action in the cytoplasm or the nucleus due to their large sizes and anionic charge [6]. Also, the immunity issues arising from triggering the interaction with toll-like receptors (TLRs) that lead to cytokine release and inflammatory responses [7]. So, gene delivery vehicles are required to offer shielding from degradation enzymes and the immune system while achieving tissue-specific delivery and endosomal escape.

The current landscape of gene delivery vehicles is divided between viral and non-viral vectors [8]. Viral vectors exhibit high efficiency in tissue-specific targeting and delivering nucleic acids to the cytoplasm or the nucleus. They have been optimized over millions of years by evolution. Retroviruses, Adenoviruses, Lentiviruses, and Adeno-associated viruses are the most common viral vectors. They mainly differ in the type and size of genetic cargo and the types of cells they can transfect [1,9]. However, these viral vectors pose mutagenicity and immunogenicity risks, which make them more challenging for prenatal gene therapy [10].

On the other hand, non-viral vectors such as polymeric or lipid nanoparticles (NPs) have lower risk and a reproducible and more scalable manufacturing process [6]. Ullrich et al have shown the ability of polymeric nanoparticles to deliver micro-RNA to the fetal lung [11]. Other studies have explored the potential of lipid nanoparticles in delivering messenger RNA (mRNA) to the fetal lung and liver [12,13].

1.2 Lipid Nanoparticles

Lipid nanoparticles (LNPs) have become the gold-standard for nucleic acids delivery, with four products already reaching the market and tens in different stages of clinical trials [14]. Chronologically sorted by their FDA approval date, the four FDA-approved LNPs-based products are: Onpattro, Pfizer–BioNTech COVID-19 vaccine, Moderna COVID-19 vaccine, and Moderna respiratory syncytial virus (RSV) vaccine [15,16]. The LNPs formulations are composed of four different classes of lipids: ionizable lipid, PEGylated lipid, helper lipid and cholesterol [17]. These lipids could be of different types or molar percentages, which affect the LNPs physicochemical properties and biological behavior.

The phospholipid is a class of lipids that's composed of a polar head and non-polar tail (Figure 1A); the molecular structure of both has great influence on the properties of the lipid. For example, the

tail length and unsaturation greatly impact the phase transition temperature (T_m). T_m is the temperature at which the lipid changes from the ordered gel phase to the disordered liquid crystalline phase [18]. As the lipid tail length increases, the hydrophobic interaction between the tails increases leading to higher T_m as shown when comparing DSPE to DPPE and in Figure (1B). On the other hand, the tail unsaturation leads to a kink in the structure that disrupt the assembly with neighbouring lipids and increase the distance between them (Figure 1A). And since the London dispersion forces that governs the interaction is inversely proportional to distance between the interacting lipid tails to the power of six (r^6) [19], this leads to a huge decrease in T_m, as seen when comparing T_m DOPE (unsaturated lipid tail) to DSPE (saturated lipid tail) in Figure 1B.

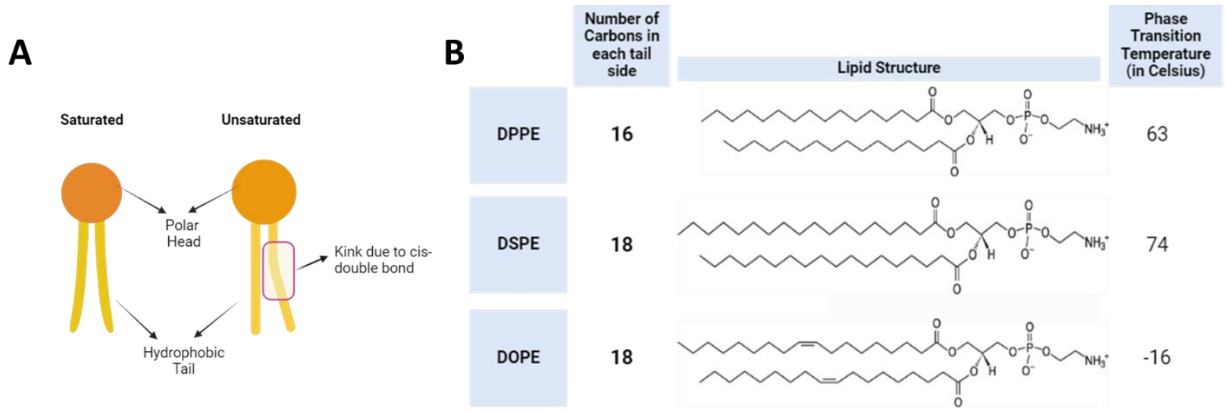

Figure 1: *The Lipid Structure and Properties. (A) Schematic Structure of Phospholipid; showing the difference between saturated and unsaturated lipids. (B) Different lipid structures and their phase transition temperature; showing the effect of tail length and unsaturation. DPPE stands for 1,2-dipalmitoyl-sn-glycero-3-phosphoethanolamine; DSPE stands for 1,2-distearoyl-sn-glycero-3-phosphoethanolamine; DOPE stands for 1,2-dioleoyl-sn-glycero-3-phosphoethanolamine. Created with BioRender.com.*

The first and most fundamental class of lipids in the LNPs is the ionizable lipid which plays the major role in transfection by enhancing endosomal escape. Increasing endosomal escape is essential for successful nucleic acid therapeutics; either for efficient silencing using siRNA, or protein translation using mRNA. Ionizable lipids have a pKa in the range of 6-7, so their head group is neutral at physiological pH, but positively charged in the endosomal acidic pH [20,21]. Several concepts exist to explain the endosomal escape of LNPs including the concept of lipid polymorphism (Figure 2A).

Amphiphilic molecules, such as phospholipids, can self-assemble into a variety of different structures upon dispersion in water. This behavior has been known as lipid polymorphism which has been explained by the "Molecular Shape" theory [22]. As shown in Figure 2A, molecules with large headgroup area and small tail area have a cone geometry and tend to self-assemble into micelles. On the other hand, molecules with equal head and tail areas have a cylindrical geometry and prefer the bilayer assembly. Finally, the molecules with bigger tail area have an inverted cone geometry and assemble into inverted micelles or inverted hexagonal structures [23].

Endosomal escape derived by lipid polymorphism starts by lipids exchange between the LNPs and the endosomal membrane [24]. Thereafter, the ionizable lipid will get positively charged at acidic endosomal pH, leading to stronger interaction with the negatively charged endosomal membrane [25]. Finally, this interaction will change the geometry of the lipid leading to bilayer to Hexagonal (II) transition (Figure 2B).

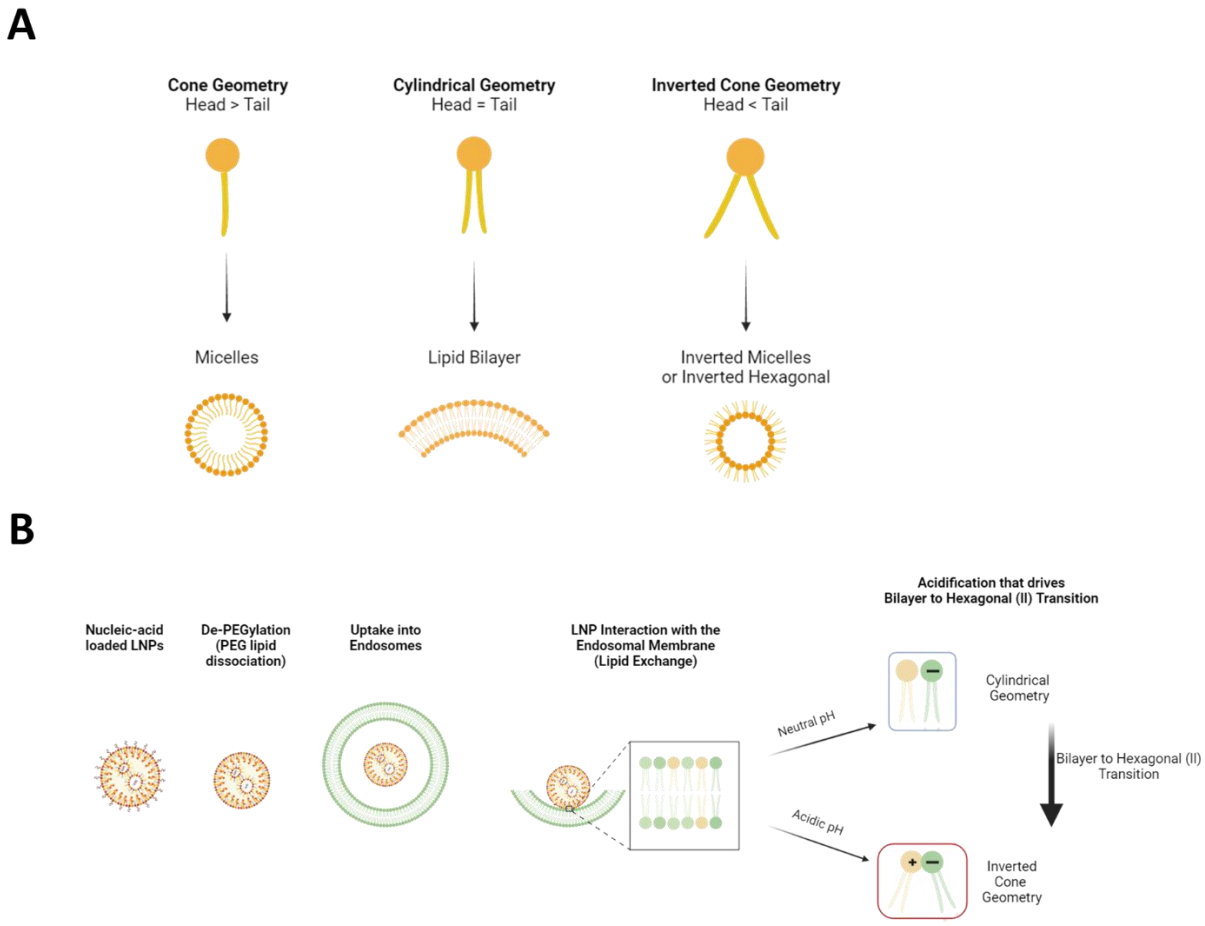

Figure 2: *Lipid Polymorphism and Endosomal Escape. (A) Schematic of how the geometry of the lipid tail and head influence the assembly structure of the lipids. (B) Schematic of LNPs interaction with the endosomal membrane and how acidification drives the bilayer to hexagonal transition to achieve endosomal escape. Created with BioRender.com.*

On the other hand, earlier studies attributed the endosomal escape to the Proton Sponge Effect, which depends on the presence of weakly basic tertiary amines which when ionized, they increase the endosomal membrane potential resulting in higher chloride diffusion that raises the osmotic pressure and destroys the endosomal membrane [26,27].

Adopting one of these hypotheses can influence the optimization steps in the study. Explaining endosomal escape through lipid polymorphism influenced subsequent studies to manipulate the transition temperatures by changing the tail branching and length [21,28,29]. Increasing the branching or

decreasing length reduces the London Dispersion force between the hydrophobic tails and lowers the phase transition temperature (T_m) and the bilayer-to-H(II) transition temperature (TBH). While explaining endosomal escape through the concept of ions sponge have influenced some studies to increase the number of tertiary amine groups in the ionizable lipid structure [30,31].

In addition to the ionizable lipids, PEGylated lipids are required to prevent the aggregation of LNPs as they form a hydrophilic steric sheath around LNPs [32]. PEGylated lipids are amphiphiles consisting of a lipid conjugated to a polyethylene glycol (PEG) moiety. They therefore tend to accumulate at the interface between LNPs and the external aqueous phase [33]. PEGylated lipids diminish the interaction of LNPs with each other, thus reducing LNPs aggregation and enhancing their colloidal stability. They also decrease the opsonization process and reduce LNPs interaction with the immune cells [34]. The properties of the PEGylated lipids are also governed by the lipid head group charge and the tail length and unsaturation. Zhu et al have showed how the tail unsaturation leads to significant differences in PEG-lipid dissociation rate and in vitro uptake of the NPs [35]. They found that DSPE-PEG, which has a saturated tail, has a dissociation half-life of 24.7 hours. While the DOPE-PEG has a dissociation half-life of 2.1 hours, due to the tail unsaturation.

Beside ionizable and PEGylated lipids, other structural helper lipids are incorporated in the LNPs to efficiently deliver nucleic acids. DSPC and cholesterol were found to promote the stability of nucleic-acid complexes with ionizable lipids in neutral physiological pH enabling high encapsulation efficiency [36]. Besides, helper lipids and cholesterol have been shown to affect the LNPs biodistribution. Zhang et al have found that changing the helper lipid affect the apolipoprotein E (ApoE) adsorption on LNPs that drives their hepatic delivery. Therefore, when they replaced DOPE with DSPC, the ApoE adsorption decreased leading to higher delivery to the spleen [37]. Besides, Hatit et al have shown that the stereochemistry of hydroxycholesterols plays a role in the LNPs interaction with the phagocytic pathways. Therefore, testing LNPs with different hydroxycholesterol's stereochemistry led to a big difference in mRNA delivery potency [38].

Permanently charged lipids are a fifth lipid type that were recently being adopted in the composition of different LNPs. Dilliard et al showed that the charged lipids change the pKa of the LNPs, which leads to different protein adsorption and drive LNPs delivery to extrahepatic targets [39]. Specifically, they showed that the incorporation of 50% DOTAP of the total lipid composition of LNPs resulted in preferential lung accumulation in comparison to a hepatic accumulation of control LNPs with 0% DOTAP. While the inclusion of the anionic lipid (1,2-dioleoyl-sn-glycero-3-phosphate, 18PA) with a percentage of 30% of the total lipid led to exclusive transfection at the spleen [40]. Therefore, they called their approach selective organ targeting (SORT) LNPs. By applying SORT technology, we aim at studying the effect on LNPs interaction with the placenta and maximize the nucleic acid transfection to fetal cells compared to maternal cells.

Although the Onpattro formulation was optimized for hepatic delivery, follow-up studies showed that manipulations in the helper lipids or charged lipid types or percentages have led to preferential transfection in the spleen, pancreas, or lung [37,41,42]. Despite numerous efforts, achieving efficient non-liver targeting using LNPs following intramuscular or intravenous injection is still challenging. There have been different strategies to drive non-liver targeting, which focused mainly on LNPs composition manipulations or antibody-conjugated LNPs, as recently summarized [43].

1.3 Microfluidic Synthesis of Lipid Nanoparticles

Historically, lipid-based nanoformulations have been routinely prepared by the thin-film hydration method or the ethanol injection method. These methods suffer many limitations; they involve many steps such as sonication, buffer exchange, extrusion or filtration. First, some of these steps should be done at the scale of milliliters at least, which makes it not economical at the development stage where you optimize different formulation compositions [44]. Also, some of these formulation development steps are not easily scalable, so making it harder to manufacture it on a large scale after the optimization [45].

Microfluidics enables the manipulation of fluids at the microscale; this allows controlled mixing of minute amounts of liquids, which gives control over the self-assembly process. This translates to a precise control over the size and size distribution (polydispersity index) of NPs. There are many parameters that affect the process; the design of the microfluidic device, the flow rates, and the concentration and composition of the lipids [45]. Chip design plays a great role on the speed of nanoparticles formation, hence, affecting the size and size distribution. There are different designs; some of them are commonly used such as hydrodynamic focusing and chaotic micromixer [46], and other designs such as T-shaped mixer, Bi-furcating mixer, and Baffler mixer [47].

In the microfluidic device, there's a control on two flow rates, the aqueous phase flow rate which usually contain the nucleic acid and the ethanol (organic) flow rate which contains the lipid. The summation of these two flow rates is called the total flow rate (TFR), and the ratio between them is called the flow rate ratio (FRR). The self-assembly of LNPs is affected by the growth time which is affected by the TFR and FRR. The self-assembly of LNPs is also dependent on the nucleation time; the nucleation time is dependent on the concentration of the lipids [48].

Synthesis of lipid nanoparticles by microfluidics poses many advantages over traditional methods. First, Scalability, the process is easily scalable by running multiple channels in parallel [49]. Second, reproducibility, having precise control over the self-assembly process minimize batch-to-batch variations [50], which is essential for regulatory bodies' approvals. Another advantage of this controlled mixing is giving monodisperse nanoparticles [51], this could reduce the number of steps required for the manufacture of NPs with homogenous properties. Due to the ease of automation and the minute amounts of reagents needed, the microfluidic technique is suitable for high-throughput systems, where the tools of robotics and machine learning are utilized to synthesize and characterize many formulations. This makes the process of formulation development highly automated, making it more economically viable and less prone to human errors [52]. Another merit that makes the technique economical is the high encapsulation efficiency [53], which saves a significant amount of the loaded cargo, that could be expensive like nucleic acids.

1.4 Bioengineered Model for In vitro Evaluation: Organ-on-a-chip Models [54]

Microfluidics is a discipline of science that deals with flow and manipulation of small volumes of fluid down to picolitres or lower constrained in dimensions <1000 μm [55]. When the dimensions in a fluidic system are downsized to the microscale, many of the impacts or phenomena that are observed on the macroscale are no longer valid. For example, gravitational forces become negligible in microscale and the surface tension dominates the gravity [56]. Fluid flow in microfluidic channels therefore behaves differently in which viscous force (the force due to the friction between fluid layers)

over inertial force (the resistance to change the motion state; speed, direction) and a fully laminar flow prevails [57,58]. These characteristics of the microfluidic devices allow the recapitulation of the different micro-cellular systems in the human body [59]. Microfluidics offers many advantages including economic use of samples and reagents due to the small volumes of liquids involved, the ability to conduct experiments under a highly replicable conditions, the precise control over the flow, high surface-to-volume ratio that allows a fast and cost-effective heat and mass transfer, the high spatio-temporal resolution and high control of variables in the microenvironment such as concentration gradients of nutrients and chemicals, and the ability to integrate different feedback control elements (like sensors and cameras) [59,60].

Microfluidic technology offers a powerful and advanced method to grow cells under dynamic flow of fluids, e.g., blood flow, simulating the in vivo environment [61]. The flowing fluid exerts a tangential force, termed shear stress, on the cell surface impacting the cell phenotype and the cell-nanoparticle interactions, e.g., cell uptake of nanoparticles and cell viability following exposure to nanoparticles [62-66].

Advances in the development of cellular co-culture models, microengineering techniques, 3D bioprinting, and microfluidics have enabled the emergence of the organ-on-a-chip (OOC) technology. The OOC concept is based on loading a microfluidic chip with cell architecture to simulate specific organ or tissue microstructure. These devices can be fully tuned so that a variety of cells, matrices and other components can be included to better represent the complex physiology, structural organization, as well as the physical and biochemical environment of the organ. Further, the dynamic flow of fluids through these chips simulates the dynamic physiological environment e.g., blood flow, in which the flowing fluid exerts a tangential force, termed shear stress, on the cell surface modulating the cell phenotype and the different cell responses and functions [61]. The microfluidic OOC devices allow the communication between different cells, tissues, and biochemical environments through microchannels or porous membranes. Therefore, the design of the microfluidic devices plays a central role in the performance of the models [67].

1.5 Bioengineered Models of the Placental Barrier

Human placenta is a highly organized organ with a myriad of functions such as exchange of fluids, nutrients, oxygen, removal of waste products, and control of substances reaching the fetus [68]. Human placenta is disc-shaped, and it is formed from maternal placenta (known as decidua) and fetal placenta, of which the outermost layer is the chorion. The chorion, where substrate exchange occurs, consists of trophoblast cells (cytotrophoblasts and the syncytiotrophoblasts) and fetal mesodermal cells. Further, the structure and thickness of the placental barrier varies along pregnancy [69].

Substrate transfer across the placenta occurs by mechanisms such as passive diffusion, facilitated diffusion, active transport, and pinocytosis [70]. IgG antibodies can pass through the placenta through receptor-mediated endocytosis. Specifically, IgG antibodies pass from the mother to the fetus in utero through binding to the Fc neonatal receptors (FcRn) which are expressed on the maternal side of the placenta [71]. Therefore, FcRn receptors are considered attractive targets to mediate transplacental delivery of nanoparticles; IgG conjugated chitosan NPs showed higher placental transport compared to bare NPs [72].

Different models have been used to study the transport across the placental barrier. The models vary in complexity, physiological relevance, and reproducibility. They range from the in-vitro static and organ-on-a-chip models to the in-vivo and human placenta perfusion models. Each poses certain advantages and suffers some limitations [54,73]. Nanoparticle transport across the placental barrier has been assessed in static transwell models [72,74], organ-on-a-chip models [75], and human placenta perfusion models [76]. Most studies focused on polymeric nanoparticles from the perspective of toxicological studies. While no data has been reported yet evaluating the placental transfer of LNPs with their conventional four component composition up to the best of our knowledge. Understanding nanoparticles' interactions with the placental barrier is of utmost clinical significance. Outlining the parameters affecting the NPs' transport to fetal circulation is essential to designing safe therapeutics for pregnant women.

Rationale

Despite the rapid advancements in LNPs as a gene delivery vehicle, LNPs interactions with the placental barrier are underexamined. Optimizing LNPs transplacental transport is an essential step in developing fetal gene therapies. LNPs are composed of different lipid types that lead to diverse properties and biological behavior, so there is a need to examine how manipulations in the LNPs composition affect the placental transport. Besides, the placenta poses a dynamic barrier as its structure and properties vary across the different stages of pregnancy. Therefore, it’s essential to study LNPs transport at different placental models. So, placental barrier variations are considered when developing fetal gene therapies.

Studying the variations of LNPs composition and the placental model designs represent a multi-hierarchal problem that’s hard to interpret using traditional linear mode. So, there’s a need for advanced analysis methods such as machine learning to draw more holistic conclusions.

There has been progress in developing targeted LNPs that can achieve extrahepatic delivery in adults, but optimizing the LNPs composition for preferential transfection in fetal cells is still needed. Besides, there’s a need to study the effect of LNPs exposure on fetal organ development. It can ensure that targeted LNPs could be a safe vehicle for fetal gene therapies.

Hypotheses

We hypothesize that the composition of nucleic acid-loaded LNPs will induce nanoparticle transport across the placenta by changing the ionizable lipids, PEGylated lipids, or antibody orientation. Secondly, we hypothesize that changes in placental model design induce changes in LNPs transport. Besides, utilizing machine learning to analyze the LNP's placental transport can delineate the top factors affecting the transport and inform the formulation design. Furthermore, tuning the internal charge of the LNPs using permanently charged lipids or adjusting the lipids and nucleic acid ratios will direct the LNPs transfection into fetal lung cells. Finally, dynamic flow will induce cellular-level changes in the placenta and alter the nanoparticles interaction with the placental barrier.

Chapter 2: Optimizing Lipid Nanoparticles for Fetal Gene Delivery In Vitro, Ex Vivo, and Aided with Machine Learning

Amr Abostait[1,2], Mahmoud Abdelkarim[1,3], Zeqing Bao[4], Yuichiro Miyake[5,6], Wai Hei Tse[5], Caterina Di Ciano-Oliveira[1], Tina Buerki-Thurnherr[7], Christine Allen[4], Richard Keijzer[5], Hagar I. Labouta[1,2,3,4]

[1]Keenan Research Centre for Biomedical Science, Unity Health Toronto, Toronto M5B 1T8, Canada

[2]College of Pharmacy, University of Manitoba, Winnipeg R3E 0T5, Canada

[3]Biomedical Engineering, Faculty of Engineering, University of Toronto, Toronto M5S 3G9, Canada

[4]Leslie Dan Faculty of Pharmacy, University of Toronto, Toronto, ON M5S 3M2 Canada

[5]Department of Surgery, Division of Pediatric Surgery, Max Rady College of Medicine, Rady Faculty of Health Sciences, University of Manitoba and Children's Hospital Research Institute of Manitoba, Winnipeg, MB R3E 3P4, Canada

[6]Department of Pediatric General and Urogenital Surgery, Juntendo University School of Medicine, Tokyo, Japan, Address: 2-1-1 Hongo Bunkyo-ku, Tokyo 113-8421, Japan

[7]Laboratory for Particles-Biology Interactions, Swiss Federal Laboratories for Materials Science and Technology (Empa), St. Gallen, 9014 Switzerland

Contributions of Authors

A.A. performed most of the experiments (formulation development, characterization, and in vitro work). A.A. and Y.M. performed the ex-vivo experiments. A.A. and C.D. performed the imaging and image analysis. M.A. and Z.B. developed the machine learning models. A.A., H.L., M.A., Z.B. processed the experimental data and performed the analysis. A.A. wrote the first draft of the manuscript, with the help of M.A., Z.B. and H.L who also contributed to the design of Figures. A.A., H.L., M.A., Z.B. processed the experimental data, performed the analysis, drafted the manuscript and designed the figures. H.L., R.K., C.A., T.B. aided in interpreting the results and worked on the manuscript. H.L. led the project conception and design and funding acquisition and has supervised the work. R.K., C.A., W.T. were involved in planning and supervision of various parts of the project. All authors read and approved the manuscript.

1. Introduction

Congenital fetal anomalies occur during pregnancy and are characterized by abnormal fetal organ development, which can result in perinatal mortality or severe lifelong morbidity [1]. These anomalies complicate 3% to 6% of pregnancies and are one of the leading causes of infant mortality [77]. Congenital diseases exhibit phenotypic changes due to genetic mutations, chromosomal abnormalities, epigenetic changes, or environmental factors [2]. Many of these congenital diseases are attributed to genetic abnormalities that start at conception, and with advancements in prenatal diagnosis, early intervention to correct the course of the diseases during pregnancy could be possible [1,4,78].

Since many congenital diseases have been categorized as monogenic, early in-utero intervention by replacing or silencing the gene of interest could restore or improve normal fetal development [1,79]. For example, viral vectors have been adopted as a vehicle for gene therapies due to their targeting efficiency [9]. However, their development is often limited by challenges such as manufacturing difficulties, high cost [80], and particularly high immunogenicity risks which could be more severe during prenatal development [81]. In contrast, non-viral gene delivery systems based on polymer or lipid excipients are showing promise due to their low immunogenicity, ease of manufacturing, and reproducible physiochemical properties [82,83]. These advantages make non-viral gene delivery systems a potentially safer alternative vehicle for these fetal gene therapies.

Recent advancements in lipid excipients, particularly ionizable lipids, have established Lipid Nanoparticles (LNPs) as the safe and efficient vehicle for nucleic acid transfection. Compared to previous iterations of lipid-based formulations (e.g., liposomes), these LNPs have shown significant improvement in their efficiency in driving endosomal escape and higher encapsulation efficiency [84]. Endosomal escape is essential for cytosol delivery and protein translation or silencing. Ionizable lipids enable the endosomal escape of LNPs as they get positively charged at endosomal pH which drives the bilayer to hexagonal transition [25,85]. Patisiran, or Onpattro®, was approved in 2018 as the first FDA-approved LNPs formulation for nucleic acid delivery. The formulation included D-lin-MC3-DMA as the ionizable lipid, DSPC as the helper lipid, cholesterol, and DMG-PEG as the PEGylated lipid at molar percentages of 50, 10, 38.5, and 1.5, respectively [86,87]. Since then, different studies and drug development programs have proposed similar formulations or excipients for other targets.

To date there are no clinically approved nanoparticle formulations that can cross the placental barrier to achieve fetal targeting. Earlier, our team developed a novel fetal drug delivery approach by leveraging the natural transfer of passive immunity from the mother to the fetus through the FcRn receptors which transport immunoglobulin G (IgG). Similarly, IgG conjugated chitosan nanoparticles showed higher placental transport compared to bare nanoparticles [72].

Few other studies showed an impact of the physicochemical properties of nanoparticles, including size and surface chemistry, on their transport efficiency across the placenta [76,88]. Most of these studies focused on polymeric and inorganic nanoparticles from the perspective of toxicological studies. However, the limited data available are sometimes conflicting and may require further systematic studies for a more compressive validation. This is because many studies that focus on a single characteristic of nanoparticles may not provide accurate predictions for placental transport [76,89,90]. Therefore, studying multiple properties, such as material composition, surface charge and

modifications, and biological factors, could be more capable of modeling placental transport by establishing structure-activity relationships (SAR) [90]. To date, a systematic approach to investigate the transport of LNPs across the placenta is lacking.

In this work, we are adopting a multiparametric approach to develop the first predictive model on the transport of LNPs across the placenta. Given the complexity of the datasets when optimizing new formulations, linear (single cause–effect) models and other algebraic approaches will have difficulty discerning trends from the experimental dataset. On the other hand, machine learning (ML) as a data-driven approach has shown its effectiveness in tackling these challenges and demonstrates potential in the design of drug delivery systems [91,92]. Modeling the relationship between LNPs design parameters and their transplacental transport metrics is critical to inform the development of optimized LNPs for nucleic acid delivery to the fetus for management of congenital anomalies.

Aside from nanoparticle transport across the placenta, it is important to optimize the LNPs formulation to maximize nucleic acid transfection in fetal cells in order to increase the efficacy of the congenital therapy. The impact of LNPs exposure on fetal development should also be assessed. While the cargo delivered, such as siRNA or mRNA, could restore normal development and prevent permanent damage, the delivery vehicle itself could pose toxicity issues on fetal development [93]. To this end, we present here a workflow based on in vitro and ex vivo experiments for initial screening of LNPs formulations for transplacental transport, viability and transfection efficiency using model placental trophoblast and fetal lung cells. Understanding all these parameters is the first step to designing safe and effective congenital therapies during pregnancy.

2. Methods:

2.1 Materials

All the lipids were purchased from Avanti Polar, except D-lin MC3 DMA was purchased from MedChemExpress; all the lipids full name are included in Appendix 1. The transwell inserts with pore size 5 um were purchased from MilliporeSigma Canada (cat: CLS3421-48EA). All the centrifugal filters were purchased from Fisher Scientific (cat: UFC801024, UFC803024, 14558473). Alex Flour 488 (AF488)-siRNA was purchased from Qiagen (cat: 1027292). FITC-labeled human IgG (cat: F9636), FITC-dextran (cat: FD10S), and TNS reagent (cat: T9792) were purchased from MilliporeSigma Canada. Active Capase-3 antibody (cat: AF835) and iFlour 647-WGA (cat: 25559) were purchased from Cedarlane Labs. Primary rabbit ZO-1 antibody (cat: 40-2300) and goat anti rabbit-AF647 (cat: A-21245) were purchased from Invitrogen. Primary rabbit fcRn antibody (cat: ab193148) was purchased from Abcam. Human placental BeWo b30 cells were provided by Dr. Tina Buerki-Thurnherr (EMPA, Switzerland). Human Umbilical Vein Endothelial Cells (HUVEC) was purchased from Lonza (cat: C2519A). Human fetal lung fibroblast (WI-38) was purchased from ATCC. ViaLight Plus Cell Proliferation and Cytotoxicity BioAssay Kit was purchased from Lonza (cat: LT07-221).

2.2 Lipid Nanoparticles Synthesis

Lipid nanoparticles were formed by hydrodynamic focusing using the 5-inlet microfluidic chip from Dolomite Microfluidics (Norwell, USA). Mixtures of different ionizable lipids, helper lipids, cholesterol, PEGylated lipids were mixed at different molar percentages, as outlined in Table S2. A Rhodamine-B labeled lipid was added to the lipid mixture at a 0.5 molar percentage to prepare fluorescent LNPs for tracking using fluorescence measurements and imaging. The final lipid mixture

was solubilized in ethanol at a concentration of 2 mg/ml. Using two programmable syringe pumps, the lipid was injected into the middle channel at a flow rate of 15 µl/min while MES buffer, pH6, 0.1 M, was injected into the side channels at 75 µl/min, achieving a flow rate ratio of 5:1. Following the formation of LNPs, they were centrifuged three times at 2500 g for 12 minutes at 4 °C using Amicron centrifugal filters (10,000 Dalton) to remove ethanol. In each centrifugation round, the LNPs was redispersed in a 3 ml of 10 mM PBS, pH 7.4.

To prepare siRNA-loaded LNPs to measure transfection efficiency, AF-488 labeled siRNA was introduced in the aqueous phase (10 mM citrate buffer at pH of 4). The concentration was adjusted to achieve a lipid: siRNA weight ratio of 40:1, 20:1, or 10:1; most formulations have a ratio of 40:1 unless otherwise stated. Rhodamine-B lipid was not used for labelling siRNA-loaded LNPs. For centrifugation of siRNA-loaded LNPs, 30,000 Dalton filters were used at 1358 g for 10 minutes at 4 °C , and 3 ml of RNAse-free PBS was added in each centrifugation round. The supernatant was analyzed for fluorescence of unencapsulated siRNA to indirectly determine the encapsulation efficiency.

We used EDC/NHS conjugation reaction to prepare IgG-coated LNPs, in which 3 ml of MES buffer, pH 6, 100 mM was added in each centrifugation round.

2.3 IgG Surface Conjugation

LNPs were conjugated with FITC-labelled IgG (labelled by the manufacturer) to use FITC fluorescence as a surrogate for IgG density following LNPs conjugation using a plate reader. IgG antibodies are supplied with 15 mM sodium azide for preservation, but this concentration can interfere with conjugation reactions. Therefore, prior to the conjugation reactions, IgG was filtered using 10,000 Dalton centrifugation filters at 1559 g for 10 minutes and were redispersed in 2 ml sterile PBS.

Different functionalized DSPE-PEG lipids were included in the different formulations at 0.5 molar % to achieve IgG conjugation at different orientations. Each functional group requires different reactions for IgG surface conjugation, as detailed below.

For LNPs prepared using DSPE-PEG-COOH, LNPs dispersed in 0.1 M MES buffer (pH=6) were reacted with EDC and sulfo-NHS at a (DSPE-PEG-COOH: EDC: sulfo-NHS) molar ratio of 1:10: 25 for 2 hours at room temperature with gentle shaking. Surface activated LNPs were centrifuged using 10,000 Dalton filters to remove the excess EDC and sulfo-NHS and replace the MES buffer with PBS buffer. Within a few minutes, IgG was added to the activated LNPs. The formulation was gently shaken for 1 hour at room temperature, then shaken overnight at 4 °C.

For LNPs prepared using DSPE-PEG-NH2, we first reacted 40 µg of FITC-IgG dispersed in MES buffer with 16 µg of EDC and 24 µg of sulfo-NHS for 30 minutes at room temperature followed by centrifugation using 10,000 Dalton filters to remove excess EDC/NHS. Activated IgG was redispersed in PBS and mixed with LNPs while shaking for one hour at room temperature, then overnight at 4 °C .

For LNPs prepared using DSPE-PEG-Maleimide, we first reacted 40 µg of FITC-IgG with 0.55 µg of Traut's reagent in 2.5 mM EDTA solution for one hour at room temperature to convert the primary amine groups in the IgG to thiol groups. The antibody was filtered using 10,000 Dalton filters to remove excess Traut's reagent. Finally, LNPs containing the maleimide groups were added to the treated IgG while shaking for 1 hour at 4 °C to form thiol-maleimide bonds.

To remove unbound FITC-IgG following any of these reactions, the LNPs formulations were centrifuged using 300,000 Dalton filters at 110 g for 10 minutes for four times and LNPs were dispersed in sterile PBS. The supernatant was collected in each step to measure the concentration of unbound IgG and indirectly calculate the IgG conjugation efficiency.

2.4 Lipid Nanoparticles Physicochemical Characterization:

We measured the size, size polydispersity index (PDI), and zeta potential of all prepared LNPs formulations using a Zetasizer Ultra (Malvern Polyanalytical), which depends on dynamic light scattering. For measurement, the LNPs samples were diluted in buffer (0.2 um filtered) to a concentration of 0.05 mg/ml; the buffer the LNPs were dispersed in can be found in Appendix 2.

The number concentration of LNPs, number of particles per ml, was determined using ZetaView Nanoparticle Tracking Analysis (NTA, Particle Metrix GmbH, Germany). The measurement parameters were optimized to achieve the optimal mean intensity and number of particles per field of view. The pre-acquisition parameters were set as follows: Sensitivity = 70, Shutter = 100, frame rate = 30, and Resolution: Medium. The post-acquisition parameters were as follows: Minimum Brightness = 25, Min Area = 5, Max Area = 1000, and trace length = 15.

2.5 Apparent pKa Measurement of Lipid Nanoparticles:

The TNS binding assay was used to determine the apparent pKa of LNPs. Buffer salts with different pKa were mixed as follows: 10 mM sodium acetate, 10 mM MES, 10 mM HEPES, and 130 mM sodium chloride. The pH was adjusted with hydrochloric acid or sodium hydroxide to achieve a pH range of 2.5 to 12, with an increment of 0.5. In each well of a black 96-well plate, a 100 µl buffer solution with different pH value was mixed with 3 µl of TNS reagent (0.1 mg/ml in water) and 5 µl of LNPs (0.5 mg/ml). The plates were gently shaken for 10 minutes, and fluorescence was measured using a plate reader at excitation and emission wavelengths of 321 and 445 nm, respectively. GraphPad Prism was used to fit the fluorescence data to the sigmoidal best-fit function (using the four parameter logistic (4PL) regression model).

2.6 IgG Surface Density and Conjugation Efficiency:

Following FITC-IgG conjugation and centrifugation using 300,000 Dalton filters, the supernatant with the unbound FITC-IgG was collected and measured for fluorescence using a plate reader using excitation and emission wavelengths of 485 and 528 nm. The concentration of unbound IgG was calculated reference to a 10-point preconstructed calibration curve and the conjugated IgG concentration was calculated indirectly based on the difference from the total theoretical IgG concentration used in the conjugation reaction. From the conjugated concentration, the mass of IgG and the number of IgG in the sample was calculated, and relying on the NTA results, the number of antibodies per LNP (Equation 1) and the distance between antibodies on the LNP surface (Equation 2) were calculated.

$$Number\ of\ antibodies\ per\ LNP = \frac{(number\ of\ conjugated\ Antibodies)}{number\ of\ LNPs\ in\ the\ sample} \quad eq: 1$$

$$Approximate\ distance\ between\ antibodies\ (nm)\ = \pi \times \sqrt{\left(\frac{(LNP\ Diameter \times 10^{-9})^2}{n\ of\ Antibodies\ per\ LNP}\right)} \times 10^9 \quad eq: 2$$

2.7 In Vitro Cell Culture Models:

Each of human placental BeWo b30 trophoblast cells, Human Umbilical Vein Endothelial Cells (HUVEC) and human fetal lung fibroblast (WI-38) were cultured at a humidified atmosphere with 5% CO_2 at 37 °C . Different culture media were used for the different cells. Ham's F12 K Nutrient Mixture, Kaighn's Mod supplemented with L-Glutamine, 10 % FBS and 1 % Penicillin-Streptomycin was used to culture BeWo cells. HUVEC cells were cultured using EBM™-2 Basal Medium supplemented with EGM™-2 SingleQuots™ Supplements (ATCC). WI-38 lung fibroblasts cells were cultured in EMEM supplemented with L-Glutamine and 10 % FBS. Near confluency, cells were sub-cultured using 0.5% trypsin–EDTA. For this work, we used passages 28-43, 5-9 and 19-22 for BeWo, HUVEC and WI-38, respectively. For transport experiments, cells were cultured on transwell membranes in 24-well plates as summarized in Figure 4. First, membranes were treated with fibronectin for 2 hours to promote the adherence of HUVEC cells on the bottom side (in EBM-2 media) and then BeWo cells were cultured on the side facing the apical compartment (in F12K media). The seeding density and time were optimized to ensure both cells were forming a monolayer without overgrowth. The exposure time of forskolin was optimized to achieve syncytialization, as shown in Appendix 1.

For the combined transport and transfection experiment (Figure 12), lung fibroblasts were additionally seeded on the bottom of the basolateral compartment (in EMEM media) at a seeding density of 30,000 cells per well before seeding the BeWo cells.

2.8 Cell Viability Study:

Cells were seeded in 96 well plates at a density of 10,000 cells per well for 24 hours before exposure to different concentrations of LNPs for another 24 hours. As a negative control (NC, 100% viability), some wells were treated with media only (no LNPs) for 24 hours. Positive controls (PC, 0% cell viability) were exposed to triton X-100 for 10 min. We conducted Calcein and Vialight assays, to measure cell viability under different conditions. Also, we conducted MTT assay (refer to Appendix 1). For all of these assays percentage cell viability was calculated according to Equation 3.

$$Viability\ \% = \frac{Signal\boldsymbol{experimental} - Signal_{PC}}{(Signal_{NC} - Signal_{PC})} \qquad eq: 3$$

2.8.1 Calcein assay:

Following 24 hour cell exposure to LNPs, cells were washed with 1x DPBS, then incubated with 100 µl of 1 uM Calcein in DSPS Solution for 30 minutes at 37 Celsius and 5% CO2. Then, the fluorescence was recorded using a plate reader with the green filter (ex485, em528).

2.8.2 ViaLight assay:

After 24 hours of exposure to LNPs, cells were treated with a 50 µl cell lysis reagent for 10 minutes at room temperature. A volume of 100 µl of the supernatant was then incubated with a 100 µl ATP monitoring reagent per well in black, clear bottom 96 well plate for 2 minutes in the dark before bioluminescence measurement using a plate reader.

2.9 Lipid Nanoparticle Transport Assays

Prior to transport studies, barrier formation of the different placental models was checked quantitatively using a fluorescence transport assay using 10 kDa FITC-labeled dextran; 100 µl of 42 µg/ml was added to the apical compartment. At different time intervals, 25 µl samples were withdrawn from the basolateral compartment at three time points, diluted suitably with fresh media and assayed using plate reader (excitation and emission wavelengths of 485 and 528 nm). Samples withdrawn were immediately replaced with an equal volume of fresh medium, which was accounted for in the transport percentage calculations. FITC-labelled dextran concentration reference to a 10-point preconstructed calibration curve.

LNPs transport experiments were conducted following the same seeding protocols and using freshly prepared LNPs within 24 – 48 hours of synthesis. A total volume of 100 µl dispersion of rhodamine-labelled LNPs in culture media was added to the apical compartment, representing the maternal side of the placenta. At different time intervals up to 24 hours, 25 µl samples were withdrawn from the basolateral compartment (600 µl total), representing the transported LNPs to the fetal compartment. Samples withdrawn were immediately replaced with an equal volume of fresh medium. Withdrawn samples were diluted suitably, and analyzed for fluorescence in black 96 well plates at excitation and emission wavelengths of 560 nm and 600 nm, respectively, and the mass of transported LNPs was determined according to an 8-point standard curve generated for each formulation. Percentage transport was calculated by dividing the fetal side concentration by the equilibrium concentration. The equilibrium concentration was determined by dividing the total mass added to the maternal side by the total volume (the sum of the maternal side volume, 100 µl, and the fetal side volume, 600 µl).

2.10 Transport Kinetics Models:

2.10.1 Data Acquisition and Processing:

Transport data for various LNPs were collated. This dataset included time-course concentration data which was subsequently utilized to analyze nanoparticle transport across cellular barriers. The data normalization was performed relative to the final equilibrium concentration (C_∞), providing a standard framework for comparison across different nanoparticle formulations.

2.10.2 Kinetic Model Implementation:

A Logistic Growth Model was employed to characterize the transport of LNPs. The logistic growth model is used to describe saturation dynamics typical in biological transport processes, which are crucial for effective nanoparticle permeation through biological barriers, such as the placenta in this work. The logistic model is defined according to Equation 4.

$$C_t = \frac{C_\infty}{1+e^{-k(t-t_o)}} \qquad \textit{eq: 4}$$

Where, C_t is the concentration of nanoparticles at time t, C_∞ is the final equilibrium concentration, and k is the rate constant. Here, t_o represents the inflection point where the growth rate is maximal, effectively indicating the half-maximal concentration time.

2.10.3 Parameter Estimation and Model Fitting:

Custom Python scripts were developed to fit the model to the normalized concentration data. The scripts utilized non-linear curve fitting techniques with multiple initial guesses to ensure robust model fitting. Key parameters such as the rate constant (k), half-time ($t_{1/2}$), and the inflection point (t_o) were extracted from the fits.

2.10.4 Apparent Permeability Calculation:
Apparent permeability (p_{app}) was calculated to assess the efficiency of LNPs transport across the placental barrier. The formula used was:

$$P_{app} = \frac{dQ}{dt}\frac{1}{A\,C_o} \qquad eq: 5$$

Where $\frac{dQ}{dt}$ is s the rate of mass transport, A is the effective surface area of the membrane, and C_0 is the initial concentration in the donor compartment. papp is critical for understanding the transport characteristics of nanoparticles, including their interaction with the barrier and transport kinetics.

2.10.5 Statistical Analysis and Visualization:
Statistical measures such as root mean square error (RMSE) and the coefficient of determination (R^2) were computed to validate the fit quality of the models.

2.11 - Machine Learning Modelling of Transport Percentage and Transport Kinetics:
2.11.1 Dataset Correlation Analysis
The pairwise correlation between all the descriptors (input features and the target) was analyzed. Specifically, the Pearson correlation coefficient was computed using pandas.DataFrame.corr. The results were visualized using a heatmap, where red color indicates a positive correlation and blue indicates a negative correlation. The strength of the correlation (i.e., the absolute value of Pearson correlation coefficient values) was indicated by the intensity of the color, with darker colors representing stronger correlations.

2.11.2 ML Modeling
Prior to modeling, the input features in the dataset were standardized using sklearn.preprocessing.StandardScaler. ML models were then developed using the scaled dataset to predict the target variables (i.e., transport percentage, transport kinetics, permeability, or half-time). A panel of models, including extreme gradient boosting (XGB), decision tree (DT), random forest (RF), support vector regressor (SVR), light gradient boosting machine (LightGBM), and linear model with least absolute shrinkage and selection operator regularization (Lasso), were developed for comparison. These models were initialized with their default hyperparameters from sklearn, xgboost, and lightgbm libraries.

The models were trained and evaluated using a leave-one-out cross-validation method. The model performance was measured using four metrics to provide a comprehensive evaluation: mean absolute error (MAE), median absolute error (MedAE), root mean squared error (RMSE), and mean squared error (MSE). The model that performed the best across most of these metrics was identified as the best-performing model for further analysis.

2.11.3 Model Interpretation and validation

The best-performing model identified from the model evaluations was further analyzed to gain insights into the relationships between the features and the target. Specifically, the model was interpreted using Shapley Additive exPlanations (SHAP) analysis to rank the input features in terms of their importance to the prediction. The results were visualized using shap.summary_plot.

We then validated the ML model using external data not included in the training dataset. We relied on the top 5 features from SHAP analysis to design three new formulations that are expected to have low, moderate, and high transport across the placenta and then tested their transport at 24 hours.

2.12 Machine Learning Modeling of Lipid Nanoparticles Size and Zeta Potential:

First, the dataset correlation analysis was conducted using the same methodology in section 2.11.1.

2.12.1. Machine Learning Modeling:

To address the imbalance in the dataset, Random Over-Sampling was applied to ensure a more balanced distribution of feature values. This method involves duplicating instances from the minority class to increase their representation, thus augmenting the dataset and providing the model with more information on the minority class [94]. Following the over-sampling, the dataset was modelled using the same methodology in section 2.11.2.

2.12.2. Model Interpretation:

First, feature importances were calculated for the best-performing models to identify the lipid type or process parameters contributing the most in the output prediction. After identifying the top 10 features, SHAP was employed to understand the contribution of each input feature to the predictions.

2.13 Cell Association study:

We used immunostaining protocols for qualitatively investigating barrier function, confirming FcRn expression and for cell uptake of LNPs. Following the 24 hour transport study, cells were washed with 1x PBS, fixed in 4% paraformaldehyde and washed three times in sterile PBS, permeabilized using 0.1 % triton x-100 in PBS, and blocked using a mixture of 0.1% tween-20, 3% BSA, 3% serum, 0.75% glycine in PBS for 1 hour at room temperature. Cells were then incubated overnight at 4 °C with the primary antibody, either ZO-1 diluted 1 in 80 or FcRn diluted 1 in 100. After washing, cells were incubated with the secondary antibody, goat anti rabbit-AF647, diluted 1 in 400 for 40 minutes at room temperature. Finally, nuclei were DAPI stained and mounted with mounting media and covered with 1.5 mm coverslips and were imaged using a QUORUM SPINNING DISC Confocal system using a 63x Oil objective and an ORCA-Flash 4.0 V2 PLUS sCMOS camera. The imaging parameters are summarized in Appendix 1. We used Z-stacks to calculate the sum of pixels due to LNPs associated with the cells in all optical slices following normalization to remove background signal

2.14 Transfection Study:

Cells were cultured in black 96-well plates till 50-60% confluency before exposure to LNPs encapsulating 1 picomole or 4 picomole of siRNA, to make a final concentration of 10 nM or 40 nM, respectively. For positive control (PC), cells were exposed to siRNA -Lipofectamine complexes prepared from 0.3 µl lipofectamine and 1 or 4 pmol of siRNA. Cells incubated with media only were used as a negative control (NC). After 24 hours of incubation, cells were washed with sterile 1x PBS to remove any unbound LNPs or siRNA, fixed in 4% PFA (methanol free) for 15 minutes, then washed with sterile 1xPBS 3 times. We used Alexa Fluor 647-labelled wheat germ agglutinin (WGA-647) for cell membrane staining. The staining protocol varied for the different cell lines. BeWo cells were incubated with 10 µg/ml WGA-647 in HBSS buffer for 10 minutes, then the nuclei were stained with

Hoechst (2 ug/ml in PBS) for 10 minutes. For lung fibroblasts, a solution of 5 µg/ml WGA-647 was incubated with the cells for 10 minutes followed by Hoechst at 2 µg/ml for 10 minutes.

Cell Discoverer machine was used for the transfection experiments as it enables automated high throughput imaging, which enabled the screening of multiple formulations. The imaging parameters are summarized in Appendix 1. Transfection was calculated based on the mean intensity values from the image analysis. Transfection was presented as a percentage relative to lipofectamine (PC) according to Equation 6.

$$Transfection\ \% = \frac{(MI_{exp} - MI_{NC})}{(MI_{PC} - MI_{NC})} \qquad eq: 6$$

2.15 Ex-vivo Experiments:

2.15.1 Rat Fetal Lung Explant Model:

We followed a protocol established by our team to harvest the rat embryos on day 18 of pregnancy and dissected fetal lungs [95] . Guided by a surgical microscope, a volume of 10 µl of LNPs formulations was injected into the lung via the trachea using a special microinjection needle described here [96]. Control lungs were injected with 10 µl of PBS each. The trachea was then tied off with a polypropylene surgical suture. The explants were placed on a 12-well plate with a membrane insert. The bottom of the insert was filled with DMEM/F12 media, containing: 8 mM L-glutamine, 100 mg/ mL primocin, 1.0% FBS. The plates containing explants were left in the incubator for 24 hours at 37 °C with 5% CO2. Then, lungs were formalin fixed for 24 hours at 4 °C. Subsequently, lungs were dehydrated in a methanol gradient, cleared in xylene, and embedded in paraffin.

2.15.2 Histological staining:

Hematoxylin and Eosin (H&E) staining was performed to study the lung air space. The lung tissue was sectioned using a rotary microtome (Leica, Germany) to produce sections with 5 µm thickness. To ensure reproducibility, an autostainer machine (Leica, Germany) was used to automate the staining process following a pre-set program: Oven 65 °C (10 min), Xylene (3 min,2 min, 2 min), 100 % Alcohol (1 min, 1 min), 95% Alcohol (1 min), H_2O wash (1.5 min), Haematoxylin (2.5 min), H_2O wash (1 min), DEFINE (acidic solution) (35 sec), H_2O wash (1 min), blue buffer (slightly basic solution) (45 sec), H_2O wash (1 min), 95% Alcohol (1 min), eosin (1 min), 100 % Alcohol (1 min, 1 min, 1 min), Xylene (2 min, 2 min). Finally, the slides were mounted and covered with 1.5 mm coverslips.

2.15.3 Immunostaining:

We used immunostaining and immunofluorescence imaging to study the effect of LNPs on lung cells proliferation and apoptosis. Lung sections (5µm) were deparaffinizated using the autostainer using the following program: Oven 65 °C (10 min), Xylene (3 min,2 min, 2 min), 100 % Alcohol (1 min, 1 min), 95% Alcohol (1 min), H_2O wash (1.5 min). Then the slides were immersed in an antigen retrieval buffer (10 mM sodium citrate, pH 6, with 0.05 % tween-20) and placed in a pressure cooker at 100 °C for 15 minutes. Following antigen retrieval, the slides were incubated with blocking buffer (PBS with 0.1 % tween-20, 2 % bovine serum albumin, 3 % FBS) for 3 hours at room temperature. Sudan black solution (0.1 % in 70% ethanol) was added for 30 minutes to reduce autofluorescence. Active Caspase-3 and ki-67 were used as the primary antibodies for Apoptosis and proliferation, respectively. The primary antibody diluted in blocking buffer (diluted 1 in 200) was added to sections

and incubated overnight at 4 °C followed by washing 3 times with PBST (PBS with 0.1 % tween-20). Treated lung sections were exposed to the secondary antibody, goat anti rabbit-AF647 or donkey anti mouse-AF647 (diluted 1 in 200), for 3 hours at room temperature followed by washing 3 times with PBST. The nuclei were stained with DAPI (1 in 1000) for 3 minutes. After washing with PBST, PBS, and double distilled water, the sections were left to dry and were covered with flourmount G and 1.5 coverslips (0.17 mm). The Axioscan slide scanner (ZEISS, Germany) was used to enable high throughput imaging of the lung tissue sections as it enables imaging of the whole section ensuring accurate analysis of the protein expression. The imaging parameters are summarized in Appendix 1.

2.15.4 Image Analysis

Image analysis of the tissue sections was conducted using HALO software (Indica Labs, USA). To measure the airspace of the lung in the H&E-stained sections, we used the tissue classifier function that relies on Random Forest algorithms. We first annotated the total area to be analyzed and then calculated the percentage area of air space by dividing the air space area by the total analyzed area. For immunofluorescence staining experiments, we used two methods for image analysis which are positive pixel counting and the nuclear segmentation method. The region of interest in all analyses was DAPI positive (DAPI+) areas. First, a threshold intensity was determined based on negative control sections, which are treated with secondary antibody only, but were not exposed to the primary antibody. The pixels exceeding the threshold intensity were designated antibody positive (Antibody+). In the nuclear segmentation method, we counted the apoptotic or proliferating DAPI-stained cells that are exceeding the threshold intensity for the antibody. Finally, percentage pixels and cells were calculated using Equations 7 and 8, respectively.

$$Percentage\ of\ apoptotic/proliferative\ pixels = \frac{no\ of\ Colocalized\ pixels\ (Antibody+\ \&\ DAPI+)}{no\ of\ DAPI+\ pixels}\ \%$$

eq: 7

$$Percentage\ of\ apoptotic/proliferative\ cells = \frac{no\ of\ Apoptotic\ or\ proliferative\ cells\ (Antibody+\ \&\ \ DAPI+)}{Total\ number\ of\ cells\ (DAPI+)}\ \%$$

eq: 8

2.16 Statistical Analysis

Statistical analysis was conducted using GraphPad Prism version 8.0.1 and IBM SPSS software. To compare two groups, the unpaired t-test was used for groups with equal sizes. We used the unpaired t-test with Welch's correction to compare groups that were not equal in size. For multiple groups comparison, one-way ANOVA or two-way ANOVA was conducted. First, normality checks and Levene's test were carried out to ensure the assumption of normality was met. If a significant p value ($p<0.05$) was found, the test was followed by post hoc Tukey's test. Significance levels were noted in the figures as follows: * for ($p<0.05$); ** for ($p<0.01$); *** for ($p<.001$).

3. Results and Discussions

3.1 Lipid nanoparticle synthesis using microfluidics

To gain a comprehensive understanding of the interactions of LNPs with the placental barrier, we used microfluidics to create a large library of LNPs (Figure 3A). This method allows for precise control over the mixing and formation of LNPs, which in turn determines the final size and PDI of the particles [17]. The 5-inlet chip was used for the LNPs formulation, as it enabled the formation of monodisperse LNPs (PDI < 0.25). Our library of LNPs was created by varying the type and percentage of ionizable lipids, non-functionalized PEGylated lipids, functionalized PEGylated lipids (carboxylic acid or amine terminated lipids), and permanently charged lipids (Figure 3B). The developed LNPs exhibited a broad range of zeta potentials and sizes. The zeta potential varied from -39 to +46 mv, with a median of -5. The particle sizes ranged from 68 nm to 252 nm, with a median of 112 nm (Figure 3C).

A

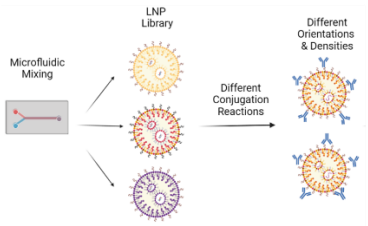

B

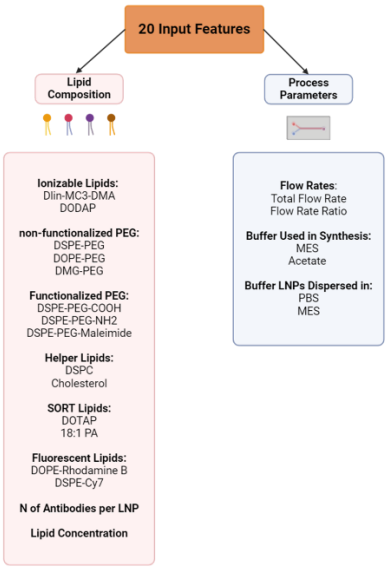

C

Physicochemical properties	Size (nm)	Zeta Potential (mV)
Minimum	68.3	-38.9
1st Quartile	92.5	-15.9
Median	111.8	-4.7
3rd Quartile	135.8	16
Maximum	251.7	46

D

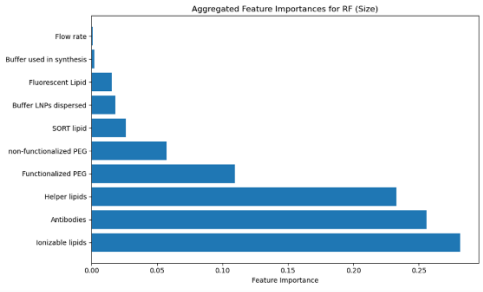

E

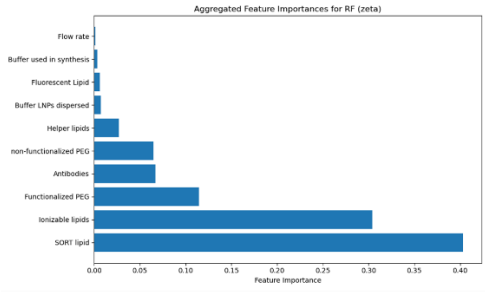

F

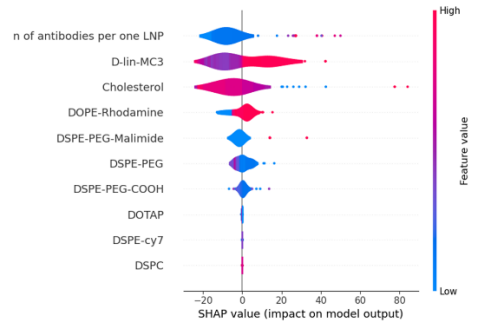

G

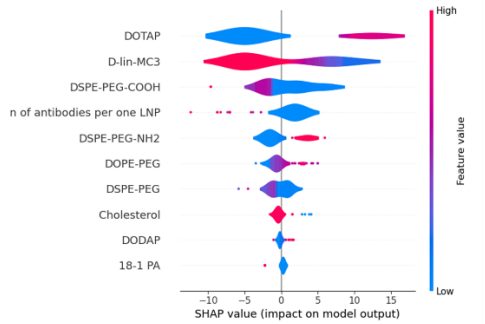

***Figure 3**: Synthesis and characterization of lipid nanoparticles (LNPs), and machine learning modelling for size and zeta potential. (A) A schematic of LNPs synthesis using microfluidic mixing followed by IgG surface conjugation; Created with BioRender.com. (B) Overview of the different variables/features used to develop the LNPs library, including lipid classes and process parameters; Created with BioRender.com. (C) Summary of the physicochemical properties of the LNPs library.*

The aggregated feature importance of each input (variable) including lipid classes and process parameters in predicting the (D) LNPs size and (E) zeta potential by Random Forest (RF) machine learning model. Shapley Additive explanations (SHAP) showing the top 10 input features predicting (F) the size and (G) the zeta potential of the LNPs.

Beside its ease of scalability, high reproducibility, and miniature scale, the microfluidic mixing process is easily programmable to achieve the high-throughput capabilities desirable in ML- driven studies [97]. The LNPs prepared using this microfluidic system were then characterized and complied into a dataset for ML model development, aiming to better understand how the composition and process parameters influence the particle size and zeta potential. The resulting best-performing models were interpreted in terms of feature importance for predicting LNPs size (Figure 3D) and zeta potential (Figure 3E). Ionizable lipids, the number of conjugated antibodies, and the helper lipids have the highest effect on the size which confirm previous reports [36,98]. Interestingly, fluid flow rates and the buffers employed had a minimal effect on the size and zeta potential. Collectively, our results show that lipid composition is the key determinant of the physicochemical properties of LNPs.

Among the different lipid types, permanently charged lipids (or SORT lipids) had the highest effect on zeta potential (Figure 3G). A previous mechanistic study attributed the targeting mechanism of SORT lipids to their influence on pKa [39]. However, our results show that SORT lipids are affecting zeta potential, which could be contributing to their different biodistribution. Functionalized PEGylated lipids, such as DSPE-PEG-COOH and DSPE-PEG-NH2, had the second highest effect on zeta potential, despite being used at a small molar percentage of 0.5%. Previous studies have used functionalized PEG to enable antibody or peptide conjugation to LNPs but did not take their effect on the physicochemical properties into consideration [99,100]. In contrast, our results point out their high impact on zeta potential, which warrants careful consideration in future formulation studies.

We used Shapley Additive Explanations (SHAP) to visualize the hierarchy of the significance of the different input feature values on the prediction of the output from the most important (at the top) to the least important (at the bottom) [101], as shown in Figures 3F and 3G . In these figures, the blue color represents low feature values, and the red color represents high feature values. In Figure 3F, where each lipid or feature was studied individually, a relatively high number of antibodies per LNP or high D-lin MC3 molar percentage contributes to a higher LNPs size. Conversely, high cholesterol molar percentages contributes to smaller size, as delineated in a previous study [36]. Additionally, Figure 3G shows how the lipid molar percentage influences the net zeta potential, with high molar percentages of the permanently cationic lipid DOTAP increasing zeta potential, and higher percentages of D-lin MC3 and DSPE-PEG-COOH decreasing it.

Collectively, the developed ML models for the size and zeta potential will benefit future formulations of LNPs by expediting their development stage to attain specific physicochemical parameters. For instance, increasing the ionizable lipid D-lin MC3 molar percentage or conjugating the LNPs with antibodies could increase the size of the LNPs and decrease their zeta potential.

3.2 Placental Model Development

To evaluate this library of LNPs (a total of 51 transport experiments with 44 formulations), we developed placental transwell models that are ideal for high throughput screening of formulations and are highly reproducible [73]. Aside from the various physicochemical parameters of the different

LNPs formulations, there are several variations in the placental barrier when choosing the number and types of cells included. We believe that these variations have partially contributed to the sometimes-conflicting results among the published data [102,103] . Some studies have used a model based on a monolayer of trophoblast cells to mimic the maternal side of the placenta [72,103,104], while others have additionally included endothelial cells as a surrogate of the fetal vessels [74,102,105]. Moreover, some have chemically induced trophoblast syncytialization, aka trophoblast cells fusion, using forskolin to form multinucleated syncytiotrophoblasts [105]. Therefore, we developed three different models to investigate the impact of endothelial cells and syncytialization on LNPs transport, as depicted in Figure 4.

A

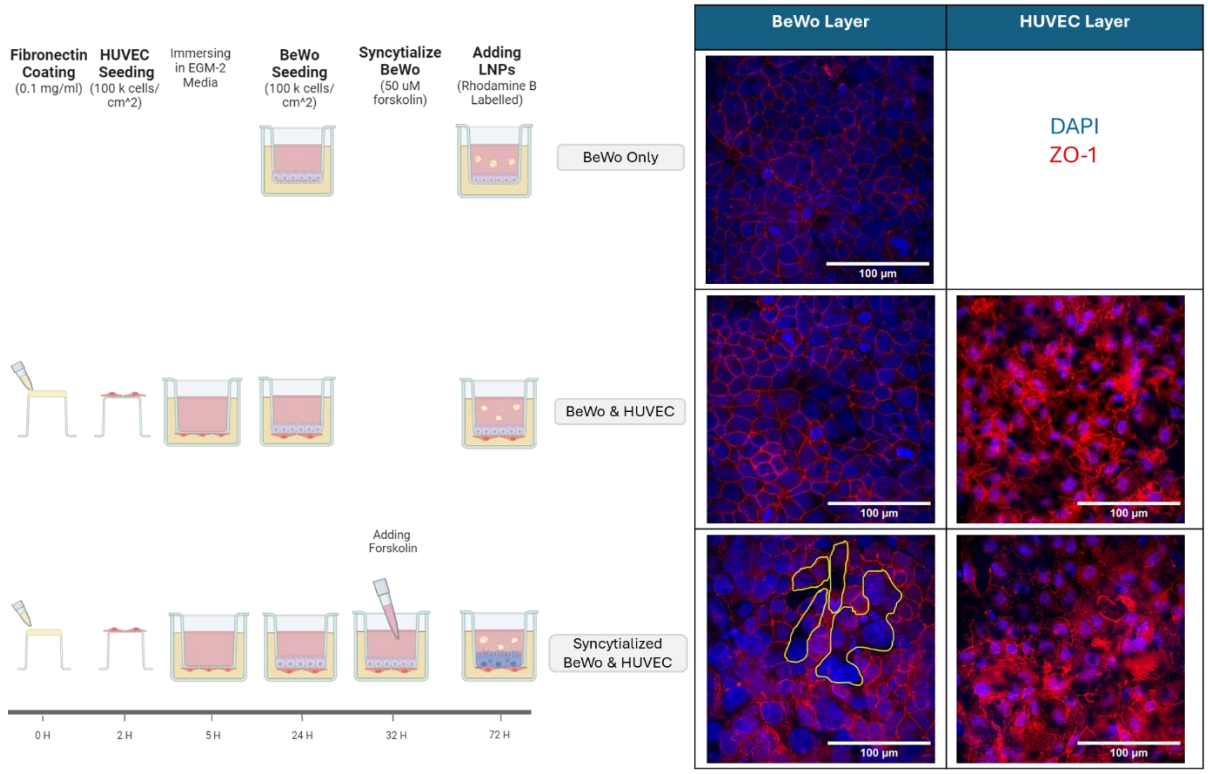
Fibronectin Coating (0.1 mg/ml)
HUVEC Seeding (100 k cells/ cm^2)
Immersing in EGM-2 Media
BeWo Seeding (100 k cells/ cm^2)
Syncytialize BeWo (50 uM forskolin)
Adding LNPs (Rhodamine B Labelled)
BeWo Only
BeWo & HUVEC
Adding Forskolin
Syncytialized BeWo & HUVEC
0 H
2 H
5 H
24 H
32 H
72 H
BeWo Layer
HUVEC Layer
DAPI
ZO-1
100 µm

B

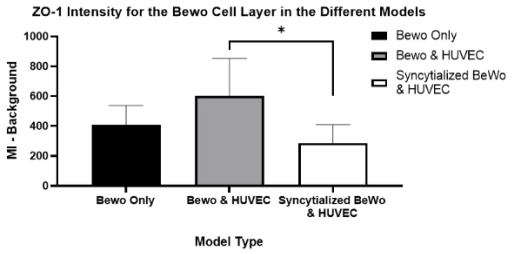
ZO-1 Intensity for the Bewo Cell Layer in the Different Models
MI - Background
1000
800
600
400
200
0
*
Bewo Only
Bewo & HUVEC
Syncytialized BeWo & HUVEC
Model Type

C

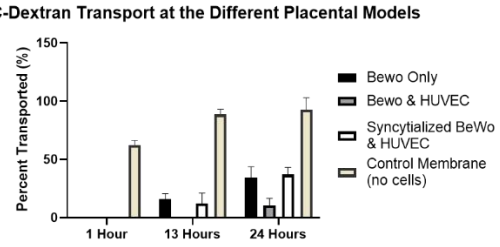
FITC-Dextran Transport at the Different Placental Models
Percent Transported (%)
150
100
50
0
1 Hour
13 Hours
24 Hours
Bewo Only
Bewo & HUVEC
Syncytialized BeWo & HUVEC
Control Membrane (no cells)

D

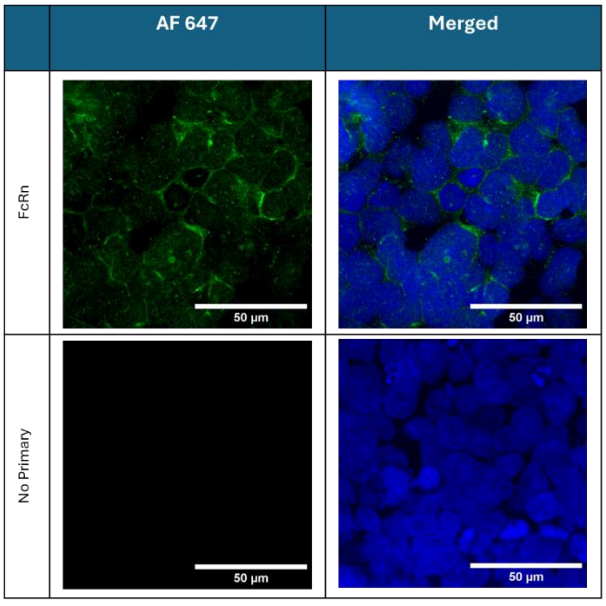
AF 647
Merged
FcRn
No Primary
50 µm

Figure 4: *Development of different placental models. (A) A schematic for cell seeding and other steps for the development of the different models; Created with BioRender.com. For each of these models, we characterized the barrier formation using ZO-1 tight junction staining, denoted in red and syncytialization in which the formation of multinucleated cells is annotated in yellow (B) Comparison of ZO-1 expression levels in the BeWo cells of the different models. (C) FITC-labelled dextran transport across the different placental models at different time intervals. (D) Staining of FcRn receptor (denoted in green) in BeWo cells. Refer to Appendix 1 for imaging parameters.*

First, cell seeding density and time were optimized to establish a confluent monolayer of BeWo cells, as increasing the seeding density or incubation time could lead to overgrowth and multilayer formation, thus hindering the functionality of the barrier [30]. As shown in Figure 4A, ZO-1 tight junction staining confirmed the formation of the barrier. After treatment with forskolin, we observed a reduction in the number of nuclei per image field (Appendix 1) and an increase in their size. The formation of syncytia was also observed, as highlighted in yellow in Figure 4A. In addition, the intensity of tight junction staining decreased, as shown in Figure 4B. All these observations are hallmarks of syncytiotrophoblast formation as reported in previous studies [69,105].

We then used a FITC-dextran transport assay to quantitatively evaluate the barrier function of the different models [72,74]. The transport of 10 kDa FITC-tagged dextran was significantly lower in the BeWo model versus in the control experiment without cells and the transport increased gradually over 24 hours to around 34% dextran transport (Figure 4C). Inclusion of a layer of endothelial cells decreased transport, which was also observed in previous studies [105], however, inclusion of endothelial cells showed no effect on 40 kDa dextran transport in a previous study by Aengenheister et al [74]. Exposure of the BeWo & HUVEC model to forskolin led to a significant increase in dextran transport, which aligns with an earlier report showing an increase in dextran transport after syncytialization, due to the smaller thickness and higher permeability of the syncytiotrophoblast[103]. However, the impact of forskolin-induced trophoblast syncytialization is a contradictory topic. For instance, Wong et al. showed no effect of syncytialization on 4kDa and 70kDa dextran transport [105], and Zhou et al. observed a decrease in dextran transport following syncytialization [102]. These two studies used the same forskolin concentration of 50 uM as we did and the differences observed might be attributed to differences in seeding time, forskolin exposure duration, and dextran concentration.

Finally, we characterized the models for FcRn receptor expression which plays a principal role in the transport of IgG antibodies from the mother to the fetus [106,107], which we are employing as a parameter to induce IgG transport in this study. Our immunostaining experiments confirmed the expression of the FcRn receptor in the trophoblast cells used, as shown in Figure 4D. Altogether, we validated the models for barrier function and FcRn receptor expression allowing us to conduct transport studies of LNPs using these models.

3.3 Cell viability on exposure to LNPs

Prior to conducting a thorough transport study, it was important to screen HUVEC and BeWo cells for cell viability after exposure to LNPs. First, interference between LNPs and the different assay reagents was checked, and no interference was detected. We then measured HUVEC and BeWo cell viability following 24 hour exposure to different concentrations of four LNPs formulations representing the diverse chemical compositions and significantly different in zeta potentials and pKa were measured. We used two assays, namely ViaLight and Calcein assays. The ViaLight

bioluminescent assay detects cellular ATP levels, while the Calcein AM fluorescent assay depends on endogenous esterase activity and plasma membrane integrity. Negative controls (normal media) and positive controls (triton-x 100 treated) were included in all the experiments, representing 100% and 0 % viability, respectively.

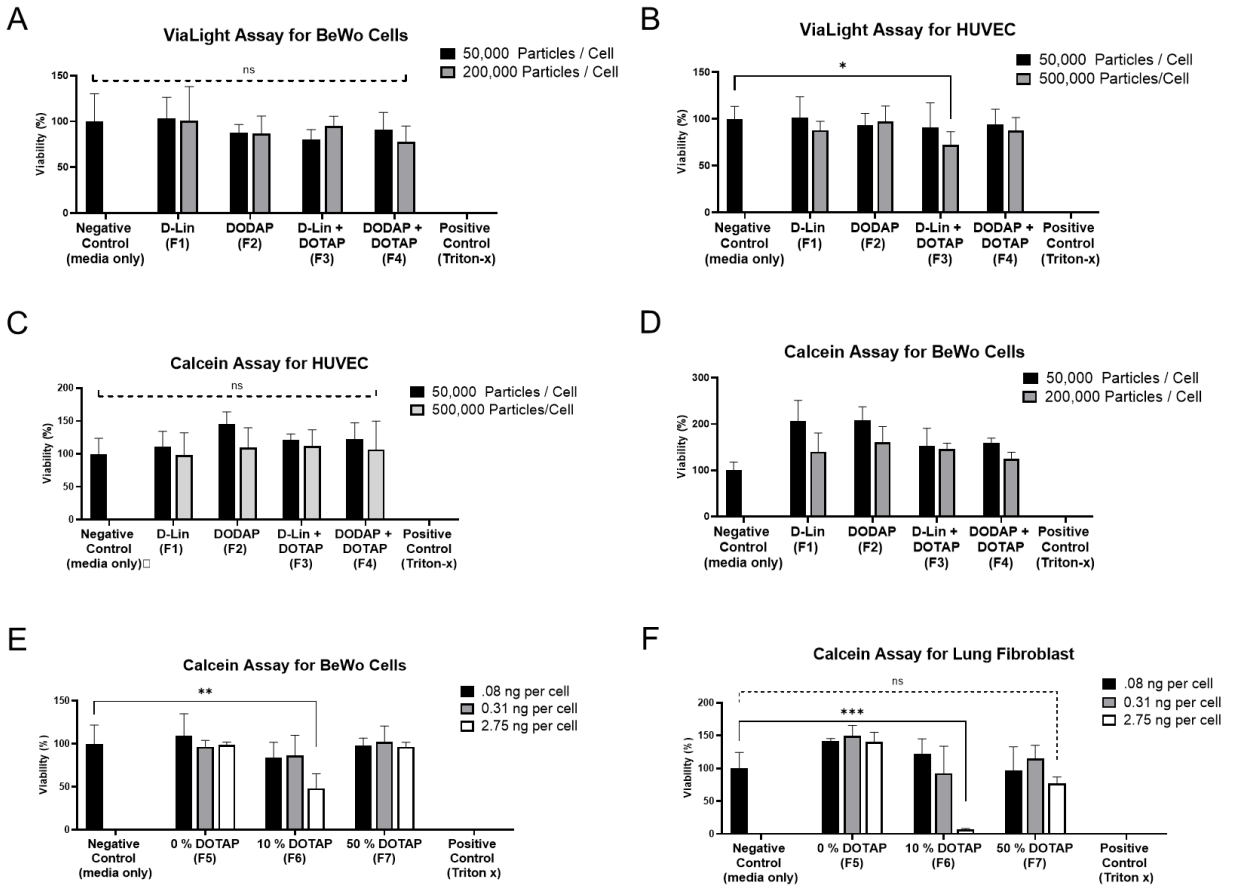

Figure 5: *Cell viability of different cells on exposure to LNPs for 24 hours using different viability assays. Data (n=6) are presented as mean ± SD and ns denotes non-significant difference. * (p<0.05); ** (p<0.01); for (p<.001) denote different levels of statistical significance. Culture media and Triton X-100 were used as negative and positive controls, respectively. (A) Viability of BeWo cells on exposure to different LNPs formulations using ViaLight Assay. (B) Viability of HUVEC cells using ViaLight assay. Viability of (C) HUVEC cells and (D) BeWo cells on exposure to different LNPs formulations using Calcein AM assay. (E) Viability of BeWo cells on exposure to LNPs with different molar percentage of DOTAP using Calcein AM assay. (F) Viability of fetal lung fibroblasts on exposure to LNPs with different molar percentage of DOTAP using Calcein AM assay. The formulation ID number is included between brackets in each figure. Please refer to Appendix 2 for the detailed description of the LNPs composition and the physicochemical characteristics of each formulation*.

Cell viability was relatively high for all tested formulations ranging from 72% to 100% or more. The increased mean viability of cells after 24 hour LNPs exposure could be due to cell proliferation over

time in the presence of phospholipids and cholesterol naturally present in cell membranes of mammalian cells, as shown in Figures 5C, 5D, and 5F [108,109]. This result could also be explained by the hormesis effect; which implies a biphasic dose-response where low dose can lead to beneficial effect while the high dose can be toxic [110]. No significant difference in cell viability was observed for all tested LNPs, except in HUVEC cells exposed to LNPs formulation F3 (D-lin + 50 % DOTAP) at a concentration of 500,000 particles per cell concentration. In this case, the mean cell viability was 72% when analyzed using ViaLight assay, but there was no significant difference compared to the negative control when analyzed using Calcein AM assay as shown in Figure 5B and 5C, respectively. Transport experiments included only LNPs concentrations in the safe (non-toxic) range.

Cell viability assays were also needed to determine the concentration range for LNPs formulations used for siRNA transfection assays included in our study. Formulations with different molar ratios of cationic lipid DOTAP were tested at different concentrations on BeWo Cells and lung fibroblasts, as shown in Figures 5E and 5F. The concentrations tested were 0.08, 0.31, and 2.75 ng per cell. The F6 formulation (with 10 % DOTAP) showed significant toxicity to BeWo cells and lung fibroblasts as shown in Figure 5E and 5F, but only at the extremely high concentrations of 2.75 ng per cell. Nanoformulations containing permanently cationic lipids were previously shown to induce cell toxicity at high concentrations, as they destabilize the cell membrane and inhibit the Na+/K+ pumps [111,112]. Therefore, 0.08 and 0.31 ng per cell concentration were selected for the next transfection experiments following the transport study; considering a lipid to siRNA mass ratio of 40, these concentrations would translate to siRNA concentrations of 10 nM and 40 nM per well (0.35 mm^2).

3.4 Formulation composition and placental barrier design affects LNPs transport.

We then conducted an extensive transport study for the different formulations using the BeWo only model unless otherwise indicated; the BeWo & HUVEC and the syncytialization models were investigated with several formulations. In all of the conducted experiments, the percentages transport were normalized relative to a corresponding control LNPs formulation tested at the same time. This control formulation has D-lin MC3 as the ionizable lipid, DSPC as the helper lipid, cholesterol, DSPE-PEG_{2000} as the PEGylated lipid, DSPE-PEG-COOH as the functionalized PEGylated lipid, and DOPE-Liss Rhod at molar percentages of 49.75, 9.95, 38.3, 1, 0.5, and 0.5 respectively.

IgG functionalization was the first parameter to test as our team has published that IgG conjugated chitosan nanoparticles can leverage the neonatal FcRn receptor to increase transport across the placental barrier [72]. The crystallizable fragment Fc fragment of IgG induces the transplacental transport via binding with the FcRn receptor in the placental barrier [113]. On the contrary, another study by Gruber et al. showed that incubating polystyrene nanoparticles with IgG did not improve placental transport [114]. Therefore, it was necessary to test IgG functionalization as a mechanism for fetal delivery using LNPs as the gold standard for nucleic acid delivery, and to optimize the IgG-conjugated LNPs formulation to induce the highest LNPs transport across the placenta. The different results in transport of IgG treated nanoparticles could be related to the different orientation of the surface IgG, in addition to the different physicochemical parameters of the nanoparticles in both studies.

Therefore, we decided to test how the orientation of IgG attached to the surface of LNPs plays a role in dictating the transport of LNPs across the placental barrier. We hypothesized that high binding to the FcRn receptor is facilitated when many surface IgG have their Fc portion remain free, non-substituted and directed toward the outer part of the conjugated protein to interact with the receptor.

To this end, we prepared different LNPs incorporating 0.5 molar percentage of functionalized PEG-lipids with various terminal functional groups, namely carboxylic acid, amine, and Maleimide, and used different reactions to conjugate IgG to the LNPs with different dominant IgG orientations. As shown in Figure 6A, the formulations with DSPE-PEG-COOH and DSPE-PEG-Maleimide showed a significant increase in transport when conjugated with IgG. Since these formulations react with the available primary amines at the end of the Fab portion or the 20 lysine residues available across the IgG chain [115-118], this can reduce the steric hindrance near the Fc portion, resulting in more availability for the interaction with the FcRn receptor. However, the formulations with DSPE-PEG-NH2 react with the carboxylic acid groups in the Fc portion [119], leading to steric hindrance that could reduce the interaction with the FcRn receptor. Surprisingly, these formulations showed a significant decrease in transport by 25 % when conjugated with IgG relative to control unconjugated LNPs. This could be attributed to the different physicochemical properties of these LNPs versus controls.

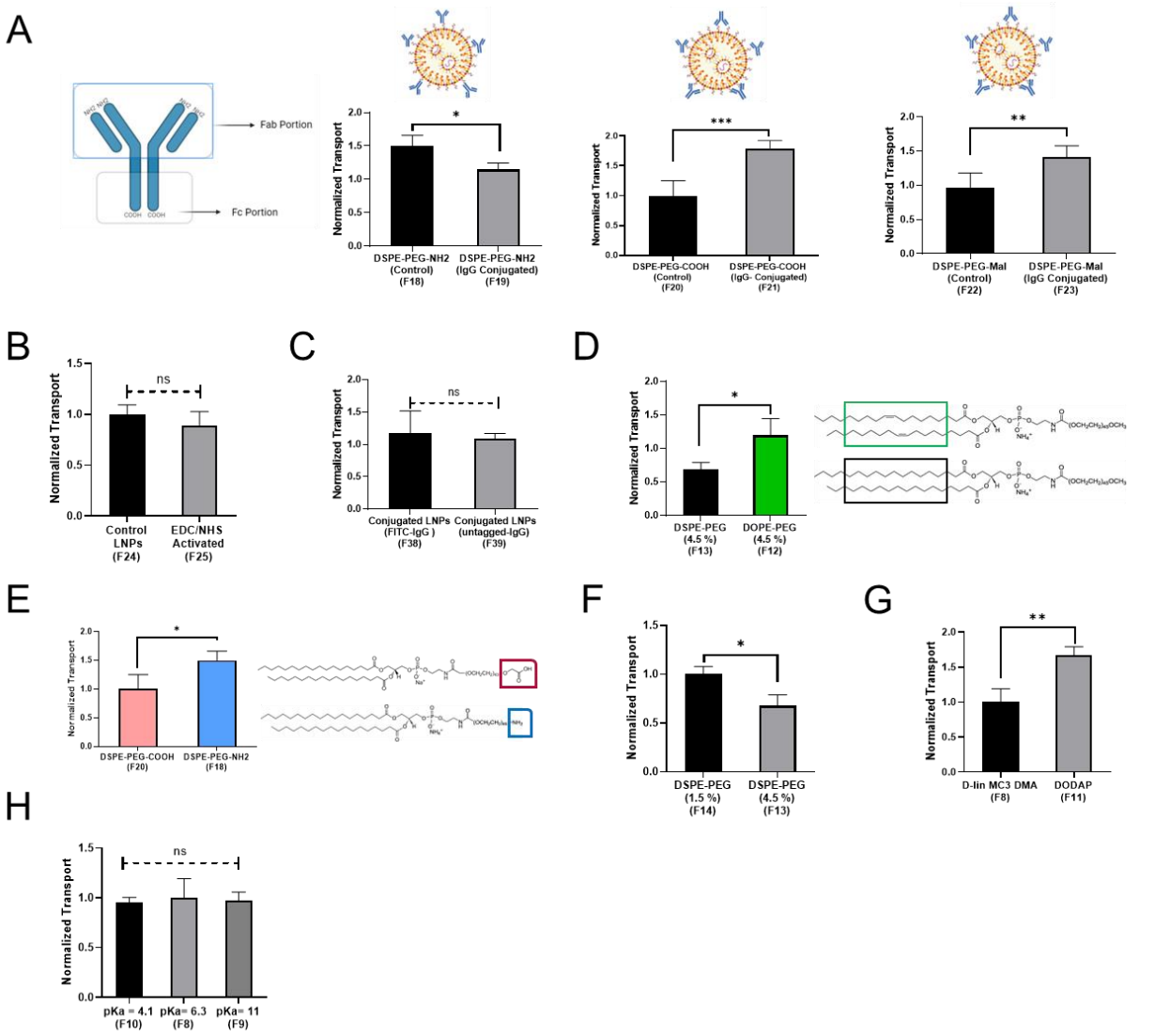

Figure 6: *The effect of LNPs formulation composition on LNPs placental transport. (A) The structure of Immunoglobin G (IgG) antibody and the effect of IgG orientation on the placental transport of different IgG-conjugated LNPs versus unconjugated LNPs; Created with BioRender.com. (B) The effect of EDC/NHS activation on LNPs transport. (C) The effect of IgG labelling on placental transport. (D) The effect of PEGylated lipid tail unsaturation on transport. (E) The effect of PEGylated lipid end-functional group on transport. (F) The effect of molar percentage of the PEGylated lipid. (G) The effect of ionizable lipid on transport. (H) The effect of LNPs apparent pKa on transport. To normalize transport results along our study, we divided the percentage transport of every studied formulation by the percentage transport of a control LNPs formulation that was used across all the experiments. The formulation ID for LNPs is included between brackets in each figure. Please refer to Appendix 2 for the detailed description of the LNPs composition and the physicochemical characteristics of each formulation. Data are presented as mean ± SD and ns denotes non-significant difference. * (p<0.05); ** (p<0.01); for (p<.001) denote different levels of statistical significance.*

For formulations containing DSPE-PEG-COOH, the carboxylic acid groups were activated by EDC and sulfo-NHS to form an intermediate NHS ester before IgG conjugation. Although this NHS ester is stable for a short time at physiological pH [120], we wanted to test if potentially free esters not functionalized with IgG have any contribution to the transport results. So, we compared the transport of EDC/NHS-activated LNPs to that of control LNPs. We observed no effect on transport, as shown in Figure 6B. Further, previous studies have pointed out that antibody labeling can affect the antigen-binding specificity [121]; the fluorescent IgG has around three FITC molecules per one IgG according to the manufacturer's information. We, however, observed no significant difference in percentage transport of LNPs conjugated with FITC-labelled IgG when compared with LNPs conjugated with unlabeled IgG, as shown in Figure 6C.

We then investigated the impact of type and percentage of PEGylated lipids as they are key components of LNPs and are included in all FDA-approved LNPs [122], but their type and percentage are usually varied between formulations. Also, the impact of PEGylated lipids on the physicochemical parameters of nanoparticles, their transfection efficiency, cellular uptake of nanoparticles, and their pharmacokinetics have been established [35]. However, the impact of the type and percentage of PEGylated lipid remains to be investigated in regards to LNPs transport across the placenta.

The PEGylated lipid consists of three main components: the lipid tail, PEG chain, and the PEG-end-functional group. The PEGylated lipid characteristics are influenced by the length and saturation of the hydrophobic tail. Both have a critical effect on the packing of the lipids and the phase transition temperature. As the phase transition temperature decreases, the PEGylated lipid dissociation from the formulation, or dePEGylation, increases [35,123]. We therefore compared the transplacental transport of LNPs with two different PEGylated lipids, DSPE-PEG and DOPE-PEG. Both have the same head group and tail length but differ in the degree of tail unsaturation (Figure 6D). Interestingly, introducing unsaturation, two double bonds, in the lipid tail for DOPE-PEG led to a significant increase in the transport of the LNPs by 75%. This could be interpreted by the faster dissociation of DOPE-PEG from the LNPs leading to higher chances for permeation and transport.

Despite being used in a small percentage in our LNPs formulations, the PEGylated lipid-end functional group had a major impact on LNPs' transport. Replacing 0.5 % DSPE-PEG-COOH with

0.5% DSPE-PEG-NH2 in our LNPs formulation has led to a significant increase in LNPs transport by 51 %, as shown in Figure 6E. This is most likely due to the increase in zeta potential from -13.1 to +6.6, respectively.

We also investigated the impact of PEGylated lipid percentage on LNPs transplacental transport. In Figure 6F, two formulations with the same components but different PEGylated lipid percentages were tested, and the increase in the PEGylated lipid percentage from 1.5 % to 4.5 % led to a significant reduction in transplacental transport. This could be due to lower cellular uptake, as observed in our cell association study in Figure 10B, or decreased permeation through the tight junctions. An increase in PEGylated lipid percentage has also been shown by others to decrease mRNA transfection [124].

Ionizable lipids are the major component of an LNPs formulation, usually constituting a molar percentage ranging from 40-50 % per LNP. Ionizable lipids play an essential role in the endosomal escape of LNPs [25] and changing the type of the ionizable lipids can alters the physicochemical properties of LNPs, such as zeta potential and pKa, impacting LNPs transfection efficiency, toxicity and biodistribution [21]. As shown in Figure 6G, replacing the D-lin MC3 ionizable lipid with DODAP led to a significant increase in transport by 67 %. This could be attributed to the difference in zeta potential and/or pKa, since incorporation of DODAP instead of D-lin MC3 in LNPs formulation has increased the zeta potential and pKa from -14.4 to +7.8 mv and 6.26 to 6.84, respectively.

Incorporating permanently charged lipids in LNPs, or selective organ targeting technology (SORT), led to promising results for extrahepatic delivery. Specifically, adding 50% DOTAP or 30 % 18:1 PA to the standard formulation of Onpattro resulted in preferential accumulation in the lung or spleen, respectively [40]. This change in biodistribution was attributed to the difference in the pKa of the LNPs [39]. However, in our study, LNPs with various pKa values, 4.1, 6.3 and 11, showed no significant differences in transplacental transport, as shown in Figure 6H.

Aside from the composition of LNPs formulations, we investigated the impact of different parameters related to the cell model used, namely cell seeding density, IgG concentration in the culture medium and trophoblast syncytialization.

Optimizing the seeding density is an essential step for barrier formation to ensure the formation of a confluent monolayer [30]. For example, a seeding density of 1 million cells per cm^2 showed multilayer formation, while 30 thousand cells per cm^2 had few gaps after 3 days. The 100,000 cells per cm square is a typical seeding density in placental barrier formation studies [105]. When one LNPs formulation was assessed at the different seeding densities, it showed a significantly lower transport percentage at the high seeding density, as shown in Figure 7A. This decreased transport most likely results from the trapping of the nanoparticles at the tight junctions, which is an expected behavior for tightly packed cells [125].

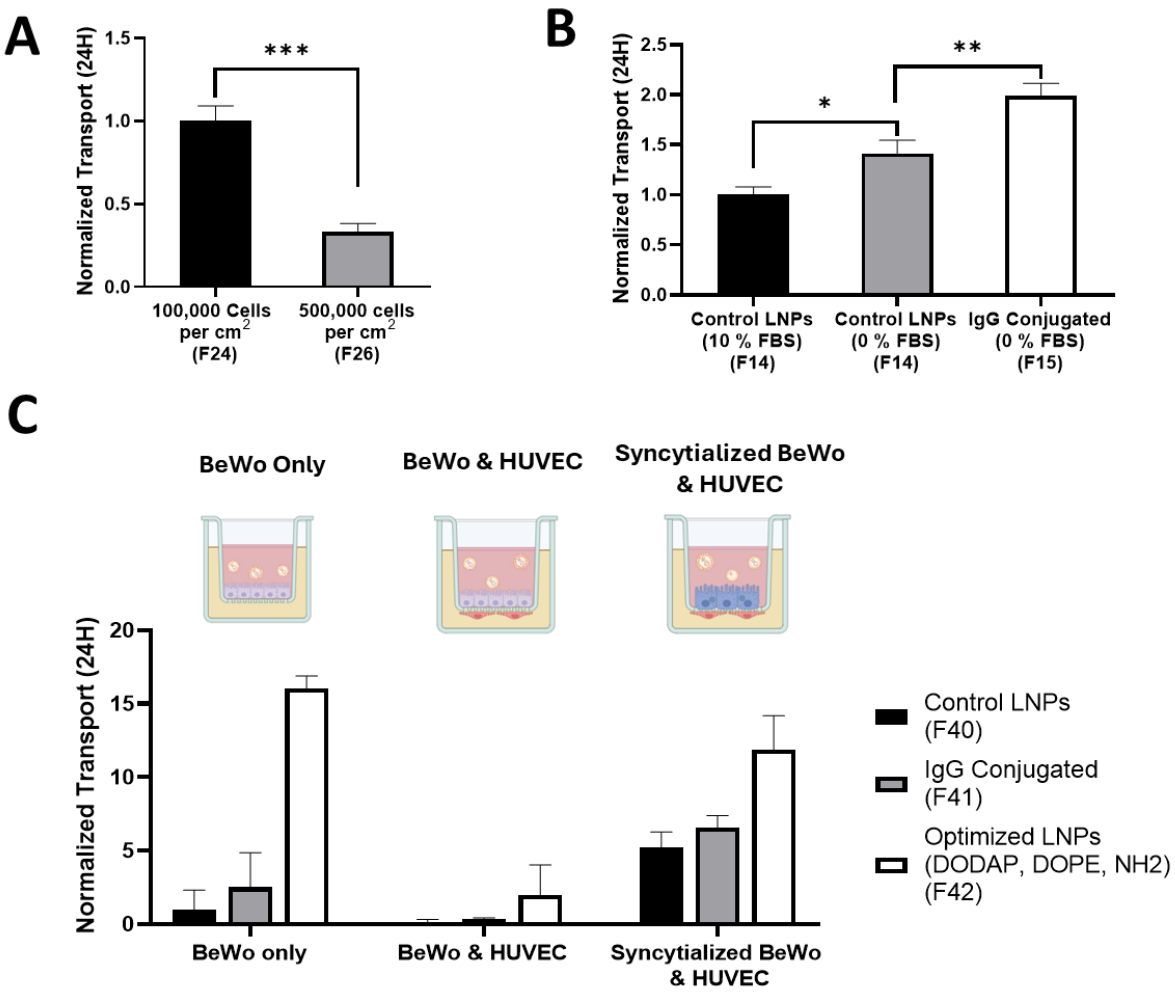

Figure 7: *The placental barrier design features affect LNPs transport at 24 hours. (A) The effect of BeWo cells seeding density on LNPs transport. (B) The effect of the percentage of fetal bovine serum (FBS) in the culture media on placental transport. (C) The transport of different LNP formulations across the different placental models. To normalize transport results in our study, we divided the percentage transport of every studied formulation by the percentage transport of a control LNPs formulation that was used across all the experiments. The formulation ID for LNPs is included between brackets in each figure. Please refer to Appendix 2 for a detailed description of the composition and characterization of each formulation.*

We previously demonstrated the importance of the media IgG concentration when targeting FcRn receptor to induce transplacental transport, as the free IgG can compete with the IgG-conjugated nanoparticles [72]. Since the fetal bovine serum (FBS) contains a high percentage of IgG, we studied LNPs transport in the control media (F12K containing 10% FBS) and a growth media containing only bovine serum albumin (F12K with 0% FBS). Surprisingly, control LNPs showed higher placental transport in the case of (0 % FBS), compared to (10% FBS), as shown in Figure 7B; it could be due to the significant reduction in tight junction formation, as indicated by ZO-1 expression in Appendix 1. Besides, this difference in transport could be attributed to the different protein corona that can form

on LNPs in the two medias, as suggested by Gruber et al [114]. IgG conjugation further increased LNPs transport ($p < 0.01$) compared to control LNPs.

The fusion of placental trophoblast cells leads to the formation of the syncytiotrophoblast consisting of an interconnected cytoplasm containing multiple nuclei. Syncytialization is critical for a successful pregnancy, as it enables the interchange of substances between the mother and fetus, without transplacental passage through the intercellular junctions, in addition to other placental functions [126]. The effect of syncytialization on the transplacental transport of nanoparticles is still understudied. This represents a knowledge gap in how the nanoparticles interact with the placenta at the different stages of pregnancy. We tested different LNPs formulations in three placental models, as shown in Figure 7C. Syncytialization has resulted in a significant increase in the transport for all the LNPs formulations compared to the BeWo & HUVEC model. Besides, the difference in transport between the different LNPs formulations was reduced on induction of syncytialization. For instance, the optimized LNPs formulation F42 showed 126% higher transport when compared to the control formulation (F40) in the syncytialized model. This contrasts with 1200 % and 1500 % increase in transport when using the BeWo & HUVEC and BeWo only models, respectively. This indicates an overall increase in permeability regardless of the composition of the LNPs. Combining the results of the FITC-dextran transport in Figure 4D and transport of the LNPs in Figure 7C indicates that the effect is size-independent. Dextran has an average molecular weight of 10,000 daltons, while the LNPs are millions of daltons. Our results contradict a previous study reporting the effect of syncytialization on transport to be size-dependent; Kouthouridis et al have shown statistically significant increase in 4kDa dextran transport following syncytialization, while the increase in 65 kDa dextran transport was not statistically significant [103]. Besides, they attributed the transport increase to the smaller thickness and increased permeability of the syncytiotrophoblast layer compared to trophoblast cells [103]. However, we didn't observe a decrease in the thickness of the BeWo layer after syncytialization, as shown in Appendix 1. Additionally, we're suggesting that what drives higher placental transport, in the case of syncytialization, is the increase in cellular permeability or cellular uptake. As we observed higher LNPs uptake into the BeWo and HUVEC cells, as shown in our LNPs association study in Figures 10I and 10H, respectively.

In summary, our comprehensive transport studies highlight the multifaceted factors influencing transport of LNPs across the placental barrier, including the impact of IgG functionalization, PEGylated lipid characteristics, ionizable lipids, and cell model variations. Our findings indicate that both the composition of LNPs and the conditions of the placental model significantly affect transport efficiency. However, our studies could not answer what features of the LNPs and cell model were most important for transplacental transport. For example, is LNPs composition more predictive than IgG functionalization or any of the other studied features? To this end, we used machine learning to investigate the impact of these LNPs features on their transplacental transport.

3.5 Machine Learning Modeling for Placental Transport and Transport Kinetics of Lipid Nanoparticles

As mentioned earlier, ML models show promise in analyzing the dataset to provide valuable insights, which can guide the design of future experiments. In this study, the ML approach was employed as a means of analyzing the key attributes to LNPs transport. ML models were trained on an experimental dataset with 189 data points, each representing 3 to 5 replicates, including 18 characteristic input

features describing the transplacental transport. The overarching goal of these ML experiments was to address the multidimensional nature of LNPs transport that cannot be retrieved by single factor experiments.

First, we refined the dataset to remove any transport experiments with missing inputs or remove highly dependent features. The refined dataset included 48 distinct transport experiments with 18 input features; the used dataset is attached in Appendix 3. A selection of ML models was trained on this refined dataset using the leave-one-out cross-validation technique, which ensures comprehensive data utilization, a valuable approach for such relatively small datasets. The models' accuracy was evaluated according to four metrics: MAE, MedAE, RMSE, and MSE, as shown in Appendix 1. The model, achieving the lowest error in most of these metrics, was chosen for further analysis. The Random Forest (RF) model showed the highest accuracy (lowest error) for predicting the studied outputs: 24H transport percentage, t-half and k-value, as detailed in Appendix 1.

Shapley Additive Explanations (SHAP) was used to rank the feature importance from top (highest) to bottom (lowest). The color represents the input feature value; if the feature values are continuous, the blue color represents low values, while red represents high values. However, if the input feature has categorical values, as in the case with the ionizable lipid type or the PEG-end functional group, the color is assigned as detailed in Figure 8E. The accuracy and reliability of the ranking diminish as you move down in the figure. Therefore, our discussion is focused on the top features in each graph to avoid over-interpretation.

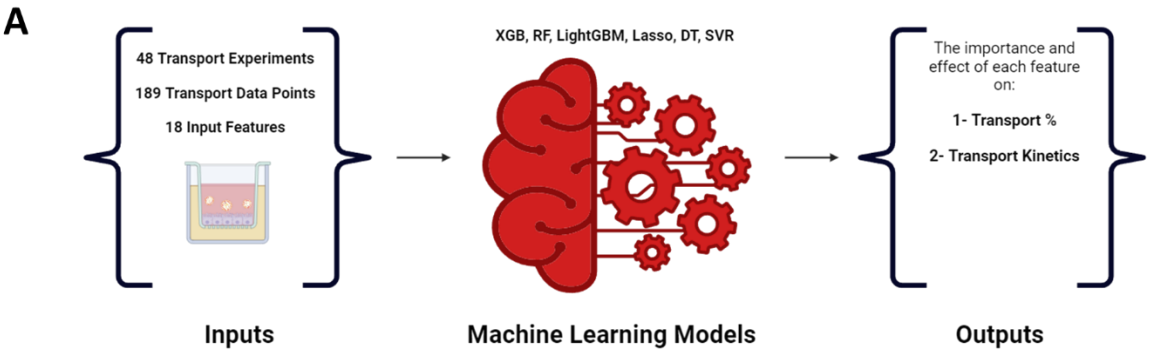

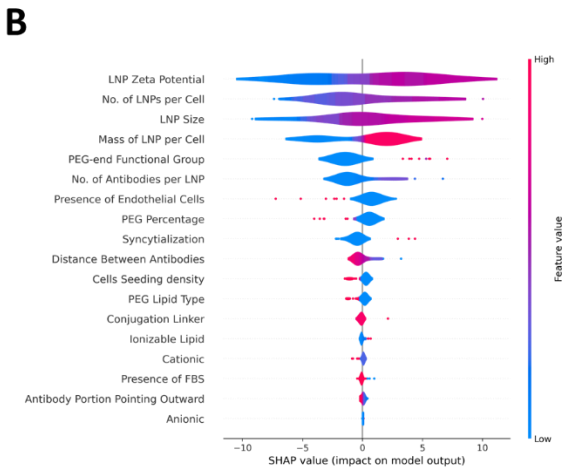

24 H Transport (%)	Mean	Min	Max
	26	0.49	87.5

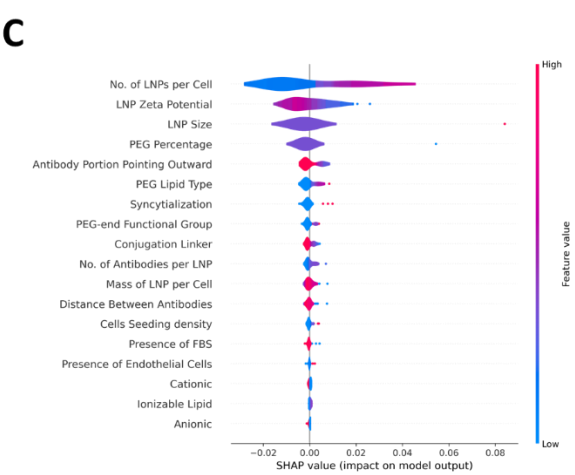

K-value	Mean	Min	Max
	0.104	0.046	0.328

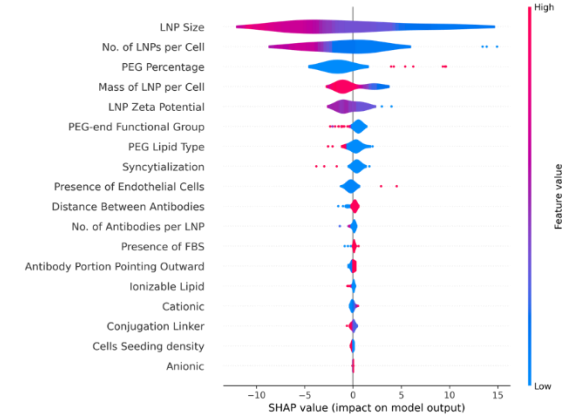

T- half (hours)	Mean	Min	Max
	37.4	6.6	75.6

E

Categorical Variables			
Feature Value	Low	Med	High
PEG-end Functional Group	COOH	Maleimide	NH2
PEG Lipid Type	DSPE-PEG		DOPE-PEG
Ionizable Lipid	D-lin MC3		DODAP
Syncytialization	No		Yes
Presence of Endothelial Cells	No		Yes
Presence of FBS	No		Yes
Antibody Portion Pointing Outward	Fc		Fab
Conjugation Linker	Carboxyl NHS		Thiol- Malemide

Figure 8: *Machine Learning Modelling for Percentage Transplacental Transport at 24h and Transport Kinetics. (A) Schematic describing the dataset and the employed machine learning algorithms used for modelling; Created with BioRender.com. (B) SHAP figure ranking the predictors of the percentage*

transport at 24 hours, using Random Forest (RF) model. (C) SHAP figure ranking the predictors of the transport constant, k-value, of the logistic growth kinetics model, using RF model. (D) SHAP figure ranking the predictors for the t-half of the logistic growth kinetics model, using the RF model.

We initially used percentage transport at 24 hours as the output for one of the ML models since it was consistent timepoint across all the transport experiments. The mean value for the 24-hour time points in the dataset was 26%. Interestingly, the zeta potential of LNPs was found to be the most critical feature in predicting the total transport percentage, as shown in Figure 8B. This means that, in the context of this study, high zeta potential is one of the key attributes for high placental transport, while low zeta potential is a predictor for low transport. These observations align with the literature, which reports positively charged NPs tend to interact with the negatively charged cellular membrane, tight junctions, or serum proteins, which could play a role in the transport process [127]. Previous studies that assessed two or three formulations with distinct zeta potential have found no effect from surface charge on transplacental transport of other types of nanoparticles [76,128]. However, our ML model that is based on a dataset which includes several formulations covering a wide range of zeta potentials, has provided validated conclusions and suggests the Zeta potential in future NPs transport studies needs to be carefully considered. Based on our machine learning models illustrated in Figure 3E, the lipids that most significantly influence zeta potential are, in order: permanently charged lipids, functionalized PEGylated lipids, and ionizable lipids.

Another important feature for percentage transport at 24 hour was LNPs size, with bigger sizes leading to increased transport and smaller sizes leading to decreased transport. This contradicts previous studies that showed the opposite correlation [88]. We think our conclusion here can't be generalized to other NPs, but it is specific to our dataset. In our dataset, LNPs with bigger sizes are IgG-conjugated LNPs, while LNPs with high PEGylated lipid percentage have smaller sizes. Also as shown in Figure 3F, the number of IgG antibodies per LNP was the most critical contributor to LNPs size, and the size increased with a higher number of antibodies per LNP. Finally, the number of LNPs per cell and the mass of LNPs per cell emerged as the second and fourth predictors for transport, respectively. This finding should be considered in dose choices for future studies developing fetal gene therapies or toxicological studies assessing environmental exposure to nanoparticles.

Additionally, we presented the transport data as the average apparent permeability, as described in the methods. This dataset was modeled for this output and is shown in Appendix 1. Since the average apparent permeability calculations considered earlier time points, not just at 24 hours, the top predictors in both models were similar but appeared in a different order. LNPs size was shown as the best predictor for permeability while the zeta potential of LNPs was shown to be the second most influential feature.

To better understand the transport process, we studied the kinetics of transport of LNPs by tracking them at several time points up to 24 hours. The transport data fit the best to the logistic growth model, which showed lower errors (higher R^2) compared to other tested kinetics models. From the refined transport dataset, 44 experiments followed the logistic growth model enabling us to calculate the k and t-half. The parameter k stands for the rate constant of transport, while t-half represents the time, in hours, to reach half of the maximum concentration. Also, t-half stands for the inflection point where the growth rate is maximal. The ML models were trained on these transport kinetics parameters; the k-values and t-half values serving as the outputs.

SHAP figures were created for k and t-half, as shown in Figures 8C and 8D, respectively. From the logistic growth model equation (eq: 4), the k values were inversely proportional to the t-half values. Therefore, the impact of an input feature can have an opposite effect on these two outputs. The LNPs size and zeta potential were among the top five predictors in both models, suggesting their predominant effect on transport kinetics.

Interestingly, the molar percentage of the PEGylated lipids appeared as one of the important features for predicting t-half (Figure 8D). As the molar percentage of the PEGylated lipids increases, the time required to reach half of the maximum concentration also increases. This new finding emphasizes the critical role of the dePEGylation step to facilitate transport across the placental barrier.

Another interesting result from the k model (Figure 8C) is that the number of particles per cell was the most important feature for predicting the rate constant of transport, while the mass of LNPs per cell had little to no effect. Even though both represent the dose of LNPs, the number of particles was more predictive of the biological effects. It demonstrated the importance of reporting the dose of nanoparticles doses as a number concentration. Ouyang et al. have similarly reported the significance of the absolute number concentration of nanoparticles to achieve targeting, demonstrating that a minimum threshold of one trillion nanoparticles per mouse is required to enhance non-liver targeting [129]. With the increasing adoption of counting techniques, such as the Nanoparticle Tracking Analysis (NTA), we anticipate broader adoption among researchers to consistently report the absolute number concentration of nanoparticles in their dosages. This practice will significantly improve future studies on the interaction of nanoparticles with the placenta and other biological barriers by providing accurate and precise number concentration data of nanoparticles.

To validate the effects of these features on LNPs transport, we developed new formulations informed by SHAP analysis. These formulations were purposefully designed to vary across the different levels of the most important features for predicting LNPs transport at 24 hours, namely the zeta potential, number of LNPs per cell, LNPs size, mass of LNPs per cell, and PEGylated lipid end-functional group. Specifically, as shown in Figure 9A, F49 represented the unoptimized formulation, F50 was moderately optimized by manipulating three features, while F51 was highly optimized by manipulating the five features. We observed a compelling result where combining these features resulted in a synergistic effect on facilitating the transplacental transport of LNPs. As shown in Figure 9B, the moderately optimized F50 led to a 129 % increase in transport. Remarkably, the highly optimized F51 resulted in a 622% increase in LNPs transport across the placenta. To improve our understanding of this synergistic effect, we studied the cellular association of LNPs with the placental barrier. We observed a statistically significant increase in cellular association of LNPs by 23 times and 44 times for F50 and F51, respectively, as shown in Figure 9C. This suggests that the transport process of these optimized LNPs could be mediated by an initial step of placental uptake.

A

ID	Zeta potential	N of LNPs per cell	Size	Mass of LNP per cell (ng)	PEG-end Functional Group	24 H Transport %
F49	-7.1	152941	98.1	0.15	COOH	8.5
F50	8.6	550000	101.7	0.65	COOH	19.5
F51	26.7	530790	114.8	0.65	NH2	61.4

Low Feature Value Moderate Feature Value High Feature Value

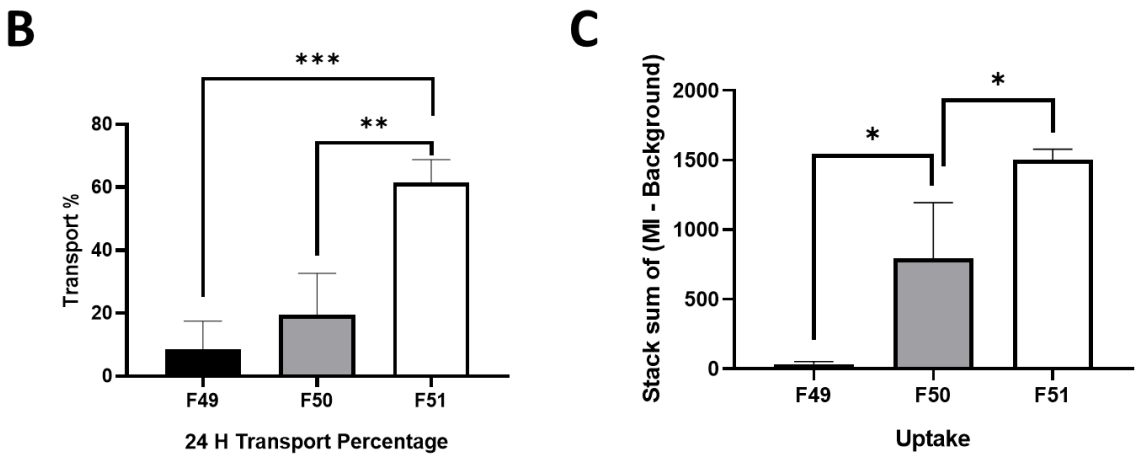

Figure 9: *Machine Learning Modelling Validation. (A) Description and results of the three formulations that were designed to validate the top five influential features on percentage transport at 24 hours. (B) The 24 hours transport percentage for the three formulations. (C) The association of LNPs with BeWo cells for the three formulations. The formulations IDs are included in each figure. Please refer to Appendix 2 for the detailed description of the LNPs formulation compositions and the physicochemical characteristics of each formulation.*

In conclusion, our comprehensive approach combining ML with experimental validation has provided deep insights into the complex dynamics of LNPs transport across the placental barrier. This integrated approach revealed distinctions between interpretations derived from the ML approach in Figure 8 and conclusions drawn from the traditional single-cause effect testing approach followed in Figure 6 and Figure 7. Using ML, we identified critical predictors such as zeta potential, LNPs size, and specific lipid compositions. We have not only refined our understanding of transport kinetics but also highlighted new strategies to optimize LNPs formulations.

3.6 Cellular Association of LNPs:

To fully understand the transport dynamics of LNPs across the placental barrier, we conducted a comprehensive cell association study. While measuring transport alone defines LNPs crossing the placenta, it does not account for the complex interactions between LNPs and placental cells. By quantifying cellular association, encompassing both uptake and adhesion to cells, we can better interpret transport results and identify the underlying mechanisms driving LNPs behavior. We used confocal imaging to measure cell uptake of LNPs following 24 hours transport and Z-stacks were quantified for fluorescence intensity. The sum of the mean fluorescence intensity of each slice was used for comparing the different experiments.

Aligned with transport results (Figure 6), PEGylated lipid tail saturation and PEGylated lipid percentage were determinants of cellular association, where higher cellular association of LNPs were observed for DOPE-PEG versus DSPE-PEG containing LNPs (Figure 10A). Also, as we increased the molar percentage of DSPE-PEG a significant decrease in cellular association was observed. Therefore, faster dePEGylation (or PEGylated lipid dissociation) could be a crucial step for cellular association of LNPs (Figure 10B). These transport and cellular uptake studies on the effect of PEGylated lipid on LNPs behavior corroborate previous studies assessing nanoparticle uptake and biodistribution [35,130]. The same was observed for the features, ionizable lipid type and IgG conjugation, however the difference in cellular association was not statistically significant (Figure 10C-E). Overall, these data suggest that cell uptake for these LNPs could be a prerequisite for successful transport across the placental barrier. The lack of significance in cellular assocaition could be due to the sensitivity limitations of image analysis based on fluorescence intensity, as we reported earlier [131,132]. Another method that compares the number of fluorescent voxels, outlined in Appendix 1, could provide more information.

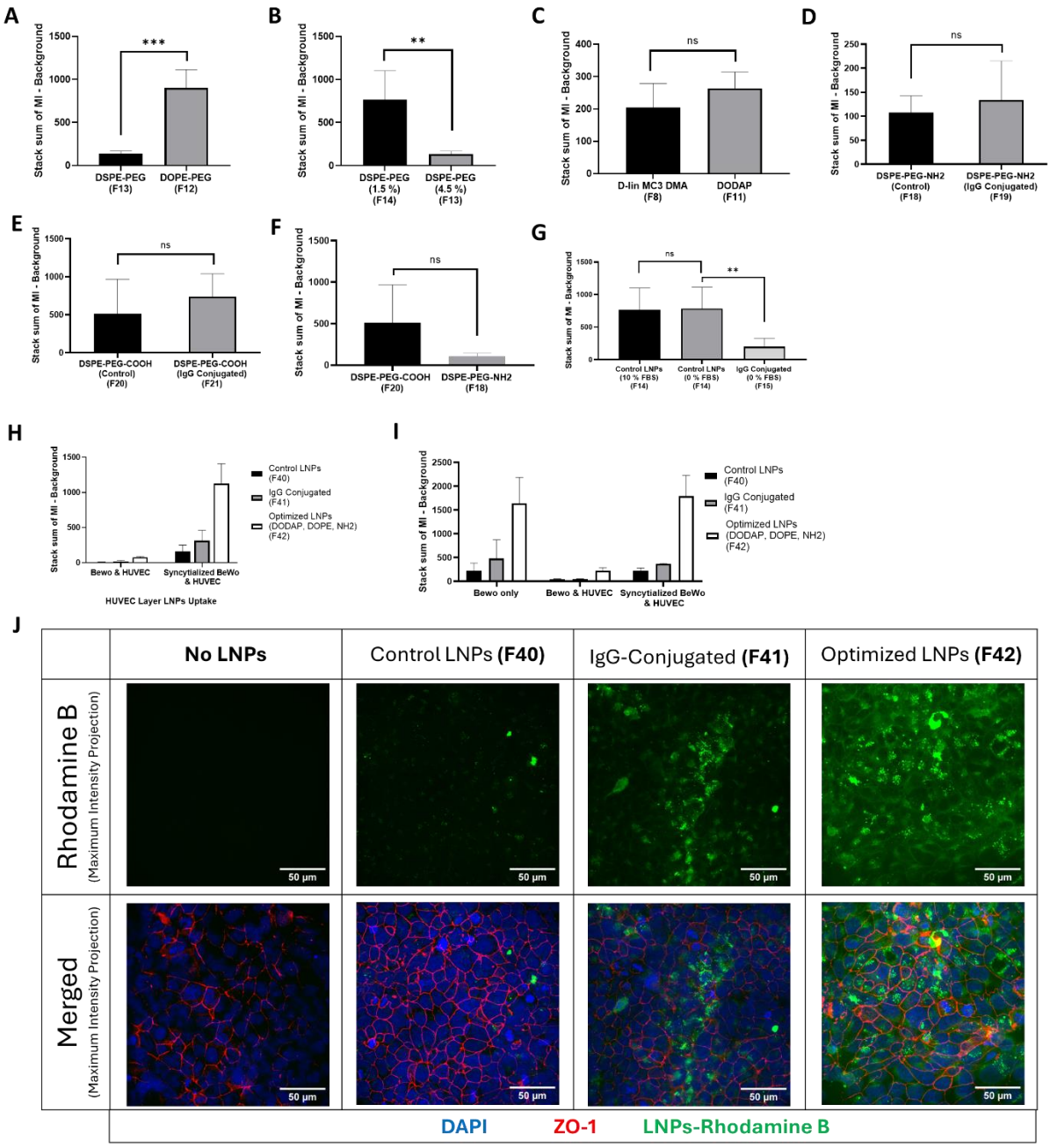

Figure 10: *Cellular association of LNPs with BeWo and HUVEC cells. The effect of (A) PEGylated lipid tail unsaturation, (B) molar percentage of the PEGylated lipid, (C) the ionizable lipid, (D) the PEGylated lipid end-functional group, (E-F) IgG conjugation, (G) percentage FBS concentration in culture media on LNPs association with BeWo cells. Association of different LNPs formulations with (H) HUVEC and (I) BeWo cells in the different placental models. (J) Representative images for cellular association of different LNPs with BeWo cells. Please refer to Appendix 2 for the detailed description of the LNPs composition and the physicochemical characteristics of each formulation.*

Interestingly, the cellular association results further strengthen our hypothesis regarding the increased cell permeability upon induction of syncytialization by forskolin. Specifically, a significant

increase in LNPs association to both placental and endothelial cells was observed following induction of syncytialization, as seen in Figures 10I and 10H. This aligns with the concomitant increase in transport observed in Figure 7C.

On the contrary, varying the PEGylated lipid end-functional group did not result in significant changes in cellular association of LNPs. This is despite the difference in transport observed between the LNPs with DSPE-PEG-COOH and DSPE-PEG-NH2. Also, we observed a reduction in cellular uptake of IgG-conjugated LNPs in IgG-deprived media (0 % FBS), as shown in Figure 10G, despite the high percentage transport of this formulation (Figure 7B). The underlying mechanisms for these observations remain unclear and warrant further investigation. One suggestion is that the end-functional group and IgG concentration in the media played a critical role in transport but were not required for initial cellular association.

In conclusion, understanding the cellular association of LNPs provides valuable insights into their transport behavior across the placental barrier and highlights the complex interplay of lipid composition and cellular interactions.

3.7 siRNA-loaded LNPs Transfection in Placental and Fetal Cells

To build on the findings from our transport study, we initiated an *in vitro* transfection study to further optimize LNPs formulations for RNA delivery to human fetal lung fibroblasts. The goal was to develop siRNA-loaded LNPs formulations that preferentially transfect fetal lung cells while minimizing transfection in off-target placental or endothelial cells.

Previously, LNPs were optimized to achieve mRNA transfection in the placental cells,[31,133] or in fetal lung cells through intraamniotic injection, vitelline vein injection, or intracerebroventricular injection [4,13]. However, developing an LNPs formulation that preferentially transfects fetal lung cells over placental or endothelial cells requires further optimization.

First, when we tested the high placental transport formulations, that included two or three of these lipids: DODAP, DOPE-PEG, and DSPE-PEG-NH2, they showed a slight increase in transfection. However, the overall efficiency was comparable to free siRNA using lipofactamine, as shown in Figure 11A. Therefore, we conducted several optimizations to improve relative transfection efficiency in fetal lung fibroblast cells to placental cells and endothelial cells

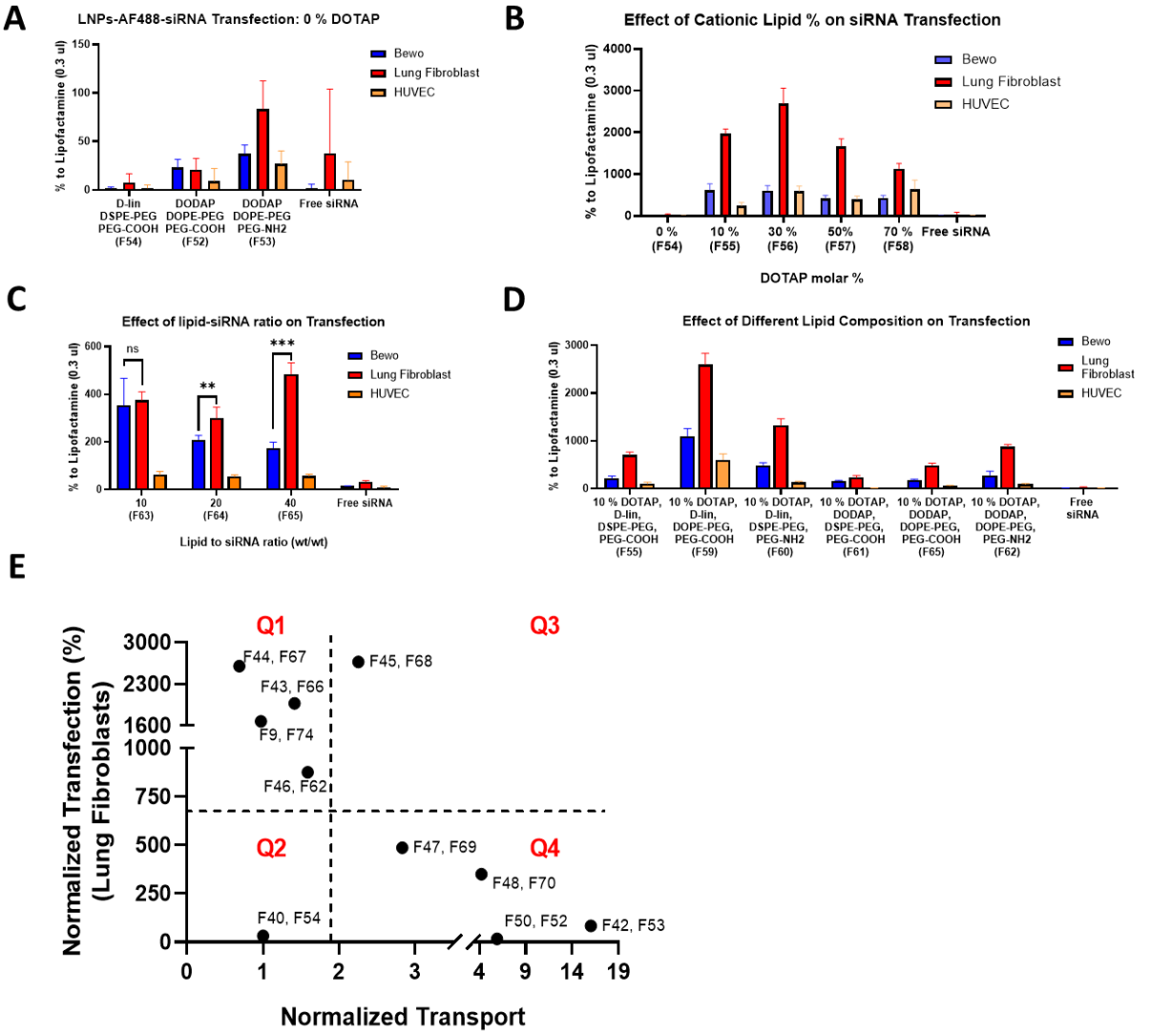

Figure 11*: Transfection of siRNA-loaded LNPs in placental and fetal cells is derived by cationic lipids, PEGylated lipids, and lipid to siRNA ratio. (A) Transfection of high-transport formulations that do not include DOTAP in their lipid composition. (B) The effect of DOTAP molar percentage on percentage transfection. (C) Effect of lipid to siRNA mass ratio on percentage transfection. (D) Optimizing formulations for high transport and high transfection by testing different compositions with lipids identified for increasing the transport. (E) The placental transport and lung fibroblasts transfection results combined; each dot represents LNPs with the same lipid composition but with 2 IDs: the first one is unloaded LNPs used for the transport experiment and the second one is siRNA-loaded LNPs tested for transfection. The dashed lines represent the median of the output and divide the performance of the formulations into 4 quadrants: Q1 is low transport & high transfection, Q2 is low transport & low transfection, Q3 is high transport & high transfection, and Q4 is high transport & low transfection. Please refer to Appendix 2 for the detailed description of the LNPs composition and the physicochemical characteristics of each formulation. Transfection results are reported as a percentage relative to the positive control (which is transfection by Lipofectamine). Data (n=6) are*

*presented as mean ± SD and ns denotes non-significant difference. * (p<0.05); ** (p<0.01); for (p<.001) denote different levels of statistical significance.*

First, we tested different LNPs to siRNA mass ratios. A mass ratio of 40 (formulation 65) showed significant transfection in lung cells compared to placental cells, while a mass ratio of 10 (formulation 63) showed no differences, as shown in Figure 11C. Therefore, the ratio of 40 was utilized for all subsequent formulations. This confirms previous studies that showed that increasing the N/P ratio (the ratio between lipid and RNA) results in preferential transfection of the lung cells [134].

To further increase the transfection percentage in lung cells, LNPs with different molar percentages of DOTAP were tested. Recent studies have shown that permanent cationic lipids, such as DOTAP, can increase mRNA transfection into lung cells as they raise the LNPs pKa above 7 [39]. As shown in Figure 11B, DOTAP molar percentages of 10 and 30 achieved the highest transfection percentage in fetal lung cells. However, increasing the DOTAP percentage beyond this resulted in a reduction in the number of viable cells. Therefore, 10 % DOTAP was included in subsequent formulations to achieve high transfection while keeping high molar percentages of the other lipids driving transport

Following determination of the optimal DOTAP molar percentage of 10 and the optimal LNPs to siRNA mass ratio of 40, we tested the impact of other lipid components shown to drive high placental transport, on transfection efficiency. Similar to the transport results, replacing DSPE-PEG-COOH with DSPE-PEG-NH2, or replacing DSPE-PEG with DOPE-PEG resulted in a significant increase in transfection, mainly due to the increase in zeta potential or more rapid de-PEGylation [35], respectively (Figure 11D). However, contrary to the transport results, replacing D-lin-MC3 with DODAP led to a significant reduction in transfection. Therefore, the lipids driving high placental transport are not necessarily the same ones leading to high fetal cell transfection. So, a balance between both is required. It should be also noted that these transfection experiments were conducted at a dose of 4 picomole siRNA per well (0.35 mm^2). To investigate the impact of siRNA dose on transfection efficiency, we tested a smaller dose of one picomole of siRNA per well (Appendix 1). Similar transfection results were obtained indicating that the behavior of LNPs can be dose-independent.

The ten LNPs formulations tested separately for placental transport and fetal lung transfection were plotted based on their measured 24-hour transport and transfection results (Figure 11F). The median for the two outputs (transport and transfection) was graphed dividing the overall output of the LNPs formulations into four quadrants, Q1 (high transfection and low transport), Q2 (low transfection and low transport). Q3 (high transfection and high transport) and Q4 (low transfection and high transport). Among the different formulations, F68 composed of (DOTAP, D-lin MC3, cholesterol, DSPC, DOPE-PEG, and DSPE-PEG-NH2) were shown to efficiently cross the placental barrier and to transfect fetal lung cells.

3.8 Combined Transport-Transfection Study

Formulations representing the different quadrants (Q1, Q2, Q3 and Q4 - Figure 11F) were tested in a combined transport and transfection placental model shown in Figure 12A. This model ensures that LNPs are intact and capable of transfecting fetal lung cells after passing through the placental barrier. A similar high-throughput set-up to test the LNPs integrity was utilized in a previous study modeling the blood-brain barrier [30].

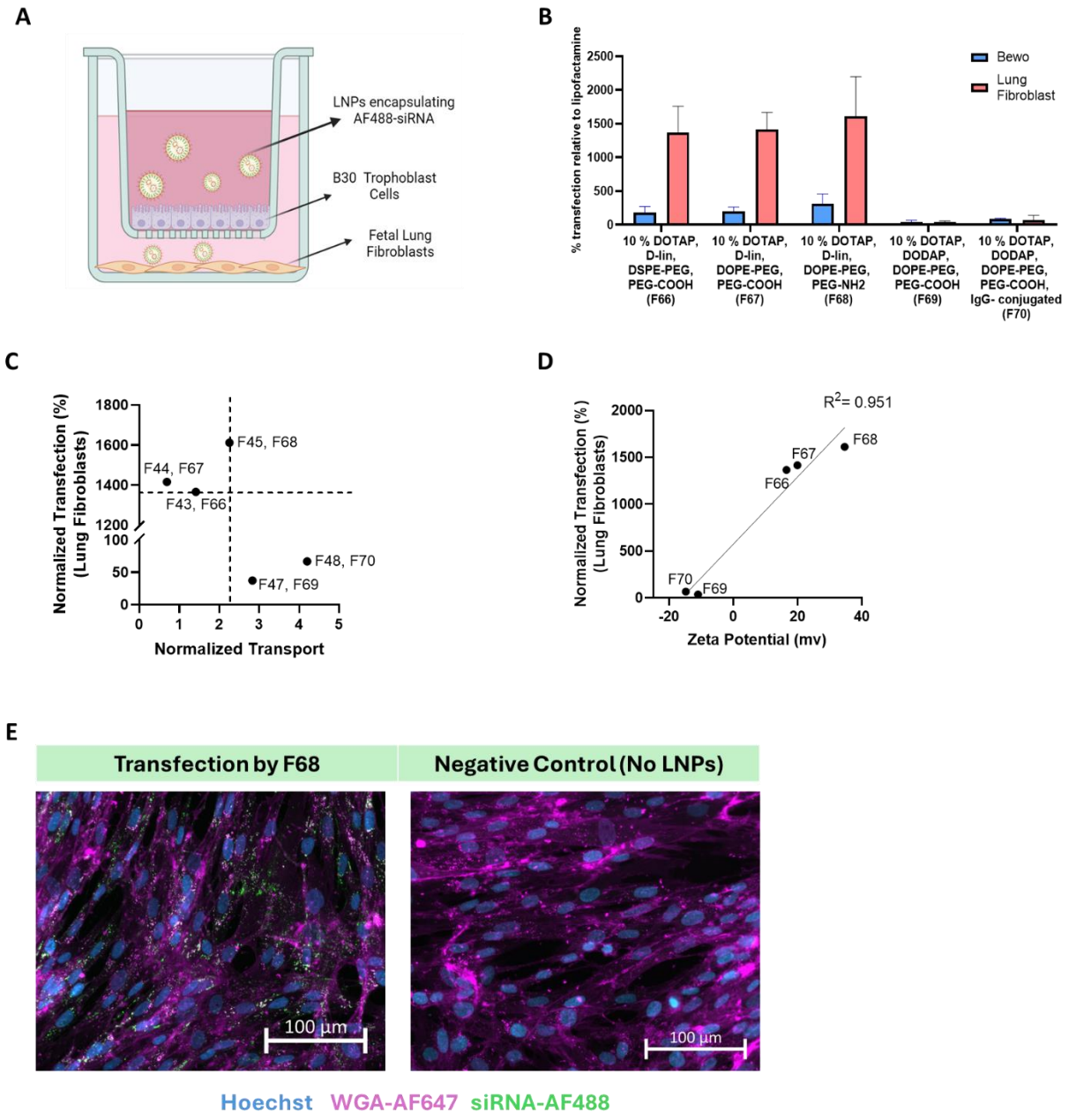

Figure 12: *Combined Transport-Transfection Model. (A) A Schematic for the combined model with BeWo cells seeded on the transwell membrane in the apical compartment and fetal lung fibroblasts on the bottom of the basolateral compartment; Created with BioRender.com. (B) siRNA transfection in BeWo cells and lung fibroblasts using the combined model. (C) The formulations represented by their transport and lung fibroblast transfection results combined; the dashed lines represent the median of the two outputs. (D) The relationship between zeta potential and lung fibroblasts transfection in the combined model. (E) Representative image for siRNA transfection into lung fibroblasts using the combined model by formulation no 68. Please refer to Appendix 2 for the detailed description of the LNPs composition and the physicochemical characteristics of each formulation.*

All of the tested LNPs formulations included 10% DOTAP, shown to induce high transfection efficiency (Figure 11B-D) in addition to the lipid composition of LNPs formulations with high transport features. Among these tested formulations, LNPs containing D-lin MC3 showed significantly higher fetal lung fibroblast transfection compared to the ones containing DODAP (Figure 12B). This could be explained by the high correlation (R^2=0.95) that was found between zeta potential and fetal lung fibroblast transfection in the combined model (Figure 12D). Figure 12E shows transfected fetal lung fibroblasts using Formulation 68, which has achieved the synergy between high transport and transfection efficiencies (Figure 12C) and has the highest zeta potential.

3.9 Ex vivo Screening of Lipid Nanoparticle Safety on Fetal Lungs

Previous studies targeting the placenta showed no fetal exposure to the nanoparticles and no effect on fetal outcome [31,135]. However, a recent study showed that even if there was no direct fetal exposure, nanoparticles still pose a risk for fetal development as they can disrupt the placental secretome [136]. In addition, recent efforts for fetal gene therapies have recommended direct injection to the fetus through the amniotic sac or the fetal vitelline vein, which leads to NP exposure in the different fetal organs, such as the lungs or liver [12,13].

Abnormal lung development as observed in Congenital Diaphragmatic Hernia (CDH) is one of the deadliest fetal anomalies [78]. Thus, targeting the abnormal lungs with a specific genetic modality could offer cures for deadly diseases [78]. Therefore, it is essential to investigate the toxicity of different LNPs compositions on lung development to guide future studies on targeted fetal gene therapies. Hence, in this study, a fetal lung explant model was used to assess the outcomes from direct exposure to different LNPs of varying composition, as outlined in Figure 13.

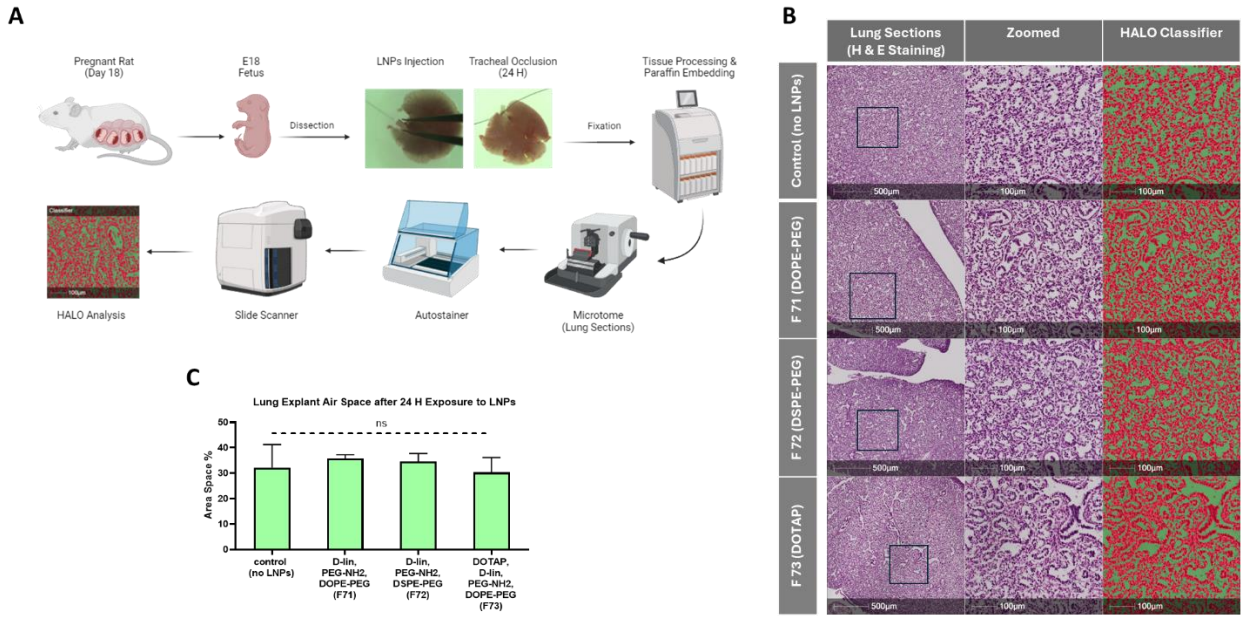

Figure 13: *Ex vivo testing of the safety of LNPs in fetal lung explants. (A) The lung explant LNPs testing workflow;Created with BioRender.com. (B) Representative images for Hematoxylin and Eosin (H&E)*

staining after 24 hours exposure to different LNPs; the black box in each image outlines the zoomed-in part. HALO classifier shows what represents the airspaces (in green) and the lung tissue (in red). (C) The lung air space after 24 hours exposure to different LNPs. Please refer to Appendix 2 for the detailed description of the LNPs composition and the physicochemical characteristics of each formulation.

Evaluating the air spaces of the lung has been used as a surrogate marker to study normal lung development and compare it to diseased states [95]. In the current study, the Autostainer, Slide Scanner, and HALO analysis have been used to automate the workflow of histological studies, as shown in Figure 13. Image analysis of H&E stained sections showed no effect on the lung airspace composition in the different LNPs groups compared to the control group, as shown in Figure 13C.

Apoptosis is considered a mark of normal lung development [95]. However, excessive exposure to nanoparticles could lead to higher apoptosis.

Since Caspase-3 and Caspase-9 are considered central regulators of apoptosis [137], their abundance were evaluated as surrogate marker of the apoptosis. Previous studies showed that cationic lipids' headgroups structure could induce cytotoxic behavior through a caspase-dependent mitochondrial intrinsic pathway [138]. Following 24 hours of exposure to different LNPs, there was no significant difference in Active Caspase-3 abundance between the different LNPs formulations and the control group, as shown in Figure 14C. The analysis was performed using the positive pixel counting and nuclear segmentation methods available in HALO software, as shown in Figures 14A and 14B.

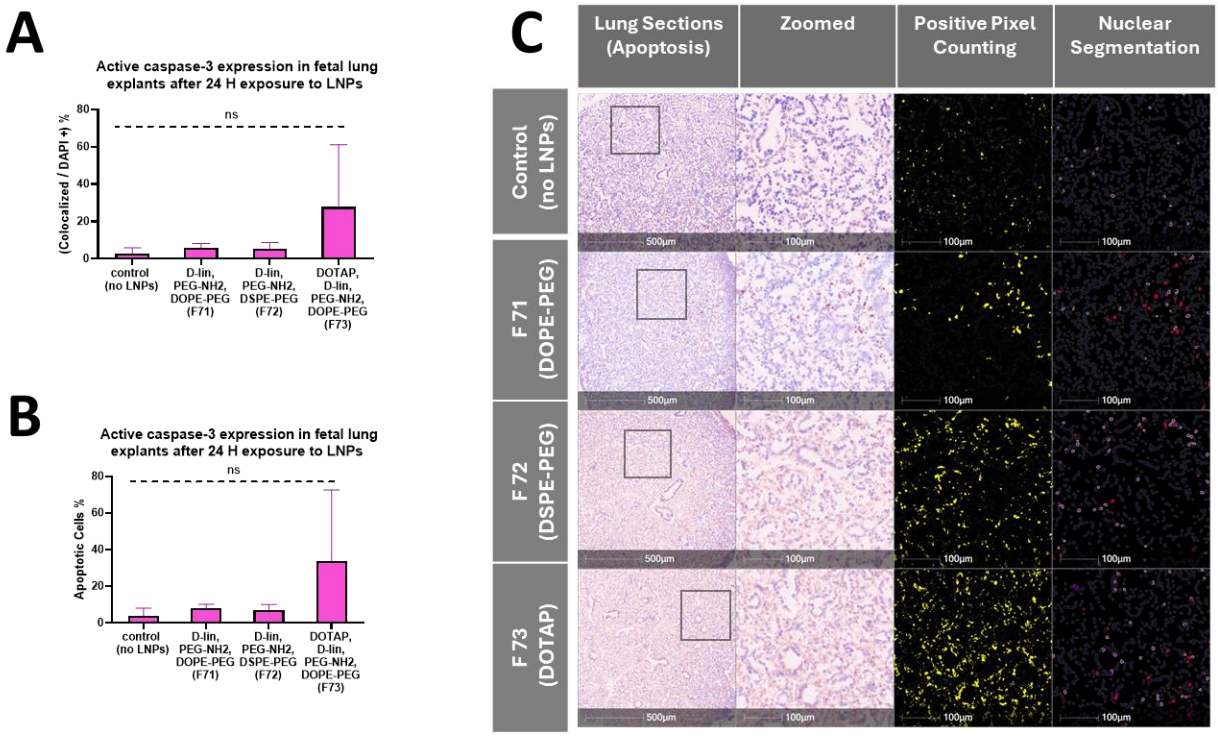

Figure 14: *Immunofluorescence staining for apoptosis in the fetal lung explant. (A) Active-caspase-3 staining signal of the different LNPs groups using the positive pixel counting analysis method, by*

dividing the colocalized signal over the DAPI+ signal. (B) Active-caspase-3 staining signal of the different LNPs groups using the nuclear segmentation method to count apoptotic cells. (C) Representative images of the active capase-3 staining; black boxes outline the zoomed-In part; Positive pixel counting images display the pixels that exceed the minimum threshold (in yellow); the nuclear segmentation images show the apoptotic cells (in purple).

In addition, fetal lung proliferation is highly active at this stage of development. Ki-67 abundance, which marks proliferative cells, was not affected by the exposure to different LNPs (Figure 15).

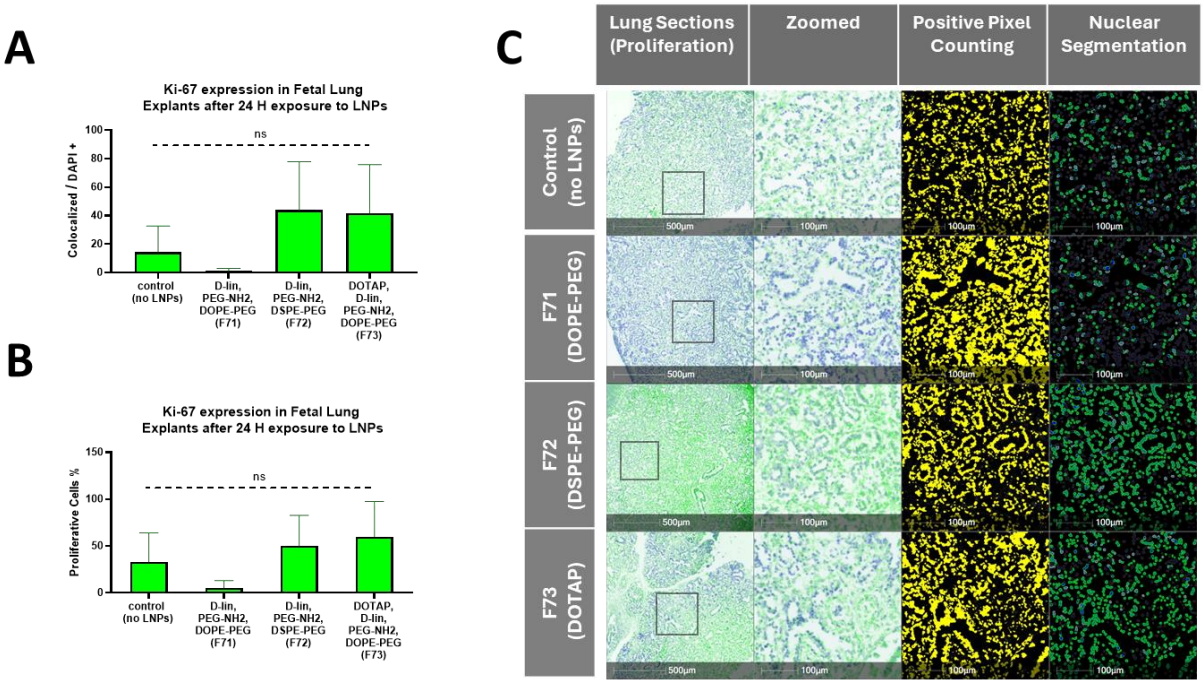

Figure 15: *Immunofluorescence staining for Proliferation in the fetal lung explant. (A) ki-67 staining signal of the different LNPs groups using the positive pixel counting analysis method, by dividing the colocalized signal over the DAPI+ signal. (B) ki-67 staining signal of the different LNPs groups using the nuclear segmentation method to count proliferative cells. (C) Representative images of the ki-67 staining; black boxes outline the zoomed-In part; Positive pixel counting images display the pixels that exceed the minimum threshold (in yellow); the nuclear segmentation images show the proliferative cells (in green). We observed non-specific interaction from the ki-67 antibody, signal outside the nucleus; this could be due to the low specificity of the antibody used. However, the analysis depended on antibody signal colocalized with the nucleus.*

These findings support the feasibility of exploring LNPs for targeted fetal gene therapies aimed at addressing lethal fetal anomalies, such as Congenital Diaphragmatic Hernia, while emphasizing the importance of continued safety assessments in future studies.

4. Conclusion

In this work, we developed a library of diverse LNPs by varying the types and ratios of the different lipid classes. Using this library, we took two approaches to study the placental transport of LNPs: statistical analysis and machine learning. Statistical analysis has identified key parameters influencing the transport, such as the antibody conjugation mechanism and the PEGylated lipid's percentage, tail saturation, and end-functional group. However, the ML model identified more properties driving the transport, such as the zeta potential, size, and concentration. Relying on the ML model results, we further optimized the LNPs formulation to include properties and compositions that induce transport. We were able to purposely design formulations that had low, medium, or high placental transport. These results are of significance for future studies aiming at developing LNPs formulation targeting maternal organs (requiring low placental transport) or fetal organs (requiring high transplacental transport).

However, a limitation of our developed ML models is their reliance on a relatively small dataset, derived from a single study, compared to larger datasets encompassing multiple studies. We are sharing our dataset (Appendix 3). So that additional data points from future studies can be incorporated, particularly considering the ongoing development of new lipids and other nanocarriers. This will accelerate the development of validated LNPs properties and transport results, thus fostering collaboration and advancing research on NP interactions with the placenta.

Combining the transport and cellular association studies has depicted the importance of the placental model structure and the dePEGylation step in influencing the uptake and transport of LNPs. Besides, the transfection studies have confirmed the importance of cationic lipids and N/P ratio in the preferential transfection of lung cells. Studying the LNPs in the combined transport and transfection model has shown that LNPs could bypass the placental barrier and transfect fetal cells, which could be a potential route to reach fetal organs. However, this could also raise concerns about environmental exposure to different NPs during pregnancy.

Finally, our *ex vivo* results suggest the safety of LNPs during fetal organ development that enable their use as a safe gene delivery vehicle during pregnancy. However, our *in vitro* viability studies raise concerns about incorporating high concentrations of permanently cationic lipids, which have been followed in different studies targeting the lung. Future studies should focus on the development of other safe ionizable lipids that can target the fetal lung and other fetal organs.

5. Acknowledgement

We want to thank Mr. Daywin Patel and Dr. Arzu Ozturk from the Children’s Hospital Research Institute of Manitoba, and Mr. Xiaofeng Lu from the core facilities at St. Michael's Hospital for their support in the animal work and histological studies.
Biorender and GraphPad Prism were used to create the figures.

A.A. was supported by Research Manitoba Master Studentship, Rady Faculty of Health Sciences Master Studentship, and Women’s Health Research Foundation of Canada Scholarship. R.K. is the inaugural Thorlakson Chair in Surgical Research for the University of Manitoba and parts of this work were supported by an operating grant from the Children’s Hospital Research Institute of Manitoba.

Chapter 3: Placental Nanoparticle Uptake-on-a-Chip: The Impact of Trophoblast Syncytialization and Shear Stress

Amr Abostait[a,b,†], Jack Tyrrell[a,†], Mahmoud Abdelkarim[a,c], Shahla Shojaei[a], Wai Hei Tse[b,f], Ibrahim M. El-Sherbiny[d], Richard Keijzer[b,f], Hagar I. Labouta[a,b,c,e*]

[a] College of Pharmacy, University of Manitoba, Winnipeg, R3E 0T5, Canada; [b] Children's Hospital Research Institute of Manitoba, Winnipeg, R3E 3P4, Canada; [c] Biomedical Engineering, University of Manitoba, Winnipeg, R3T 5V6, Canada; [d] Nanomedicine Research Labs, Center for Materials Science, Zewail City of Science and Technology, Giza, 12578, Egypt; [e] Faculty of Pharmacy, Alexandria University, Alexandria, 21521, Egypt; [f] Depts of Surgery, Division of Pediatric Surgery, Pediatrics & Child Health and Physiology & Pathophysiology, University of Manitoba, Winnipeg, R3A 1R9, Canada

[†] They contributed equally.

Keywords: Prenatal nanomedicine; placenta; syncytialization; nanoparticles; microfluidics; placenta-on-a-chip; cell uptake.

Contributions of Authors

A.A. and J.T. performed the experiments (formulation development, characterization, and in vitro work). J.T. and M.A. performed the imaging and image analysis. H.L. has led the project conception, design and funding acquisition and supervised the work. R.K., I.E., W.T. were involved in planning. A.A., H.L., J.T., M.A. processed the experimental data, performed the analysis, drafted the manuscript and designed the figures. All authors discussed the results and commented on the manuscript.

ABSTRACT

The placenta is a dynamic and complex organ that plays an essential role in the health and development of the fetus. Placental disorders can affect the health of both the mother and the fetus. There is currently an unmet clinical need to develop nanoparticle-based therapies to target and treat placental disorders. However, little is known about the interaction of nanoparticles (NPs) with the human placenta under biomimetic conditions. Specifically, the impact of shear stress exerted on the trophoblasts (placental epithelial cells) by the maternal blood flow, the gradual fusion of the trophoblasts along the gestation period (syncytialization), and the impact of microvilli formation on the cell uptake of NPs is not known. To this end, we designed dynamic placenta-on-a-chip models using BeWo cells to recapitulate the micro-physiological environment, and we induced different degrees of syncytialization via chemical induction with forskolin. We characterized the degree of syncytialization quantitatively by measuring beta human chorionic gonadotropin (β-hCG) secretion, as well as qualitatively by immunostaining the tight junction protein, ZO-1, and counter nuclear staining. We also characterized microvilli formation under static and dynamic conditions via F-actin staining. We used these models to measure the cell uptake of chondroitin sulfate A binding protein (CSA) conjugated and control liposomes using confocal microscopy, followed by image analysis. Interestingly, exposure of the cells to a dynamic flow of media intrinsically induced syncytialization and microvilli formation compared to static controls. Under dynamic conditions, BeWo cells produced more β-hCG in conditions that increased the cell exposure time to forskolin ($p < 0.005$). Our cell uptake results clearly show a combined effect of the exerted shear stress and forskolin treatment on the cell uptake of liposomes as uptake increased in forskolin exposed conditions ($p < 0.05$). Overall, the difference in the extent of cell uptake of liposomes among the different conditions clearly displays a need for the development of dynamic models of the placenta that consider the changes in the placental cell phenotype along the gestation period, including syncytialization, microvilli formation, as well as expression of different transport and uptake receptors. Knowledge generated from this work will inform future research aiming at developing drug delivery systems targeting the placenta.

1. Introduction

The placenta is a highly specialized transient biological barrier separating the maternal organs and the fetus. It plays a key role in the development of pregnancy. Placental disorders are associated with several pregnancy complications including preeclampsia and fetal growth restriction. There is therefore a substantial clinical need for the development of targeted carriers to deliver therapies to the placenta and minimize any potential side effects of the encapsulated drug that could compromise the health of the mother and the fetus.[139-141] Nanotechnology applications in medicine (called nanomedicine), have introduced the use of nanoparticles (NPs) as carriers for drug targeting, therefore avoiding off-target drug accumulation. Although this concept of nanomedicine has been applied clinically for more than two decades,[142] prenatal nanomedicine is still in its infancy.

Our current knowledge of the interaction between NPs and the human placenta under conditions simulating the physiological environment of a pregnant woman is rudimentary, especially in two aspects: the effect of the syncytialization (fusion) of the placental epithelial cells as pregnancy proceeds, and the effect of the dynamic environment due to blood circulation.

The placenta is a dynamic biological barrier which undergoes several changes in structure, as pregnancy progresses.[143] The placenta is made up of multiple layers. In the outermost layer, interacting with the maternal blood flow, is the presence of trophoblastic cells that undergo syncytialization.[144] In this process, the trophoblastic cells fuse together to form a multinucleated cellular barrier.[145] The conversion from the mononucleated cytotrophoblasts to the syncytial state results in alterations of the trophoblast phenotype over time which upregulates the production of placental hormones such as human chorionic gonadotropin (β-hCG) and is therefore integral to the hormonal function of the placenta.[146] When syncytialization is impaired, adverse reactions can occur downstream, such as premature births, developmental defects, and even preeclampsia.[144] Therefore, to understand how NPs interact with the placenta, we must first investigate how cellular uptake of NPs is affected by syncytialization, an overlooked parameter in studies focusing on *in vitro* NP placental interactions.

A major set-back in developing prenatal nanomedicine is the difficulty to mimic the dynamic physiological environment of human pregnancy. The use of *in vivo* models is associated with monetary and ethical costs. Furthermore, tests conducted on animal models have little bio-relevance to human pregnancy as there are considerable variations in the placentation, duration of pregnancy, and the physiological changes occurring during pregnancy.[141] Additionally, traditional static *in vitro* models do not consider physiological dynamism. Among current models, *ex vivo* human placental models are the closest to replicate the physiological system as they involve the usage of the actual human placenta for the studies. However, viable placental explants are scarce, complex to set-up and cannot be sustained for extended periods and are thus not suitable for long-term exposure studies.[147]

Organ-on-a-chip technologies mitigate the demerits of current *in vitro*, *in vivo* and *ex vivo* models and improve upon their benefits while utilizing minimal resources.[148] This technology is based on the principle of microfluidics which is the manipulation of fluids in small volumes like droplets and channels with at least one dimension in the microscale.[149] Most fluids behave differently in the microscale, where the capillary forces and viscous forces dominate.[150] This is similar to the dynamic micro-cellular systems within our body. Connecting the organ-on-a-chip to a flow of biological fluids

has shown to be effective in replicating the physiological system.[149-152] Placenta-on-a-chip technology therefore offers a powerful replicable tool to recapitulate the microstructure of human placenta and the dynamic environment. Its use for NP screening is in the nascent stages;[75] and was not used for the evaluation of liposomes, one of the most successful clinically approved nanocarriers.[142,153-155]

The objective of this study is to use this placenta-on-a-chip technology to develop a mechanistic understanding of the interaction of targeted PEGylated liposomal nanocarriers that are surface functionalized with placental CSA binding peptide (CSA, EDVKDINFDTKEKFLAGCLIVSFHEGKC) with the placental trophoblasts (BeWo b30) under dynamic conditions and following the chemical induction of syncytialization versus control experiments. Syncytialization of BeWo cells is commonly induced using forskolin which activates the protein kinase A pathway within the trophoblast cells, initiating syncytialization.[156]

2. Materials and Methods

2.1. Materials

Human placental BeWo b30 cells were kindly provided by Dr. Tina Bürki (EMPA, Switzerland) with permission of Prof. A. Schwartz. (Washington University in St. Louis, USA). Microfluidic chips, iBidi µ-Slide I $^{0.2}$, were purchased from iBidi™ (USA). All lipids, including, 1,2-dioleoyl-sn-glycero-3-phosphocholine (DOPC), cholesterol, 1,2-disearoyl-sn-glycero-3- phosphoethanolamine-N-[carboxy(polyethyleneglycol)-2000] (DSPE-PEG(2000)-COOH) and 1,2-dioleoyl-sn-glycero-3-phosphoethanolamine-N-(lissamine rhodamine B sulfonyl) (Rhodamine labelled PE) were purchased from Avanti Polar Lipids (Birmingham, USA). Placental CSA binding peptide (CSA, EDVKDINFDTKEKFLAGCLIVSFHEGKC), bicinchoninic acid (BCA) assay and human hCG-beta ELISA kit, 3000 MWCO Amicon Ultra-15 Centrifugal filters, DPBS, Triton X-100, Tween 20, goat serum, glycine, BSA, ZO-1 monoclonal antibody, goat anti-rabbit Alexa Fluor 488, Alexa Fluor 488-conjugated phalloidin, DAPI, Fluoromount-G reagent, paraformaldehyde (made from 16% Methanol free Formaldehyde with 1x PBS), Ham's F-12K culture medium and supplements, 100 nm polystyrene particles as well as micro cover slips, culture plates and MWCO 3000 Ultra-15 Centrifugal filters were all purchased from Thermofisher (Massachusetts, USA). ViaLight™ Plus Cell Proliferation and Cytotoxicity BioAssay Kit was purchased from Lonza (Switzerland). EDC (N-(3-dimethylaminopropyl)-N´-ethylcarbodiimide hydrochloride and NHS (N-hydroxysuccinimide) were purchased from Alfa Aesar (Tewksbury, USA). 300,000 MWCO Centrisart tubes were purchased from Sartorius (Goettingen, Germany). Gelatin and forskolin were purchased from Sigma-Aldrich (Oakville, Canada). Dulbecco's phosphate-buffered saline (DPBS) was purchased from Corning (New York, USA). Vectashield mounting medium was purchased from Vector Laboratories (Burlingame, USA). All other reagents, solvents, and buffers were purchased from Fisher Scientific (Canada) and were used directly with analytical grade. Ultrapure water for the cell experiment was obtained from a Millipore Milli-Q purification system.

2.2. Synthesis and characterization of CSA-conjugated liposomes

2.2.1. Microfluidic synthesis of rhodamine labelled PEGylated DOPC liposomes

Liposomes were synthesized using the Dolomite 5-Input Chip (Dolomite Microfluidics, Norwell, USA), connected to two programmable syringe pumps (KD Scientific, USA). To prepare the lipid solution, DOPC, cholesterol, DSPE-PEG(2000)-COOH, and rhodamine-labelled PE were solubilized in ethanol at a molar ratio of 57.5:37:5:0.5, respectively for a total concentration of 8.14 mg/mL. PBS, 0.1 M, was injected into two side channels intersecting with a center channel to which the lipid solution was injected. The flow rate ratio (FRR), defined as the ratio of volumetric flow rate of aqueous phase to that of lipid phase, was 12:1 and the total flow rate (TFR) was 50 uL/min. Those parameters were decided on after trying different FRR and TFR to give the desired range and distribution of size, these values are reported in Appendix 4. The liposome dispersion was centrifuged using 3000 MWCO Centrisart centrifugal tubes at 3700 rpm for 20 min at 4 °C, then diluted in PBS buffer to the original volume. This was repeated 3 times to remove remaining ethanol content.

2.2.2. Surface functionalization of liposomes with placental CSA binding peptide

Liposomes were surface functionalized with CSA using EDC/NHS chemistry following previously reported protocols.[108,140] First, the carboxylic groups on the liposomes were activated by the crosslinking agent (EDC/NHS) in PBS buffer. Briefly, a volume of 0.6 mL liposomes was incubated with 0.3 mg of EDC and 0.45 mg of NHS with gentle shaking for 6 hours at room temperature in the dark, as shown in Figure C. Liposomes were then centrifuged using 3000 MWCO Centrisart centrifugal tubes at 3700 rpm for 30 minutes at 4 °C to remove excess reagent followed by three successive washing steps. The total volume was then completed to 0.6 mL with PBS. Finally, CSA peptide was added at a 1: 1 molar ratio to the carboxylic acid groups present on the surface of the liposome and the coating process was continued overnight at room temperature in the dark with gentle shaking. This was followed by centrifugation and further washing steps with a 300,000 MWCO Centrisart centrifugal filter to remove unbound peptide.

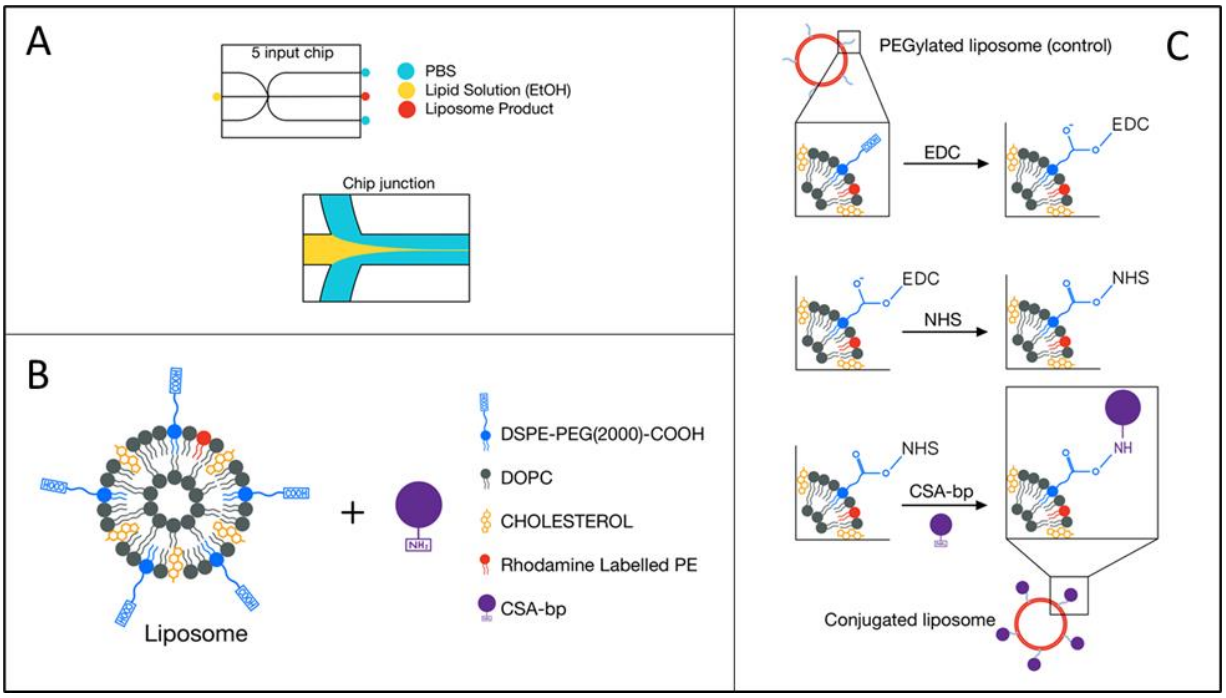

Figure 16: *The detailed synthesis process for liposomes using the microfluidic technique. A Dolomite 5 input chip used for liposome synthesis. Liposomes were synthesized using the Dolomite 5 input chip. DOPC, cholesterol, DSPE-PEG(2000)-COOH, and rhodamine-labelled PE were solubilized in ethanol and introduced to the center channel of the 5-input chip while PBS (0.01 M) was injected into the two side channels. These solutions then intersect at the chip junction, creating a laminar stream. As the ethanol moves through the outlet tube, the stream grows thin until the lipid solution is supersaturated, and liposomes form due to hydrophobic interactions when exposed to the PBS solution. The width of the laminar stream, rate of synthesis, and liposome characteristics are determined by the FRR, and TFR. B Liposome structure formed from a lipid solution of DOPC, cholesterol, DSPE-PEG(2000)-COOH, and rhodamine-labelled PE. C Surface functionalization of control liposomes using EDC/NHS chemistry for amide conjugation to CSA-bp. Briefly, the carboxylic acid groups of the PEGylated lipid DSPE-PEG(2000)-COOH were activated by EDC and NHS in PBS buffer through gentle shaking. Then, EDC and NHS were removed through centrifugal filtration before the CSA binding peptide was added. The conjugation process was then allowed to continue overnight under constant shaking, after which unbound peptide was removed through centrifugal filtration.*

2.2.3. Characterization of liposomes

Liposomes were characterized for mean diameter, polydispersity index (PDI) and zeta potential using a ZetaPALS machine (Brookhaven Instruments, Holtsville, USA) before and after covalent peptide attachment. Measurements were performed in triplicates.

The size distribution of liposomes was also determined with a complementary technique, ZetaView® Nanoparticle Tracking Analysis (NTA, Particle Metrix GmbH, Germany) using an embedded laser of 40 mW at 520 nm and a CMOS camera. This technique was also used to determine the concentration of liposomes (number of particles per mL). First, standard polystyrene particles with a known average

size of 100 nm were used to calibrate the instrument prior to sample readings. Automated quality control measurements including, but not limited to, cell quality check, instrument alignment, and focus were also performed prior to the use of the ZetaView for sample measurements. Samples were diluted in PBS to a final volume of 1 mL and were injected in the measurement cell. Liposomal dilutions for accurate measurements were found by pre-testing the ideal particle per frame value (150–200 particles/frame). For each measurement, three cycles were performed, scanning 11 positions each, and capturing 30 frames per position. For each measurement, the instrument pre-acquisition parameters were set to a sensitivity of 85, a shutter of 50, and a temperature of 22°C. The captured videos were analyzed by the ZetaView Software with specific analysis parameters: Maximum area: 1000, Minimum area: 10, Minimum brightness: 20, Trace length: 10, Framerate: 30. The number of completed tracks in NTA measurements was always greater than the proposed minimum of 1000 in order to minimize data skewing based on single large particles.[157] After the automated analysis of all 11 positions and the removal of any outlier positions, the mean, median, and mode (indicated as diameter) sizes, as well as the PDI, and the number concentration were calculated by the optimized machine software.

Conjugation of CSA to the surface of the liposomes was quantified using a BCA assay kit, in accordance with the manufacturer's instructions. This assay is suitable to measure peptides covalently bound to liposome surfaces.[108] Briefly, a calibration curve was constructed using a series of known concentrations of the CSA binding peptide within a concentration range of 33 – 800 µg/mL (Appendix 4). Samples were measured against blank solutions containing unconjugated liposomes to remove lipid interference.

2.3. Cell culture

BeWo b30 cells were cultured in Ham's F-12K medium supplemented with 10% fetal calf serum, 1% L-Glutamine and 1% penicillin–streptomycin–neomycin and were incubated in a humidified atmosphere with 5% CO_2 at 37 °C. On confluency, cells were sub-cultured through the addition of a 0.5% trypsin-EDTA treatment (approx. 0.2-0.5 million cells per T-75 flask).

2.4. Static cell experiments

Cells were cultured on gelatin pre-treated glass micro coverslips on the bottom of 24-well culture plates at a density of ~ $5x10^6$ cells/mL. Once the cells reached 90% confluency, cells were treated with 50 uM forskolin for up to 72 hours. Cells not exposed to forskolin were used as controls. Media was replaced every day; harvested medium at 24, 48, and 72 hours was stored at -80 °C for further analysis of β-hCG concentration over time to determine the rate of syncytialization. At the end of the experiment, cells were fixed with 4% paraformaldehyde (PFA), rinsed with 1x DPBS three times, then stored submerged in DPBS until further immunostaining.

2.5. Dynamic Placenta-on-a-chip model

Cells were cultured at a density of $5x10^6$ cells/mL in a gelatin-treated microfluidic channel, iBidi µ-Slide I $^{0.4}$ (iBidi™, Germany); with a channel height of 450 µm, a channel length of 50 mm, a width of 5 mm, and growth area of 2.5 cm^2. On confluency, the chips were connected to a closed loop of re-circulating medium at a flow rate of 22.89 uL/min to achieve a shear stress value of 0.025 dyne/cm^2 within the chip. This value of shear stress was chosen based on previous reporting, stating that the estimated average value for shear stress in the intervillous space can be between 0.001-0.1 dyne/cm^2.[158,159] As shown in Figure , the organ-on-a-chip chamber is open at both ends with an inlet and outlet that can be connected to a dynamic media circulating system. The chip's gelatin treated chamber enables the cells to adhere to the floor of the chamber, which allows the media to move over the cells. This dynamic flow of media mimics similar shear stress environments that the cells experience *in vivo*, allowing for a more accurate look into the physiological characteristics of the cells than static models.

Fluid flow was managed with a piezoelectric pressure controller (model OB1 Mk3, Elveflow). The equipment was tethered to a dedicated software (ESI, Microfluidic Software and SDK, Elveflow) and coupled to a flow sensor that allows for control over the flow rates applied, up to a maximum of 80 µL/min (Figure). The flow of media within the chip and tubing system is controlled via the ESI software. Cells were either exposed to forskolin under dynamic conditions at a concentration of 50 uM or used as controls (only exposed to culture media). At 24, 48, and 72 hours, media was harvested and was replaced with a fresh media. Harvested media was stored at -80 °C for further analysis of β-hCG concentration. At the end of the experiments, cells were fixed with 4% PFA and rinsed with 1x DPBS followed by immunostaining.

Additional experiments were performed to observe the presence of microvilli on the cells surface. In these experiments, a similar dynamic set up running at 0.014 dyne/cm^2 was used to compare the presence of microvilli formation on the cell surface in dynamic versus static conditions.

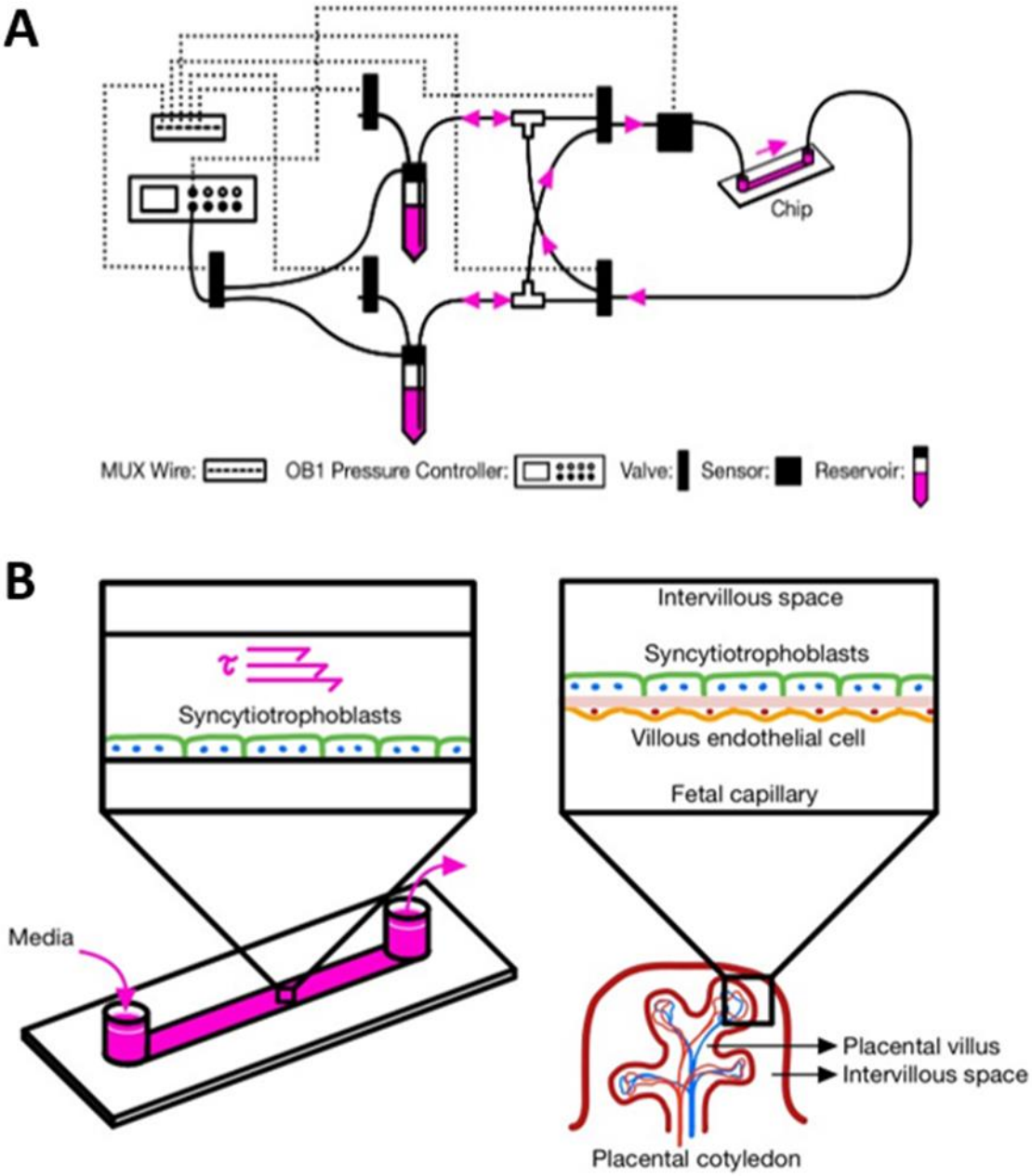

Figure 17: *A Flow circuit used in the dynamic placenta-on-a-chip experiments. Fluid flows from the media reservoir to the collection reservoir through the induction of air pressure controlled by an air pump connected to the OB1 pressure controller (Elveflow). The fluid flows through a series of valves that can be switched on or off through the MUX wire system to adjust the flow circuit and allow for recirculation. The sequential opening and closing of these valves, as encoded by the software settings, is important to always maintain unidirectional through the chip. The flow sensor reacts to the movement of cell culture media through the system and relays a signal to the OB1 pressure controller to adjust the flow to maintain a stable flow rate of media. B Placenta-on-a-chip*

architecture compared to placental anatomy within the placental cotyledon showing the similarity in maternal syncytiotrophoblast cell layers.

2.6. Quantitation of β-HCG secretion by the placental cells

Harvested media samples collected from the static and dynamic experiments were allowed to thaw and were tested to measure the concentration of β-hCG using a human hCG-beta ELISA kit (Thermofisher). Due to the large volumetric difference between the static and dynamic samples, each sample was regulated to a final volume of 1 mL which was used in the final human hCG-beta ELISA kit. Static samples were diluted to 1 mL using fresh media, while dynamic samples were concentrated to 1 mL using Amicon Ultra-15 Centrifugal filters, MWCO 3000.

Samples were analyzed in accordance with the manufacturer's instructions. Briefly, the samples were added to a human hCG-beta antibody coated well and allowed to incubate for 2.5 hours at room temperature. The wells were then washed with the wash buffer and a human hCG-beta biotin conjugate was introduced for 1 hour. After further washing, streptavidin-HRP was added for 45 minutes, washed, and a TMB substrate (3,3',5,5'-Tetramethylbenzidine) was added and was allowed to incubate for 30 minutes in the dark before adding the stop solution. A plate reader was then used to measure fluorescence at a wavelength of 450 nm. Then, by comparing the relative absorbance values to a standard concentration curve using diluted standard solutions provided by the manufacturer, the concentration of β-hCG in each sample was determined with an average recovery range of 94%.

2.7. Characterization of trophoblast syncytialization and microvilli formation via immunofluorescence

To characterize trophoblast syncytialization, fixed and washed cells were incubated with a blocking buffer (1X PBS/5% Bovine serum albumin (BSA)/0.3% Triton™ X-100) for 60 minutes. We used immunostaining to detect the expression and localization of the cytoplasmic scaffolding protein ZO-1.[160] Briefly, the cell monolayer was exposed to a secondary blocking solution containing 3% BSA, 3% goat serum, and 7.51 mg/mL glycine (0.1 M) in PBST (PBS with 0.1% Tween 20) for 1 hour. We then added ZO-1 monoclonal antibody for 1 hour at a 1/100 dilution, followed by washing three times by PBST. The cells were then exposed to goat anti-rabbit Alexa Fluor 488 at a concentration of 5 µg/mL in 1% BSA for 1 hour at room temperature. The cells were rinsed again in PBST before the addition of DAPI (1/1000) for 3 minutes, followed by washing. Finally, cells were mounted using Fluoromount-G mounting liquid and Vectashield for static and dynamic experiments, respectively. Samples were stored at 4 °C until further visualization by confocal microscopy.

Additional experiments were conducted to stain for actin using Alexa Fluor-488-conjugated phalloidin to observe the presence of microvilli on the cell surface. A similar protocol was used as above. Briefly, the specimen was blocked with blocking buffer for 1 h before introducing the fluorochrome conjugated primary antibody. The cells were then allowed to incubate for 1 h before counter staining the cell nucleus with DAPI.

2.8. Cell viability assay

Cell viability was measured using a ViaLight™ Plus Cell Proliferation and Cytotoxicity BioAssay Kit (Lonza, Switzerland). Briefly, BeWo cells were seeded into a 96 well plate at a density of 50,000 cells per well. On confluency, cells were exposed to either of unconjugated control liposomes or CSA-conjugated liposomes at a series of concentrations of $5x10^6$ –$5x10^8$ particle/mL, equivalent to 10 – 1000 liposomes/cell, for 24 hours. Negative control conditions (100 % cell viability) were allowed to incubate with only cell media, free of any liposomes. Positive controls (0 % cell viability) were exposed to triton X-100 for 30 minutes. Following exposure time, cells were introduced to a cell lysis reagent for 10 minutes before the supernatant was removed and added to a black, glass bottom 96 well plate used for reading bioluminescence in the plate reader. Then, all samples were introduced to an ATP monitoring reagent for 2 minutes. Bioluminescence was then measured using a BioTek Synergy H1 Plate Reader (Agilent Technologies, Canada). Percentage cell viability was calculated based on five replicates as follows:

$$\%\ Cell\ viability = \frac{F_{exp} - F_{positive\ control}}{F_{negative\ control} - F_{positive\ control}} * 100 \quad \text{Equation 1}$$

2.9. Liposomal cell uptake study

Cells cultured in static and dynamic set-ups and at different experimental conditions were exposed to control and CSA-conjugated liposomes at a concentration of $1.25x10^9$ particles/mL at 37°C, 5% CO_2 for 8 h. For the static experiments, we exposed the cell models to liposomes following exposure to forskolin for 48 and 72 h versus appropriate control cell models not exposed to forskolin. We then compared the results from the 48 h static conditions (forskolin treated and control static models) to 48 h dynamic experiments (forskolin treated and control dynamic models).

Following incubation, cells were washed three times with 1x DPBS to remove any unbound NPs and were fixed with 4% PFA. Cells were stained with ZO-1 and DAPI to allow for visualization of the tight junctions and cell nuclei, respectively. Imaging slides or chips were protected from light and stored at 4 °C until imaging by confocal imaging.

2.10. Confocal laser scanning microscopy

2.10.1. Microscopy

Confocal laser scanning microscopy was performed using Zeiss LSM700 Spectral Confocal Microscope. Images were recorded with a 40x or 63x water immersion objective using the manufacturer's ZEN black imaging software. Wavelengths of 488 nm, 408 nm and 555 nm were used for excitation of ZO-1 and actin, DAPI-labelled nuclei, and rhodamine-labeled liposomes, respectively. Z-stacks were captured at 1 µm steps. A minimum of three images were taken from various positions within each chamber or chip in each condition to ensure the images were representative of the entirety of the sample.

2.10.2. Image analysis

Orthogonal views were used to define the liposome signals present within the cells. Additionally, 3D models were generated from z-stack images for confirmation as shown in Figure . Z-stack layers were then analyzed using the freeware ImageJ/Fiji (National Institutes of Health) to quantify mean fluorescence intensity due to NP signals within a defined region of interest (ROI) bound by the ZO-1 stain. Briefly, Z-stack images (using the 40x objective) were overlaid with summed intensities of the signal pixels. ROI was defined in the ZO-1 channel to select the regions inside the cells, this was then overlaid onto the rhodamine labelled liposome channel image to quantify the mean fluorescence intensity within the defined ROI. For all intensity measurements, image brightness and contrast were not changed.

3. Results

3.1. Physicochemical Characteristics of liposomes

Liposomes were used as model particles to study the effect of syncytialization and the dynamic environment on cell uptake of NPs. Reproducible monodispersed rhodamine-labelled PEGylated phospholipid liposomes were prepared through microfluidic techniques using a Dolomite 5-input chip. Prepared liposomes had a hydrodynamic diameter of ~50 nm, a PDI less than 0.2 (Table 1), and were found stable in terms of colloidal properties for at least 7 days before a 10% change in diameter or PDI was observed. Liposomes were successfully functionalized with CSA without any observed aggregation. As expected, the average hydrodynamic diameter of liposomes increased to 93.7 nm following peptide conjugation. These sizes were confirmed using a nanoparticle tracking analyzer; the hydrodynamic diameters were about 49 nm and 94 nm for control and CSA-conjugated liposomes, respectively. The observed increase in the hydrodynamic diameter of the liposomes post-conjugation may be due to several factors. Throughout the process of conjugation, the liposomes undergo centrifugal filtration to remove any waste or unbound peptide. It is estimated that in this filtration, debris may be cleared of the solution - such as unbound peptide, free floating lipids, or other particulate - resulting in an increase to the average size of particles in the solution. Furthermore, the conjugation process alone will inevitably increase the size of the liposomes as we are adding CSA-bp to the PEGylated tale of the lipid DSPE-PEG(2000)-COOH. The zeta potential also decreased from -11.48 ± 4.36 mV, for control non-conjugated liposomes, to -25.5 ± 2.81 mV for CSA-conjugated liposomes. This change in zeta potential with peptide coating indicates higher stability due to steric hindrance by the peptide coat.[108] The concentrations of the prepared liposomes were ($1.7x10^{12}$ ± $1.8x10^{11}$) and ($1.2x10^{12}$ ± $8.5x10^{10}$) particles/mL for control and CSA-conjugated liposomes, respectively, as determined by nanoparticle tracking analysis. Finally, the CSA conjugation efficiency was quantified as 13% using a BCA assay compared to a preconstructed CSA calibration curve in the presence of control liposomes to correct for lipid interference. Conjugation was further verified using FTIR. The FITR spectrum showed a peak shift from 3310 to 3324 nm^{-1}. This indicates a decrease in the carboxylic acid groups and an increase in secondary amide groups. This confirms the conjugation reaction where an amine group of the CSA peptide reacted with a carboxylic acid group on the liposomal surface to give a secondary amide group.

Table 1: *Size (hydrodynamic diameter) and size distribution (PDI) of prepared liposomes. Values are presented as mean(n=10) ± standard error, in addition to statistical comparison of results*.*

Condition	**Hydrodynamic diameter, nm**	**PDI**
Control liposomes in PBS after synthesis	48.8 ± 0.5	0.19 ± 0.01
Control liposomes in PBS after filtration to remove Ethanol	49.3 ± 0.3	0.19 ± 0.01
Activated liposomes after removal of excess crosslinking reagents	57.4 ± 0.3	0.17 ± 0.01
CSA-conjugated liposomes after removal of unbound peptide	93.7 ± 1.2	0.25 ± 0.01

**Using the IBM SPSS program, a one-way ANOVA was conducted to compare how the size and PDI of NPs changed during the different steps of synthesis and conjugation. Normality checks and Levene's test were carried out and the assumptions were met. There was a highly significant difference in the size [F(3,36) = 768.7, p < 0.001] amongst the different steps, and a significant difference in the PDI [F(3,36)=10.236, p<0.001]. Post hoc comparisons using the Tukey's test was also carried out. The filtration step to remove ethanol did not change the size (P>0.05) or PDI (P>0.05). Activation by EDC/NHS increased the size by a mean difference of 8.93 ±1.09 and with a significance level (p<0.001), however, the PDI did not change significantly (p>0.05). CSA conjugation and final filtration step increased the size by a mean difference of 36.24nm ±1.09 (p<0.001) and PDI by 0.076 ±-0.014 (p<0.001) compared to activated liposomes.*

3.2. Induction of trophoblast syncytialization

We measured the extent of syncytialization, as indicated by β-hCG production under static conditions following induction by forskolin.[161] These results were then compared to syncytialization and β-hCG production under dynamic conditions to determine if the presence of shear stress affects the rate or process of syncytialization. As shown in Figure A, no significant changes ($p > 0.05$) in β-hCG production were observed under static conditions after exposure to forskolin for 24, 48, and 72 h relative to control cells not exposed to forskolin (only culture media).

Interestingly, trophoblasts exposed to dynamic conditions underwent a higher extent of syncytialization and secreted significantly ($p < 0.0001$) higher β-hCG concentration, compared to their static counterparts (Figure A). Contrary to the static experiments, the extent of β-hCG and syncytialization increased gradually over time under dynamic conditions. In conditions with a 24 h cell incubation time with forskolin under dynamic conditions, no significant difference ($p > 0.05$) was observed in β-hCG secretion as compared to dynamic control. However, at longer exposure times (48 and 72 h), forskolin treatment resulted in a significantly higher production of β-hCG relative to dynamic controls. For instance, increasing the cell exposure time to forskolin from 24 to 72 h resulted in a more than two times increase in β-hCG secretion. Comparing the different dynamic conditions, the effect of chemical induction by forskolin versus control cells was found to be highly significant ($p < 0.0005$) while the effect of cell exposure time to forskolin was found to be significant ($p < 0.005$).

Tight junctions consist of transmembrane proteins such as the cytoplasmic scaffolding protein ZO-1 (zonula occluden-1) that regulate the cell-cell adhesion and contribute to the epithelial barrier function.[160] Trophoblast cell fusion was shown to be associated with lower ZO-1 expression.[162] Therefore, we used immunostaining followed by confocal imaging to detect the expression of ZO-1 and to confirm syncytialization qualitatively. Representative images in Figure B show the lower intensity of Alexa Fluor 488 tagged ZO-1 following syncytialization. The fusion of mononucleated trophoblasts into multinucleated cells was also evident from our confocal experiments following DAPI staining of the nuclei (Figure B). We additionally compared trophoblast microvilli under dynamic and static conditions by staining the actin cytoskeleton (Figure C). Dense fine hair-like microvillous projections were observed to cover the whole surface of the BeWo cells under dynamic condition but were less expressed under static conditions and were limited to the cell boundaries.

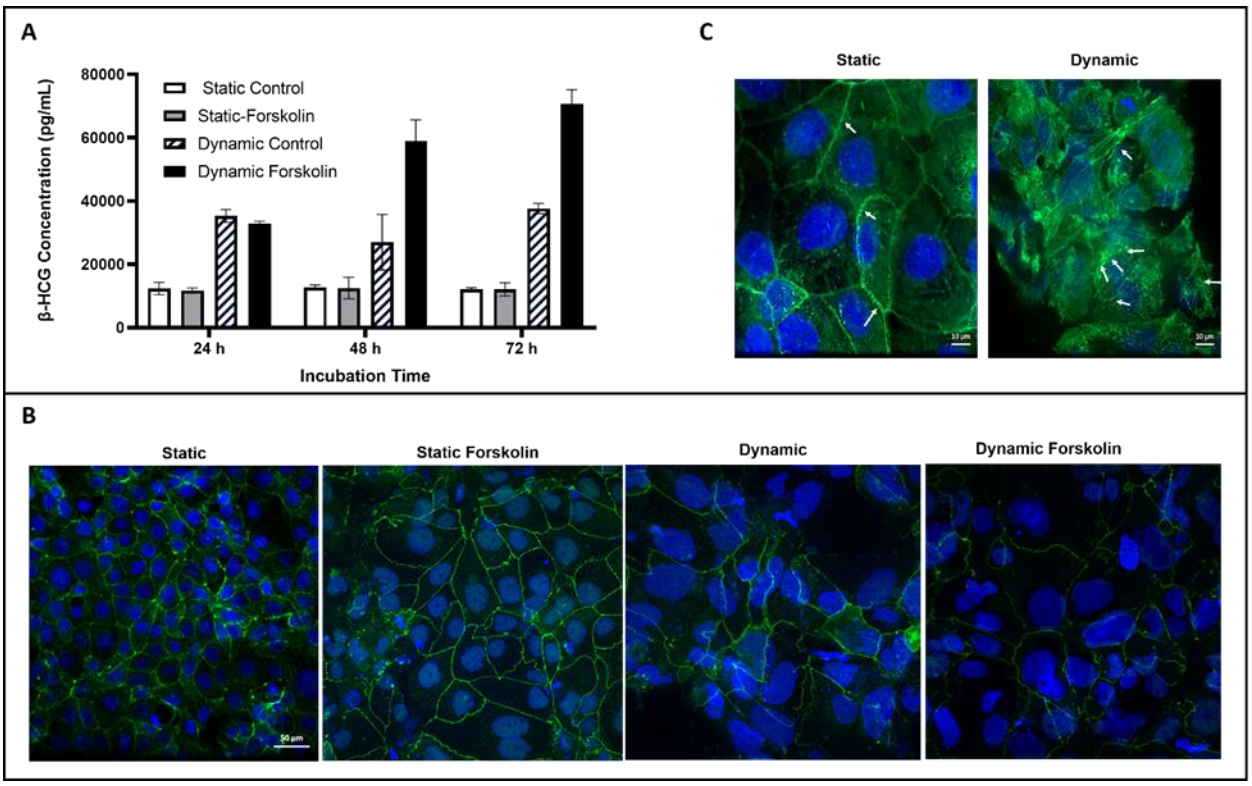

Figure 18: *Studying the extent of syncytialization under different conditions. A Beta-HCG production over time with and without chemical induction by forskolin under static and dynamic conditions. Data is represented as mean ± standard deviation (n = 3). B BeWo cells cultured under different static and dynamic conditions; DAPI-stained nuclei and Alexa Fluor 488-labelled ZO-1 are denoted in blue and green, respectively. The process and advancement of syncytialization under various conditions led to decreased expression of the tight junction ZO-1 and the higher occurrence of multinucleated versus mononucleated cells. C Microvilli formation under static and dynamic conditions as shown by actin staining of the cytoskeleton denoted in green. Microvilli are more expressed (high intensity of the Alexa Fluor-labelled actin) along the whole cell surface under dynamic conditions versus limited expression at the cell boundaries when cultured under static conditions.*

3.3. Cell viability study

Prior to tracking liposome uptake into placental cells at different biomimetic conditions, it was important to determine the concentration range for both types of liposomes, control and CSA-conjugated, that is safe to use without imposing toxicity on the cultured cells. Furthermore, as the CSA-conjugated liposomes are intentionally engineered to target the placental cells, it was important to ensure that this functionalization is not causing any cytotoxic effect. Figure A shows the viability of BeWo b30 cells after incubation with unconjugated as well as CSA-conjugated liposomes at a series of concentrations within a range of $5x10^6$ to $5x10^8$ particles/mL, as determined by nanoparticle tracking analysis. These concentrations were equivalent to liposome: cell ratios ranging from 10 to 1000 particles/cell. No significant difference ($p > 0.05$) in cell viability was observed for unconjugated liposomes or CSA-conjugated liposomes compared to non-treated control cells, indicating the safety of CSA-conjugated liposomes on the placental cells.

3.4. Cell uptake study

After careful characterization of the NPs and the cell models, and confirmation of the biocompatibility of liposomes, we wanted to respond to the main goal of the paper which was investigating how the dynamic condition and the different degrees of trophoblast syncytialization could affect cell uptake of control and CSA-conjugated liposomes. Cell uptake of fluorescent NPs was investigated using confocal microscopy followed by image analysis. Representative images can be found in Figure B. The z-stacks were analyzed for the intensity of signals due to NPs within the region of interest (inside the cells guided by the ZO-1 staining).

First, we investigated the uptake of control and CSA-conjugated liposomes into BeWo cells following NP exposure for 8 h under static conditions. Prior to NP exposure, cells were treated with forskolin for 48 h (termed the 48 h condition) or 72 h (termed the 72 h condition). Control cell models not treated with forskolin were used for comparison. On analysing the confocal images, we observed an increase in cell uptake of both control and CSA-conjugated NPs at different extents following cell exposure to forskolin, as compared to controls of the same condition (Figure D). The increase in cell uptake of CSA-conjugated liposomes following forskolin exposure versus control was statistically significant ($p < 0.05$) for the 48 h condition. In the 72 h condition, a significant increase in cell uptake of control liposomes following exposure to forskolin was observed. When comparing across the different conditions, CSA-conjugated liposomes were taken up by the cells to a higher extent when compared to control liposomes in all conditions except for the 72 h forskolin condition. However, for the latter condition, the difference in cell uptake was not statistically significant.

We then explored the impact of the dynamic condition on the cell uptake of NPs following forskolin treatment for 48 h versus static and non-forskolin treated control cell models. For all experimental conditions, exposing the cells to a dynamic flow of NPs resulted in higher cell uptake according to the results found through image analysis (Figure E). Furthermore, CSA-conjugated liposomes displayed higher values of uptake compared to control liposomes in the dynamic conditions without forskolin induction. Interestingly, forskolin exposure resulted in higher cell uptake of control and CSA-conjugated liposomes as compared to the static conditions. However, under dynamic conditions, no significant differences were observed between cell uptake of control and CSA-conjugated liposomes following chemical induction of syncytialization by forskolin. We then investigated the correlation between syncytialization, denoted by measured β-HCG concentration,

and cell uptake of liposomes from image analysis results. Though the correlation is not linear, we could observe a general increase in the cellular uptake of NPs with syncytialization (Figure F).

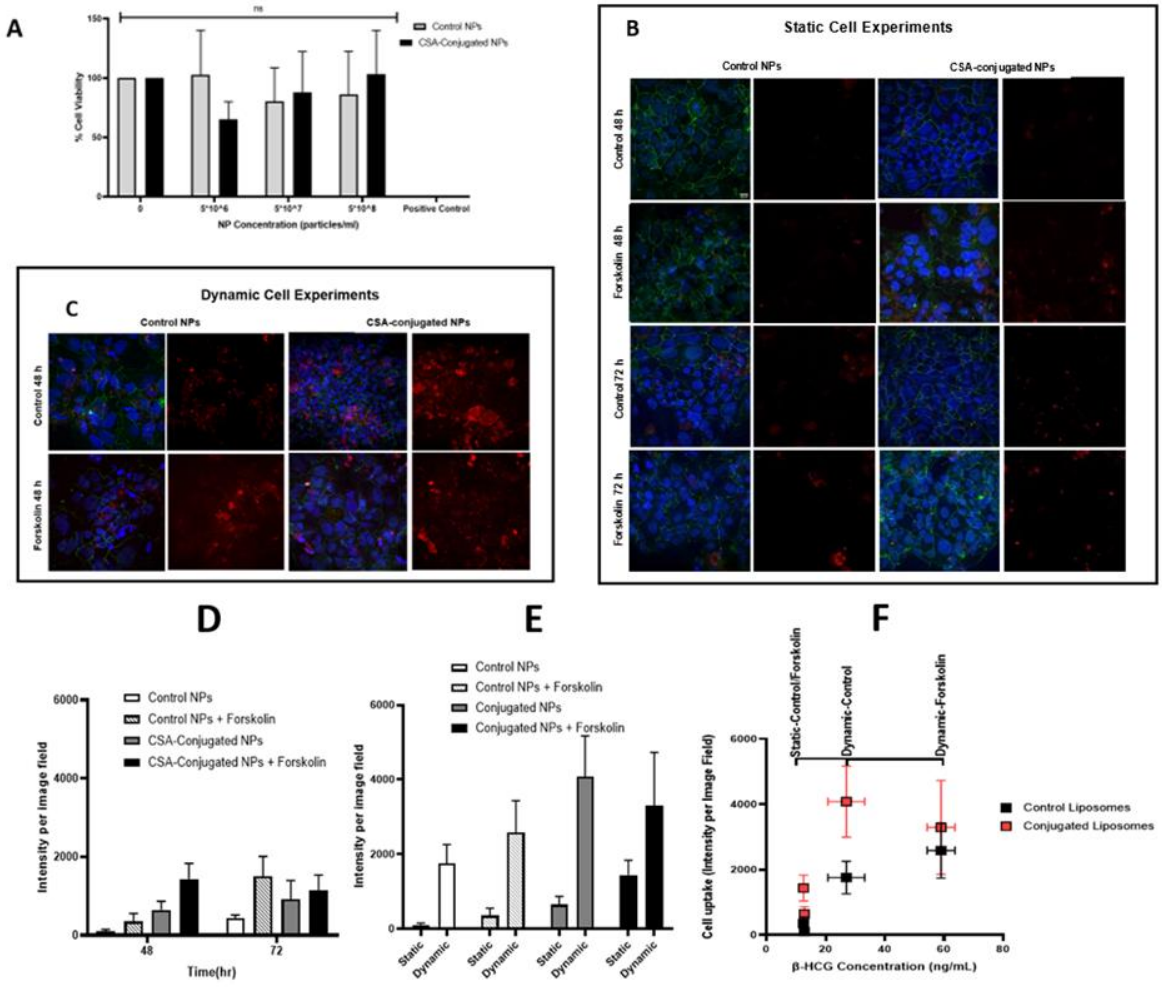

Figure 19: *The cell viability and uptake studies after introduction of liposomes under different conditions. A. Viability of BeWo b30 cells following cell exposure to control (unconjugated) and CSA-conjugated liposomes at different exposure concentrations for 24h, as determined using a ViaLight™ Plus Cell Proliferation and Cytotoxicity BioAssay Kit (Lonza, Switzerland). Triton X-100 was used as positive control. Data is presented as mean ± SD calculated from nine experimental replicates (n = 9); ns denotes non-significant difference. B. Representative images of cell uptake of control and CSA-Conjugated nanoparticles (rhodamine-labelled, denoted in red) following 8 h exposure under static conditions; Alexa Fluor-labelled ZO-1 and DAPI-stained nuclei are denoted in the figures in green and blue, respectively (n ≥ 6). Prior to cell uptake experiments, cells are either treated with forskolin for 48 or 72 h or used as controls (not exposed to forskolin). Both the overlaid image and image from the nanoparticle channel are presented for each image. C. Cell uptake of both liposomes (red) after 8 h exposure under dynamic conditions Alexa Fluor-labelled ZO-1 and DAPI-stained nuclei are denoted*

in the figures in green and blue, respectively (n ≥ 6). Cells are similarly treated with forskolin for 48 h or not treated prior to the uptake experiments. The results of image analysis of confocal images under static and dynamic conditions are presented in (D) and (E). Finally, the correlation between the extent of syncytialization, indicated by the mean concentration of secreted β-HCG, and cell uptake of both liposomes, indicated by the intensity of red signals within the ROI per image field of a Z-stack was graphed (F).

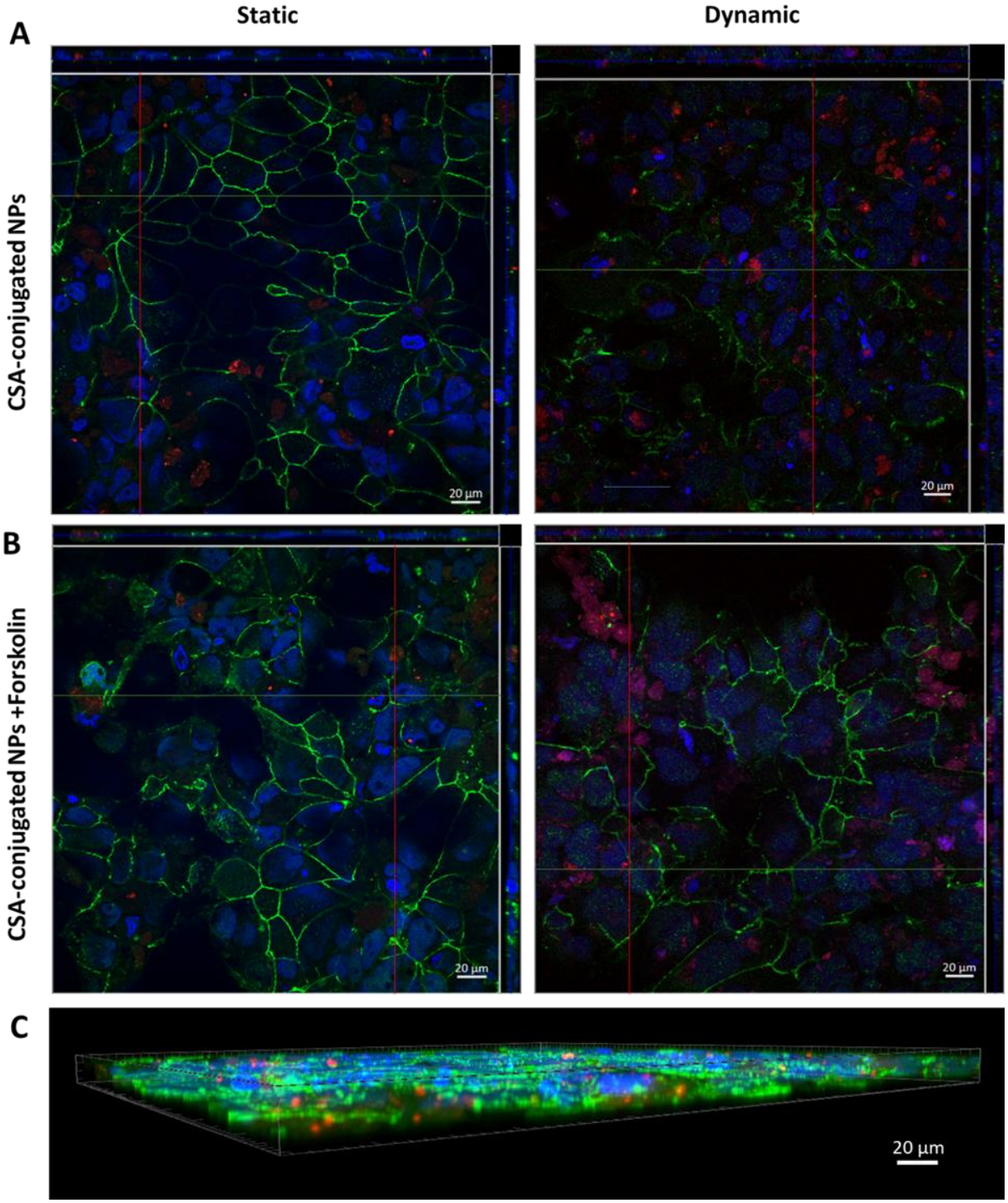

Figure 20: *Confocal microscope images to check the cell uptake and localization of the NPs. Orthogonal views of 3D confocal stacks in both static and dynamic conditions (by ZEISS ZEN 3.5 (blue edition).; A CSA-conjugated NPs. B CSA-conjugated NPs + Forskolin. C 3D image (by Imaris Viewer 9.9.1) illustrates the NP's presence inside the cells after washing the nanoparticles. Image slices showing NPs present on the surface will be excluded from uptake calculations. The cell nuclei are labelled in the blue color, tight junctions in the green color, and NPs shown in red color.*

4. Discussion

When placental abnormalities occur, this can have dire effects on both fetus development and the health of the mother.[163] However, treating placental diseases presents unique clinical challenges since they are difficult to manage without imposing side effects on the fetus and the mother. That is why there is a demand within the pharmaceutical research field to develop nanocarriers that can target the placental cells and minimize any potential side effects of the encapsulated drug that could compromise the health of the mother and the fetus. For example, there are several nucleic acid-based therapies that are currently being studied in an effort to target placental diseases such as preeclampsia.[164] However, these therapies are challenged by rapid degradation, interactions with toll like receptors (TLRs) leading to cytokine release and inflammatory responses, a lack of tissue selectivity, and rapid clearance from the blood by the kidneys. Therefore, encapsulating these therapies in nano formulations will lead to the development of safer and more effective therapies.[45] However, there is little research studying the cellular uptake of NPs after the syncytialization of trophoblastic placental cells, a natural phenomenon occurring as pregnancy progresses.[165] Further, the mechanical stimulation of the placental cells by the friction generated from flow, aka shear stress, is integral to placental development and function.[166,167] This is an emerging concept, and little is known about how the shear stress due to blood flow contributes to the response of placental cells to those targeted nanocarriers.

The purpose of this study was therefore to investigate the cellular uptake of CSA-conjugated liposomes before and after syncytialization under static and shear stress conditions. A mechanistic understanding of the impact of these physiological factors on the placental cell uptake of targeted nanocarriers is an important first step in developing nanocarriers to deliver therapies to the placenta throughout pregnancy. Several spectroscopic and imaging techniques are available to characterize cell association of NPs (a summed value of adhesion and uptake). However, measurement of cell uptake of NPs poses technical limitations to most of these techniques. For instance, flow cytometry is a highly sensitive technique that can quantitate fluorescent signals due to NPs associated with a single cell. However, flow cytometry cannot distinguish between signals inside the cells (cell uptake of NPs) and outside signals due to NPs adhering to the cell membrane (membrane-adhered NPs).[168] On the other hand, confocal imaging is the most widely used method for determining cell uptake of NPs by providing 3D location of NPs relative to a fluorescently-labelled cell membrane. However, it has a low throughput and only provides qualitative data (x-y-z images). To circumvent the former limitation, confocal imaging is usually followed by rigorous image analysis to provide quantitative data for comparing the different experimental conditions.[108,131,168]

PEGylated liposomes were chosen for this study based on their reported safety and effectiveness as drug delivery systems.[169] For our study, reproducible monodispersed liposomes were chosen as they produced reliable, uniform results which ensured that the various experimental conditions of

syncytialization and shear stress were the only parameters that varied between the different experiments. Furthermore, liposomes also provided us with the ability to perform surface functionalization in an effective manner. We therefore relied on microfluidic lab-on-a-chip technologies for the reproducible preparation of liposomes and the precise control over the size and PDI. The microfluidic hydrodynamic focusing technique developed by Jahn et al. relies on the use of microfluidic chips with cross flow geometry.[170] A stream of organic solution of amphipathic lipids is forced into the inner channel at a controlled flow rate. The lipid stream is intersected and sheathed with two lateral streams of aqueous solution flowing at a faster rate as shown in Figure A. Thus, the lipid-containing stream is hydrodynamically focused into a narrow sheet. During this process, the diffusion of alcohol into the aqueous phase, and vice-versa, triggers self-assembly of liposomes whose size controlled by the flow rate ratio of the two phases and the total flow rate. Liposomes between 50-200 nm are reported to be within the optimal range for drug delivery and to experience a longer half-life prior to detection by the immune system, therefore a size of 50 nm prior to CSA conjugation was preferred.[171,172] Furthermore, microfluidic synthesis allows for high NP yield.[45] Fine control on the different NP parameters has a huge impact on successful translation of targeted nanocarriers.[173] Cholesterol in the bilayer was incorporated as a membrane stabilizer increasing the glass transition temperature.

To target the placental cells, we used CSA to decorate the liposomes.[140] This was achieved in a two-step functionalization process. First, the carboxylic groups on the surface of the liposomes containing (DSPE-PEG(2000)-COOH) were activated with EDC/NHS mixture. In the second step, the liposomes react with the N-terminus of CSA leaving the C-terminus of the adhesion molecule free for the interaction with CSA receptors that are present on the surface of trophoblastic placental cells such as BeWo b30.[140,174] Additionally, due to the incorporation of rhodamine labelled PE within the surface of the liposome, we can track NP uptake.

To simulate conditions of shear stress and syncytialization in the lab, we have developed a “placenta-on-a-chip” model with a recirculating culture media, set to precise flow rates which corresponds to shear stress values within the physiological range (Figure). Additionally, forskolin was added to the culture media to trigger syncytialization following earlier reports.[161] The process of syncytialization upregulates the release of human chorionic gonadotropin (β-hCG) as forskolin activates the protein kinase A pathway within the syncytiotrophoblasts.[175] This is because β-hCG is a heterodimeric protein that is partially produced through the multinucleated trophoblast cell products of syncytialization.[175] Therefore, to measure the extent of syncytialization quantitatively, we measured the concentration of secreted β-hCG in cell media at different time intervals (Figure A). Quantitative measurements of β-hCG secretions were further confirmed qualitatively through imaging using confocal microscopy (Figure B). Over a 72-hour period, we only observed significant increase in the extent of syncytialization under dynamic conditions. It should be noted however, that cell treatment with forskolin under static conditions did not result in significant change in β-hCG secretion, within the sensitivity limit of the assay. This implies that the dynamic placenta-on-a-chip models mimic the micro-physiological conditions required for syncytialization to occur to a certain extent without the need for chemical induction. As expected, the extent of syncytialization in the dynamic condition was further increased following chemical induction and with longer exposure time to forskolin. This increase in syncytialization may indicate a more latent stage of placental barrier syncytialization which could influence cellular uptake in the dynamic conditions.

To date, the impact of trophoblast syncytialization on placental uptake of NPs is not known. Our cell uptake results under static conditions show a contribution of cell exposure to forskolin as well as the time of exposure in the cell uptake results (Figure B). For instance, we observed an increase in cell uptake of liposomes after exposure to forskolin for 48 h and 72 h, compared to those not exposed to forskolin. Additionally, as evident from our dynamic cell uptake experiments, higher cell uptake of both control and CSA-conjugated liposomes was observed under dynamic conditions (Figure C). This could be partially justified by the different degrees in syncytialization in which exposing the cells to dynamic conditions resulted in significantly higher degree of syncytialization and β-hCG secretion (Figure A). This is unexpected if we consider the findings from Moore et al.[176] They observed an increase in barrier function, as measured by electric cell-substrate impedance sensing, through syncytialization. They attributed this to the formation of extracellular matrix which projects from the apical side of syncytiotrophoblasts into the lumen of the maternal side of the placenta. However, the placental barrier function is the outcome of different factors which influence the permeability of the barrier and uptake into the placental cells. For instance, Liu et al. reported that the cell seeding density, incubation period, and forskolin treatment all act to affect permeability across a monolayer of BeWo cells.[177] Using a static *in vitro* model, they observed an enhanced passage of the polyunsaturated essential fatty acid linoleic acid across a BeWo monolayer on treatment with forskolin.[177] Further, trophoblast syncytialization was recently shown to be associated with higher levels of macropinocytosis promoting the uptake of fluid phase-derived molecules.[178] While these prior works did not investigate placental cell uptake of NPs following syncytialization specifically, their findings affirm our hypothesis that the various states of BeWo cells throughout forskolin induction and natural syncytialization can influence membrane transporters and the extent of cellular uptake of NPs. Insights from these earlier studies support our findings that little change in placental cell permeability can occur within the first 3 days of exposure to forskolin and further measurements over multiple time periods need to be performed to gain greater insight into the effect of syncytialization on cell uptake over time. As suggested by Liu et al., it could be that over time, the weaker cells begin to be sloughed off revealing a more permeable monolayer beneath.[177] This is even more likely when the dynamic environment is considered in the *in vitro* model as the shear stress generated by the moving media may act to remove weakened cells or to weaken the cell membrane, resulting in enhanced cell permeability and consequently higher cell uptake of NPs. However, Liu et al. findings also suggest that while forskolin is known to increase neutral amino acid carriers along the BeWo cell surface, it could also be the case that forskolin and/or cell differentiation due to syncytialization could upregulate the presence of other transporters. This hypothesis is supported by the expression of several transport and receptor proteins on the surface of syncytiotrophoblasts.[179] Altogether, our findings imply that the longer gestation period associated with more syncytialization could result in higher cell uptake of NPs. Future studies are required to investigate the mechanism of cell uptake of NPs with broad range of physicochemical parameters, e.g., size, composition, and surface charge. This will guide the selection of the appropriate NP formulations for the treatment of placental diseases at the different stages of pregnancy.

While previous works have studied the process or rate of syncytialization under static conditions or dynamic conditions, no studies have compared how the difference in static or dynamic syncytialization impacts NP uptake. While understanding NP uptake under static conditions gives us a look into cell mechanisms and uptake rates, these values give little information about the dynamic microphysiological environment of the placenta. Higher cell uptake of liposomes under dynamic

conditions could be further justified by the dense microvilli formation on the cell surface under dynamic conditions versus static conditions (Figure C). Microvilli formation is essential for efficient transport, uptake of nutrients, and waste removal as they increase the overall surface area of the cell. This may allow for more cell surface area exposed to the NPs resulting in more cell uptake. Our results showing shear stress stimulated microvilli formation along the surface of placental cells are confirmed by Blundell et al. as they also displayed higher levels of microvilli formation under dynamic conditions.[161] These microvillous areas also contain a wide array of receptor proteins which can influence cell uptake as they also observed higher values of glucose transfer in dynamic conditions at rates that closely match the *ex vivo* conditions.[160]

CSA targeting liposomes were chosen based on a previous investigation from Zhang et al.[140] In this, they discussed the presence of CSA receptors on trophoblastic cells and the ability for CSA-conjugated NPs to bind to these receptors on placental trophoblasts and be internalized after 30 minutes of exposure. Our results also show higher mean values of cell uptake for the CSA-conjugated liposomes in several comparable static conditions except for the 72 h forskolin condition. Similar results were observed in dynamic conditions not including forskolin induction. CSA-conjugated NPs in these former conditions displayed higher rates of cell uptake and internalization compared to control samples (Figure D). However, the combined effect of dynamic environment and syncytialization were shown to outweigh the effect of surface functionalization of the liposomes evident from non-significant differences in cell uptake between control and CSA-conjugated liposomes under dynamic conditions (Figure E). This might suggest that the engineered CSA-conjugated liposomes are suited for earlier stages of pregnancy and further optimization is required for later stages of pregnancy. This result, as well as the results found in the 72 h conditions, may agree with previous research as it has been suggested that chondroitin sulfate proteoglycans, like CSA, are expressed at higher levels at the end of the first semester or beginning of the second semester.[180] Further, the different outcomes between the static and dynamic conditions highlight the need for dynamic biomimetic placenta-on-a-chip models in evaluating NPs since the traditional static models clearly do not reflect the complex dynamism of the placenta.[108] We therefore submit that future studies should use dynamic models for screening of the different the surface-functionalized NP formulations before proceeding with preclinical studies. These models should consider trophoblast syncytialization since there is a clear impact of syncytialization on cellular uptake of NPs (Figure F).

Another confounding factor that may have contributed to the results of cell uptake of CSA-conjugated versus control NPs is the difference in surface charge; zeta potential decreased from 11.48 ± 4.36 (slight positive charge) to -25.5 ± 2.81 mV (negative charge) for control liposomes and CSA-conjugated liposomes, respectively. Positively charged NPs were shown earlier to favor higher adhesion with the negatively-charged cell membranes resulting in higher internalization compared to neutral and negatively-charged NPs.[181] However, surface charge was recently shown as not a key factor to steer placental uptake and transport of titanium dioxide NPs. The conflicting results in the NP-placenta literature on the effect of surface charge on interaction of NPs with the placenta warrants future mechanistic studies using NPs with different physicochemical parameters under biomimetic conditions, including trophoblast syncytialization.[141]

5. Conclusion

Using the placental secretion of β-hCG as a key hallmark of trophoblast syncytialization,[182] we could show that the syncytialization of BeWo cells was intrinsically induced under dynamic conditions. The extent of syncytialization of BeWo cells further increased on exposure to forskolin and significantly increases on increasing the time of exposure to forskolin. Therefore, it can be concluded that placental trophoblast syncytialization is dependent on these three factors: shear forces, chemical induction, and the exposure time to the chemical inducer. Interestingly, we were able to show the impact of syncytialization and the extent of cell fusion on cell uptake of liposomes. Extrapolating these results to *in vivo* scenarios could imply that liposomes interact differently with the placenta at the different stages of pregnancy which is likely due to the difference in expression of transport and uptake receptors at the different trimesters. Future studies are required to develop a more mechanistic understanding of cell uptake of NPs along the gestation period. Proteomic studies together with immunostaining experiments would also be beneficial to identify harnessed receptors in cell uptake of NPs. This also includes a systemic approach of investigating different NPs with different physicochemical parameters (including NP type, size, shape, and surface charge) and peptide conjugation for a more global view on cell uptake of engineered NPs. Importantly, our study submits that creating dynamic models of the placenta that consider dynamic changes of the barrier along pregnancy is necessary to allow for a biomimetic resemblance of how the placenta will interact with NPs *in vivo*. The results of these experiments will accurately guide tailoring the engineered properties of NPs for predictable targeted efficiencies along the human gestation period. Our work will also assist future attempts in understanding drug targeting and drug delivery mechanisms to the placenta to treat placental-related diseases.

Acknowledgement. The work was supported by the Natural Sciences and Engineering Research Council (NSERC Discovery Grant-RGPIN-2020-05679 and NSERC RTI-2021-00374), New Frontiers Research Fund – Exploration Grant NFRFE-2019-00210), SickKids Foundation in partnership with the Canadian Institutes of Health Research (NI22-1088R), and University of Manitoba. A. A. is supported by the RFHS Graduate Studentship from the University of Manitoba.

Chapter 4: Conclusion and Outlook

LNPs have achieved widespread adoption as a safe nucleic-acid delivery vehicle, which propounds its potential in targeted fetal gene therapies. Microfluidic synthesis has enabled the formation of a monodisperse reproducible library of LNPs with high encapsulation efficiency. Varying the lipid types and molar percentages enabled the formation of LNPs with diverse physiochemical properties. Using machine learning algorithms to model the LNPs colloidal properties (size and zeta potential), the lipid composition and antibody conjugation, showed the highest impact. Whereas the process parameters, such as the synthesis and storage buffers or the synthesis flow rates showed little to no effect.

The placental barrier is a unique dynamic biological barrier, as its structure and function change significantly during the different stages of pregnancy. We developed different models to capture those varying stages. The first model utilized placental cells only, the second model included fetal endothelial cells in addition to placental cells, and the third model captured the syncytialization process chemically induced by forskolin. The barrier structure and functionality were confirmed using immunofluorescence and dextran transport assays.

The different LNPs with ionizable lipids showed no toxicity on the placental and fetal cells, even at very high concentrations. However, LNPs including permanently cationic lipids showed toxicity at high concentrations of LNPs. Further, LNPs showed no effect on fetal development when tested in an ex-vivo lung explant model. This was proven by the normal lung airspace and the normal apoptosis and proliferation levels. This suggests the potential safety of LNPs for fetal gene therapies, especially for targeting the lung, as the case in congenital diaphragmatic hernia (CDH).

We then conducted a thorough LNPs transplacental transport study. Several parameters related to the composition of LNPs showed significant impact on placental transport such as the antibody orientation, the PEGylated lipid type, and the ionizable lipid. Whereas some parameters showed no effect on transport, such as the LNPs pKa. In addition, the placental model design which reflects the structure of the placenta at the varying stages of pregnancy played a role. The model parameters that exhibited significant effects are the trophoblast syncytialization, fetal endothelial cells, cell seeding density, and the fetal bovine serum concentration. On the other hand, machine learning algorithms that model hundreds of transport datapoints together revealed the importance of more general predictors such as the LNPs size, zeta potential, and concentrations.

The siRNA transfection studies showed the significant role of permanent cationic lipids and lpids to the siRNA mass ratio in driving preferential transfection in lung cells. This confirms previous knowledge about the importance of the N/P ratio in lung targeting. Our combined transport and transfection model revealed the potential of LNPs in transfecting fetal cells after bypassing the placental barrier, implying they have passed intact to fetal circulation. Besides, maximizing nucleic acid transfection in fetal cells relative to placental cells is crucial to develop safe therapeutics for congenital diseases, increasing the chance to restore normal fetal development before irreversible damage.

Altogether, this research represents an important step towards establishing the safety and efficacy of LNPs delivery to fetal cells, which propounds LNPs transplacental transport as a new route for targeting deadly congenital diseases. We also believe our approach could inspire future work on integrating machine learning models and high throughput characterization techniques in the preclinical development of nanomedicines.

The placenta-on-a-chip model poses several phenotypes of human placenta like microvilli that cover the entire cell surface of most trophoblasts. Also, the model mimics the syncytialization process happening in the human placenta by showing progressive intercellular fusion of cytotrophoblasts that formed a multinucleated barrier termed the syncytiotrophoblast. Since the dynamic flow increased NPs uptake in trophoblast cells, we believe it's important to study LNPs transplacental transport in the dynamic placenta-on-a-chip model. The dynamic forces on the LNPs combined with the dynamic forces-induced changes in the placental barrier could lead to differences in LNPs uptake, transport percentage and kinetics.

Appendix 1: Chapter 2 Supplementary Tables and Figures

Table S2: *Full name and source for the lipids used in making the lipid nanoparticles.*

Lipid Abbreviations	Full Name	Vendor
D-lin MC3 DMA	(6Z,9Z,28Z,31Z)-Heptatriaconta-6,9,28,31-tetraen-19-yl 4-(dimethylamino)butanoate	Med Chem EXPRESS
DODAP	1,2-dioleoyl-3-dimethylammonium-propane	Avanti Polar
DSPC	1,2-distearoyl-sn-glycero-3-phosphocholine	Avanti Polar
Cholesterol	Cholesterol (plant-derived)	Avanti Polar
DSPE-PEG2000	1,2-distearoyl-sn-glycero-3 phosphoethanolamine-N-[methoxy(polyethylene glycol)-2000] (ammonium salt)	Avanti Polar
DOPE-PEG2000	1,2-dioleoyl-sn-glycero-3-phosphoethanolamine-N-[methoxy(polyethylene glycol)-2000] (ammonium salt)	Avanti Polar
DMG-PEG2000	1,2-dimyristoyl-rac-glycero-3-methoxypolyethylene glycol-2000	Avanti Polar
DSPE-PEG2000-COOH	1,2-distearoyl-sn-glycero-3-phosphoethanolamine-N-[carboxy(polyethylene glycol)-2000] (sodium salt)	Avanti Polar
DSPE-PEG2000-NH2	1,2-distearoyl-sn-glycero-3-phosphoethanolamine-N-[amino(polyethylene glycol)-2000] (ammonium salt)	Avanti Polar
DSPE-PEG2000-Malimide	1,2-distearoyl-sn-glycero-3-phosphoethanolamine-N-[maleimide(polyethylene glycol)-2000] (ammonium salt)	Avanti Polar
DOTAP (cationic)	1,2-dioleoyl-3-trimethylammonium-propane (chloride salt)	Avanti Polar
18:1 PA	1,2-dioleoyl-sn-glycero-3-phosphate (sodium salt)	Avanti Polar
DOPE-Rhodamine B	1,2-dioleoyl-sn-glycero-3-phosphoethanolamine-N-(lissamine rhodamine B sulfonyl) (ammonium salt)	Avanti Polar
DSPE- Cy7	1,2-distearoyl-sn-glycero-3-phosphoethanolamine-N-(Cyanine 7)	Avanti Polar

Table S2: *Microscopy imaging for the in-vitro and ex-vivo experiments; image acquisition parameters and image display parameters.*

Imaging Machine	Experiment	Imaging Parameters	Image Display Parameters
Spinning Disk Confocal Microscope (Quorum technologies, Canada)	ZO-1 staining (Figure 4)	Lenses: 63x (oil) **DAPI:** laser power= 70, exposure time= 200 ms **ZO-1 (AF647):** laser power= 80 , exposure time= 200 ms	Maximum Intensity projection. <u>BeWo Layer:</u> **DAPI:** Min= 30 Max= 1400 **ZO-1:** Min= 600 Max= 3000 <u>HUVEC Layer:</u> **DAPI:** Min=200 Max= 700 **ZO-1:** Min= 500 Max= 2000
	FcRn staining (Figure 4)	Lenses: 63x (oil) **DAPI:** laser power= 70, exposure time= 200 ms **FcRn (AF647):** laser power= 80 , exposure time= 200 ms	Maximum Intensity projection. **DAPI:** Min= 30 Max= 1500 **fcRn:** Min= 700 Max= 6000
	LNPs cellular association (Figure 10)	Lenses: 63x (oil) **DAPI:** laser power= 70, exposure time= 200 ms **Rhodamine-B:** laser power= 60, exposure time= 100 ms **ZO-1 (AF647):** laser power= 80, exposure time= 200 ms	Maximum Intensity projection. **DAPI:** Min= 200 Max= 2500 **Rhodamine-B:** Min= 100 Max= 500 **ZO-1:** Min= 1500 Max= 4000
Cell Discoverer- 7 (ZEISS, Germany)	siRNA Transfection (Figure 12)	Lenses: 20x(0.95) and 1X **Hoechst:** intensity= 20% exposure time= 30 ms **siRNA-AF488:** intensity=50%, exposure time= 150 ms	**Hoechst:** Min= 0 Max= 12000 **siRNA-AF488:** Min= 50 Max= 2800

		WGA-AF647: intensity= 50%, exposure time= 35 ms	**WGA-AF647:** Min= 100 Max= 5500
Axioscan Microscope Slide Scanner (ZEISS, Germany)	H&E (Figure 13) Apoptosis (Figure 14) Proliferation (Figure 15)	Lenses: 20X NA 0.8 **DAPI:** exposure time= 1 ms **Active Caspase-3(AF647):** exposure time= 125 ms **ki-67 (AF647):** exposure time=100 ms	

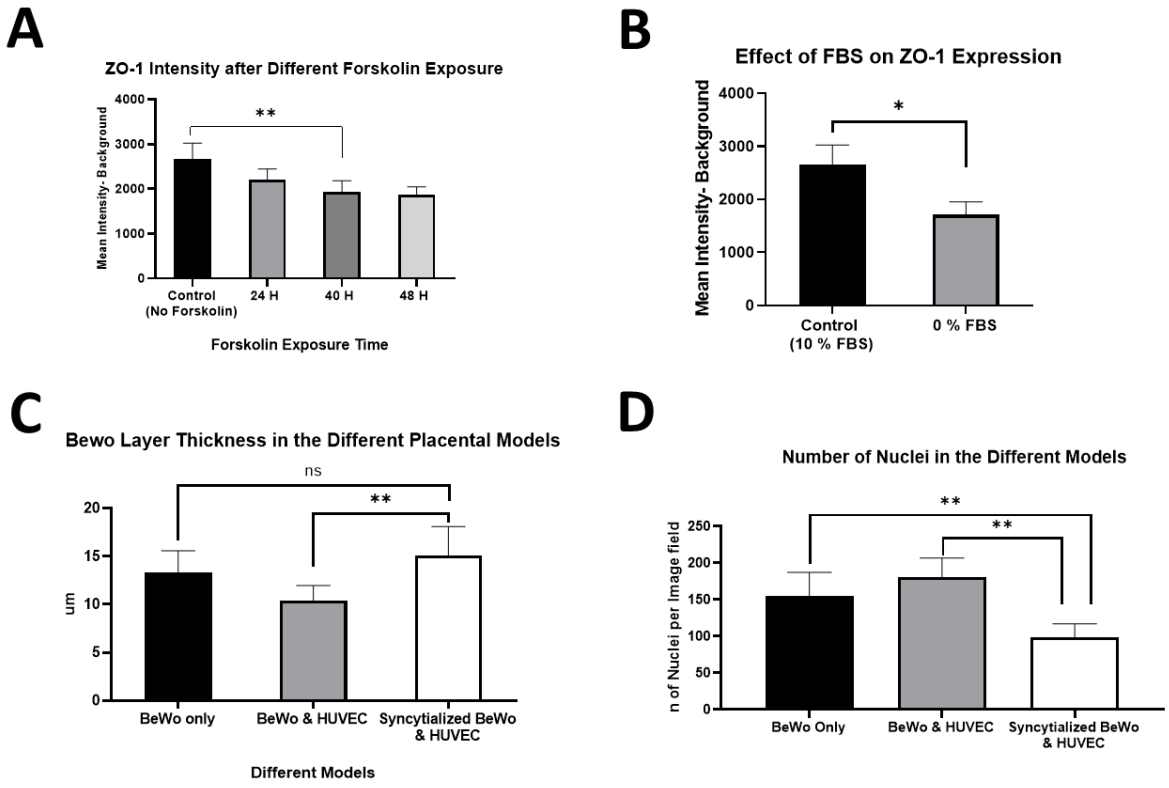

Figure S1: *Placental Models Development. (A) Tight Junction expression after different time exposure to 50uM of forskolin, analyzed by immunostaining of ZO-1 antibody on BeWo cells. (B) Effect of fetal bovine serum concentration on the media on tight junction expression on BeWo cells. (C) Thickness of the BeWo layer in the different placental models. (D) Number of Nuclei per image field in the different placental model using ImageJ analysis.*

Supplementary Methods for MTT Viability Assay:

After 24 hours of exposure to different concentrations of LNPs, media was removed, and cells were washed twice with sterile 1x DPBS. Then, 100 ul media with 10 ul MTT was added for each well and incubated for 2 hours at 37º Celsius. Then, the media was removed gently and 100 ul of DMSO was added to each well. The plates were shaken gently for 5 minutes to solubilize the crystals in DMSO. Finally, the absorbance was measured on a plate reader at wavelength of 570 nm.

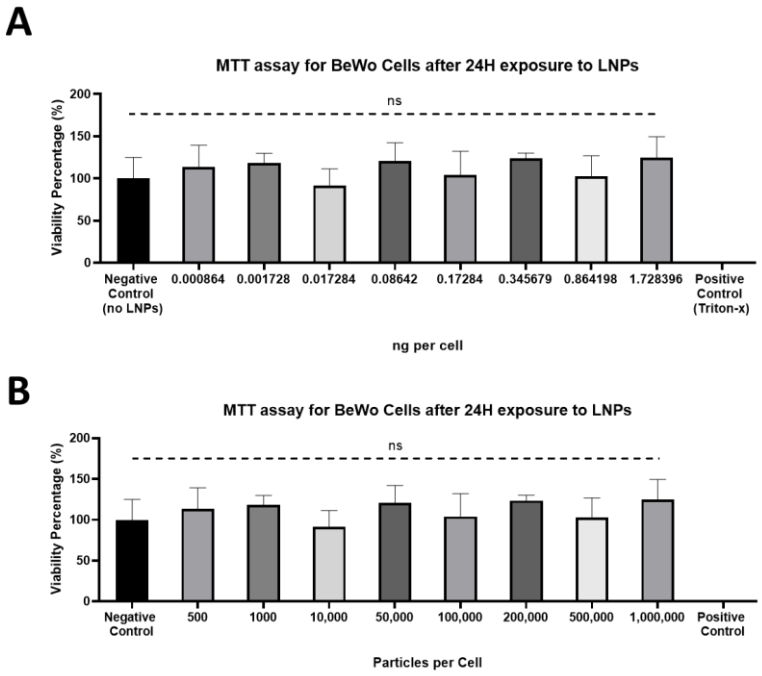

Figure S2: *MTT Viability Assay for Different concentrations of LNPs on BeWo cells. (A) LNPs concentration reported as ng per cell. (B) LNPs concentration reported as particles per cell.*

Contineous Variables					
Feature	Min	Q1	Median	Q3	Max
LNP Zeta Potential	-38.9	-20.9	-13.9	7.155	38
LNP Size	75.5	97.8	116.8	142.15	251.7
No. of LNPs per Cell	92771	168797	337059	603630	1068257
Mass of LNPs per Cell	0.13	0.15	0.65	0.65	0.65
Distance Between Antibodies (nm)	33.9	122.1	∞	∞	∞
No. of Antibodies per LNP	0	0	0	12.5	158.7
PEG Percentage	0.5	1.5	1.5	1.5	4.5
Seeding Density (cells / cm^2)	100,000	100,000	100,000	100,000	500,000
Cationic Lipid Percentage	0	0	0	0	50
Anionic Lipid Percentage	0	0	0	0	30

Low Feature Value Moderate Feature Value High Feature Value

***Figure S3**: Summary for Input Features with Continuous Values in the Transport Dataset*

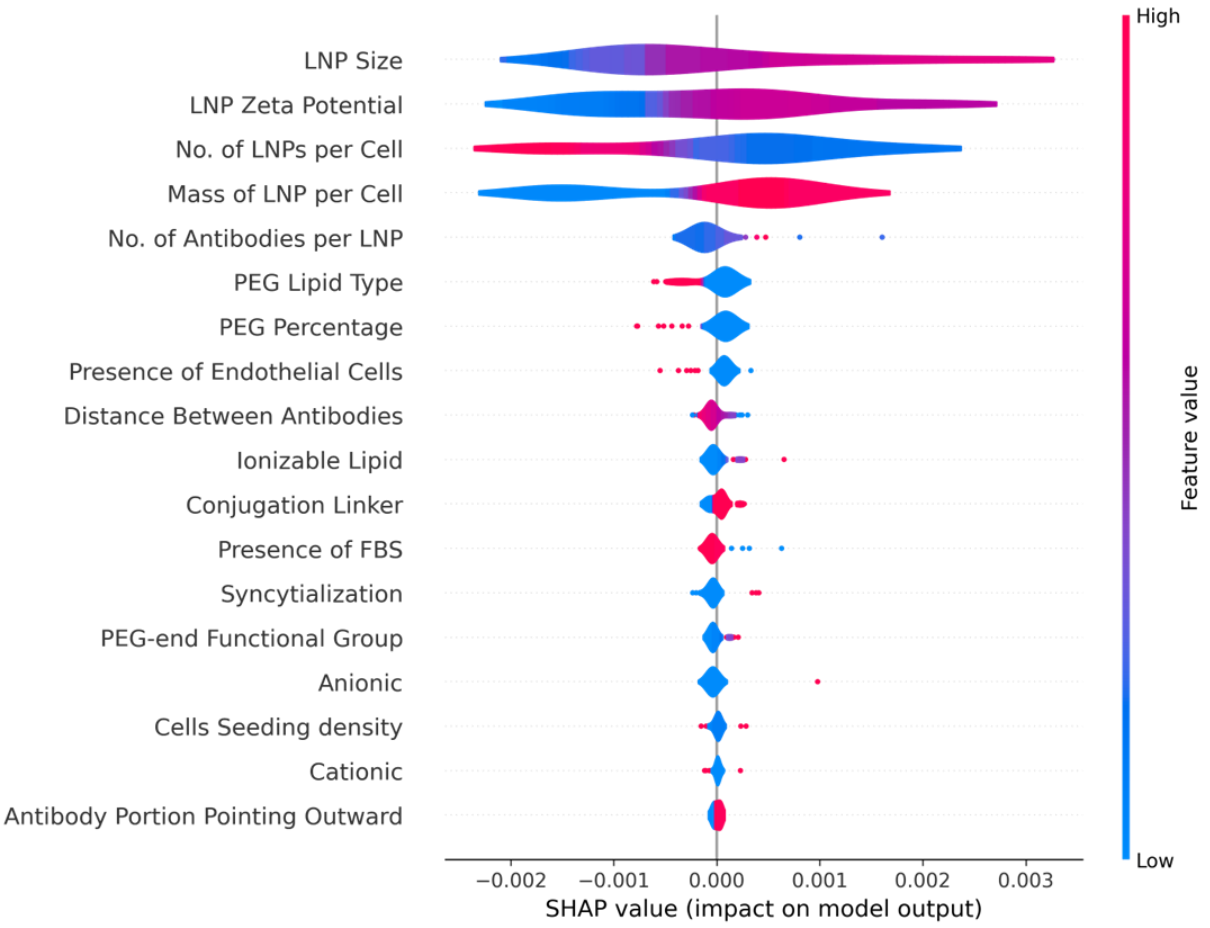

Mean	Min	Max
0.00467	0.00004	0.01765

Figure S4: *Shapley Additive Explanation (SHAP) of Machine Learning Modelling for Average Apparent Permeability using Random Forest (RF) algorithm.*

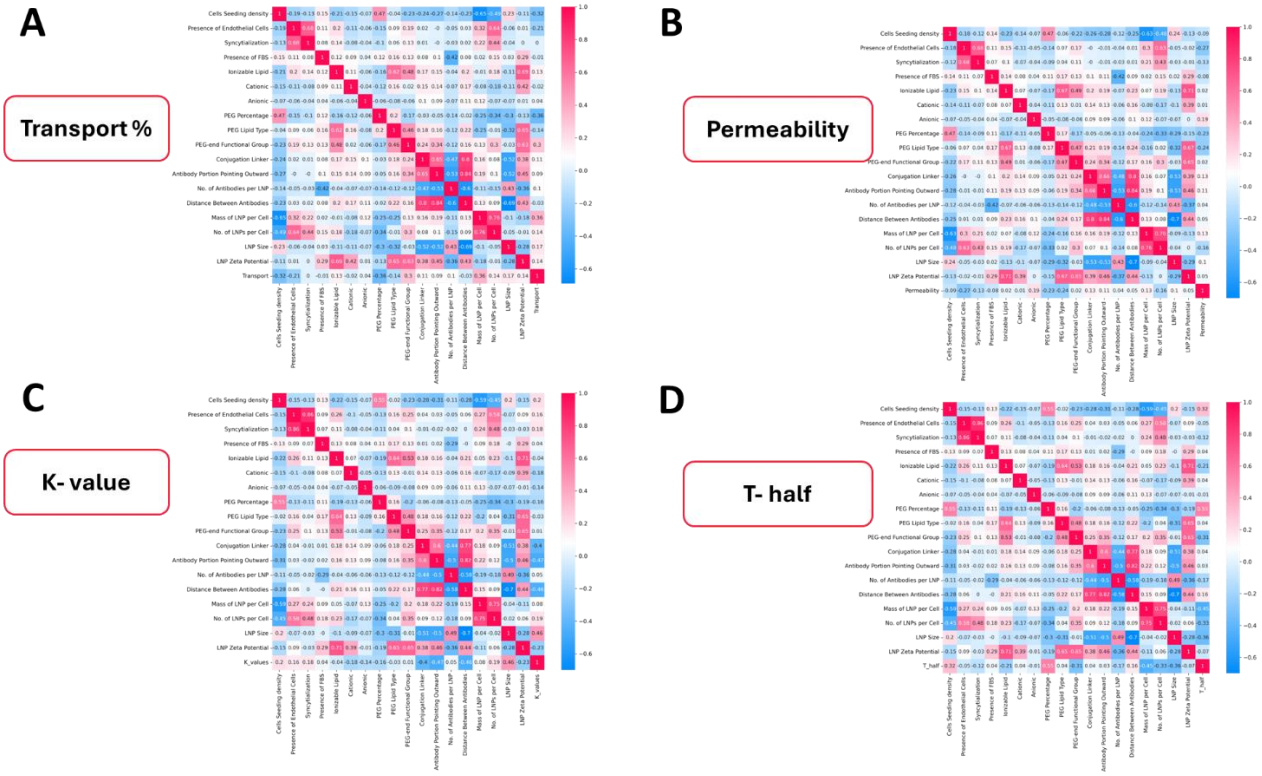

Figure S5: *Heat Map for the Correlation between Features in the different Output Datasets. (A) 24 Hours transport percentage dataset. (B) Average apparent permeability dataset. (C) Logistic growth model K-values dataset. (D) Logistic growth model T-half dataset.*

A

T- half

	RF	XGB	DT	Lasso	LightGBM	SVR
MAE	9.8	10.8	11.5	11.5	11.9	11.9
MedAE	7.8	8.5	7.6	10.3	9.5	9.7
RMSE	12.4	13.8	15.2	13.8	14.8	15.6
MSE	154.1	189.8	231.6	191.6	220.5	243.7

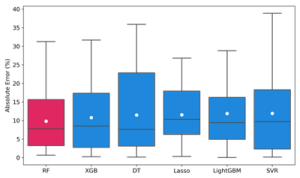

B

K- value

	RF	XGB	DT	Lasso	LightGBM	SVR
MAE	0.0301	0.0322	0.0351	0.0369	0.037	0.0728
MedAE	0.0205	0.0167	0.0187	0.0325	0.0298	0.0765
RMSE	0.0483	0.0521	0.0566	0.0539	0.0515	0.0799
MSE	0.0023	0.0027	0.0032	0.0029	0.0027	0.0064

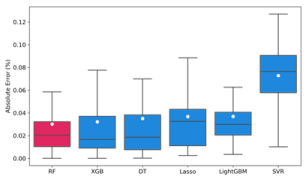

C

Transport %

	RF	XGB	Lasso	LightGBM	SVR	DT
MAE	13.1	14.5	14.6	15.5	15.9	17.0
MedAE	10.1	12.8	12.1	13.5	13.1	9.9
RMSE	17.9	18.9	18.8	20.0	20.9	24.8
MSE	319.4	356.4	352.1	401.5	438.1	613.1

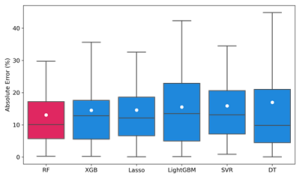

D

Permeability

	RF	LightGBM	XGB	Lasso	DT	SVR
MAE	0.00338	0.00363	0.00365	0.00380	0.00405	0.00562
MedAE	0.00280	0.00296	0.00251	0.00342	0.00178	0.00652
RMSE	0.00432	0.00467	0.00496	0.00470	0.00630	0.00622
MSE	0.00002	0.00002	0.00002	0.00002	0.00004	0.00004

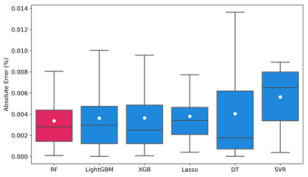

Figure S6*: Error Values for the Different Machine Learning Models on the Different Output Datasets. (A) Logistic growth model T-half. (B) Logistic growth model K-values dataset. (C) 24 Hours transport percentage dataset. (D) Average apparent permeability dataset. The model with lowest error value is shown in red while other models are shown in blue.*

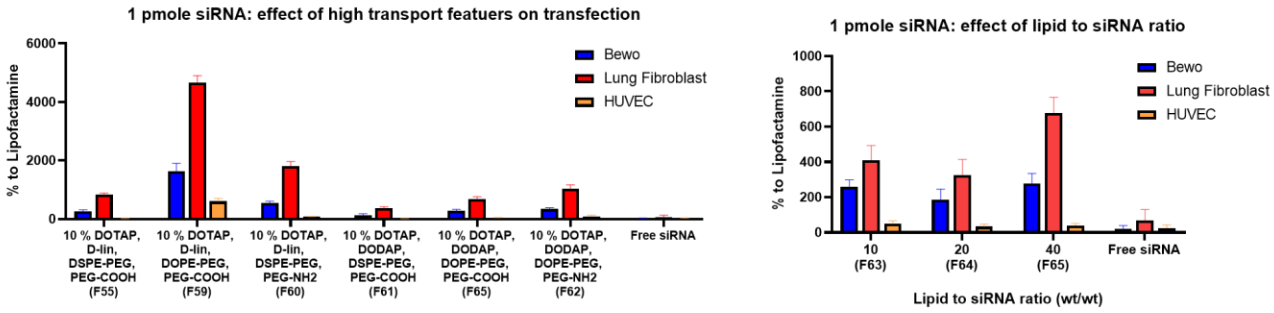

Figure S7: *siRNA-LNPs Transfection using a low dose of 1 pmole of siRNA per well. (A) Testing the effect of different lipid compositions on transfection. (B) Effect of lipid to siRNA mass ratio on transfection.*

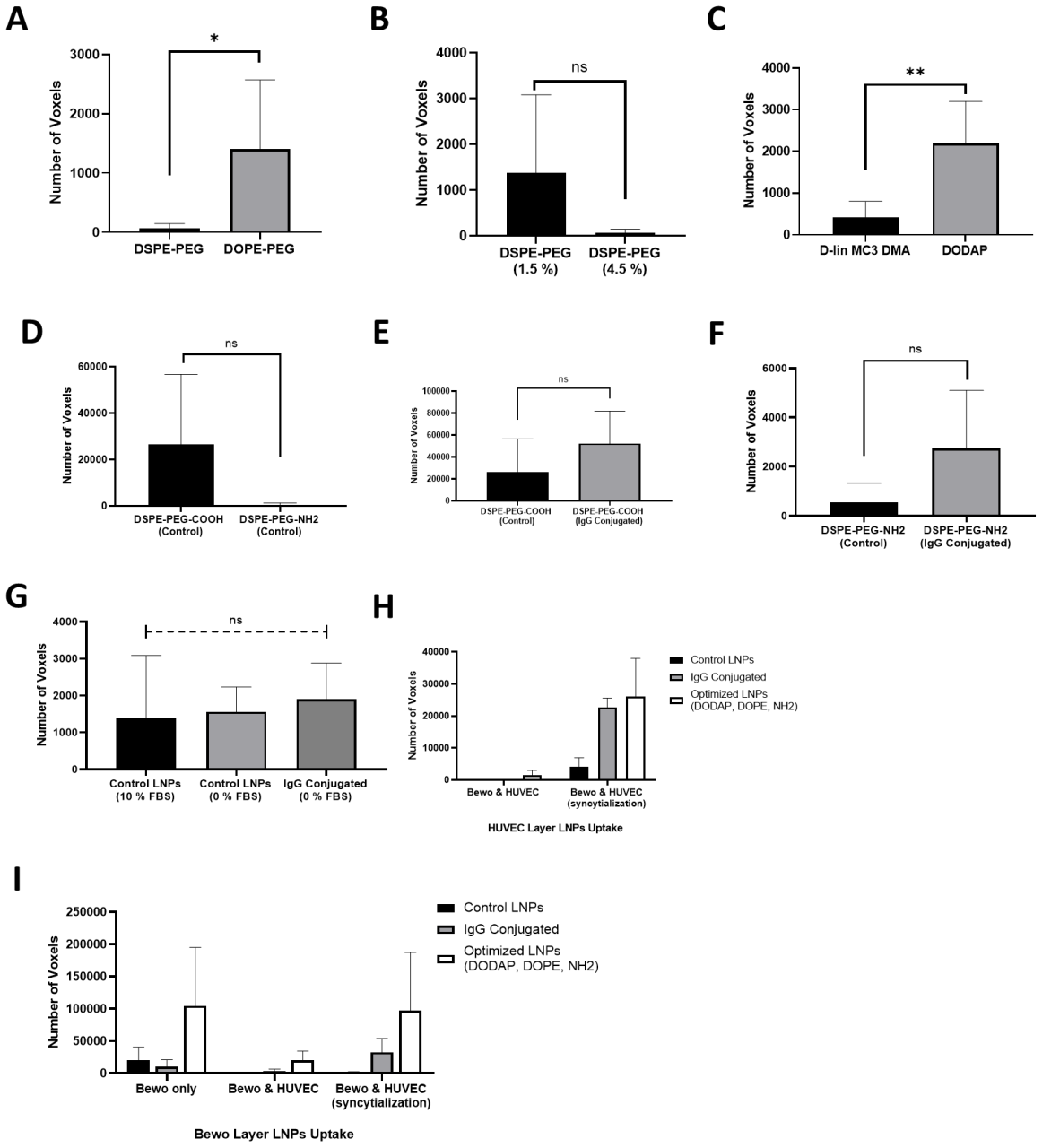

Figure S8: *LNPs cellular association using imaris software analysis to compare the number of voxels. (A) The effect of PEGylated lipid tail unsaturation on LNPs association with BeWo cells. (B) The effect of PEGylated lipid molar percentage on LNPs association with BeWo cells. (C) The effect of ionizable lipid on LNPs association with BeWo cells. (D) The effect of PEGylated lipid end-functional group on LNPs association with BeWo cells. (E-F) The effect of IgG conjugation on LNPs association with BeWo cells. (G) The effect of growth media FBS percentage on LNPs association with BeWo cells. (H) Different formulations association with HUVEC cells in the different placental models. (I) Different formulations association with BeWo cells in the different placental models. Refer to Appendix 2 for the detailed composition and characterization of each formulation.*

Appendix 2: LNPs Formulations and Characterization Dataset

A	B	C	D	E	F	G	H	I	J	K	L	M	N	O	P	Q	R	S	T	U	V	W
	Inputs																				Outputs	
	Ionizable lipids				non-functionalized PEG			Functionalized-PEG			SORT lipid		Flourescent Lipic									
M.W	642	648	387	790	2780	2801	2509	2780	2790	2940	698	722.5	1300	1332								
LNPs ID	D-lin-MC3	DODAP	Cholesterol	DSPC	DSPE-PEG	DOPE-PEG	DMG-PEG	DSPE-PEG-COOH	DSPE-PEG-NH2	DSPE-PEG-Malimid	DOTAP	18:1 PA	DOPE-Rhodamine	DSPE-cy7	total lipid conc (mg/ml)	Buffer synthesis	total flow rate	flow rate ratio	Buffer dispersion	n of abs per one LNP	Size	zeta potential
F1	49.75	0	38.3	9.95	1.00	0	0	0	0.5	0	0	0	0	0.5	2	Acetate	90	4	PBS	0	119.9	4.1
F2	0	49.75	38.3	9.95	1.00	0	0	0	0.5	0	0	0	0	0.5	2	Acetate	90	4	PBS	0	82	-21.6
F3	24.75	0	19.1	4.95	0.25	0	0	0	0.5	0	50	0	0	0.5	2	Acetate	90	4	PBS	0	142	21.4
F4	0	24.75	19.1	4.95	0.25	0	0	0	0.5	0	50	0	0	0.5	2	Acetate	90	4	PBS	0	130.9	14.2
F5	50	0	38.5	10	1	0	0	0.5	0	0	0	0	0	0	2	MES	90	5	PBS	0	126.6	4.9
F6	44.93	0	34.6	8.99	1	0	0	0.5	0	0	10	0	0	0	2	MES	90	5	PBS	0	129.3	22.0
F7	24.63	0	19.0	4.93	1	0	0	0.5	0	0	50	0	0	0	2	MES	90	5	PBS	0	130.9	37.4
F8	49.75	0	38.3	9.95	1	0	0	0.5	0	0	0	0	0.5	0	2	MES	90	5	PBS	0	90	-14.4
F9	24.88	0	19.2	4.98	1	0	0	0.5	0	0	49	0	0.5	0	2	MES	90	5	PBS	0	118.3	10.8
F10	35	0	27.0	7	1	0	0	0.5	0	0	0	29	0.5	0	2	MES	90	5	PBS	0	106.6	-7.8
F11	0	49.75	38.3	9.95	1	0	0	0.5	0	0	0	0	0.5	0	2	MES	90	5	PBS	0	130	7.8
F12	48.25	0	37.1	9.65	0	4	0	0.5	0	0	0	0	0.5	0	2	MES	90	5	PBS	0	81	-19.6
F13	48.25	0	37.1	9.65	4	0	0	0.5	0	0	0	0	0.5	0	2	MES	90	5	PBS	0	79.5	-16.7
F14	49.75	0	38.3	9.95	1	0	0	0.5	0	0	0	0	0.5	0	2	MES	90	5	PBS	0	107.2	-21.2
F15	49.75	0	38.3	9.95	1	0	0	0.5	0	0	0	0	0.5	0	2	MES	90	5	PBS	118.9	117.6	-26.5
F16	49.75	0	38.3	9.95	1	0	0	0.5	0	0	0	0	0.5	0	2	MES	90	5	PBS	0	92.9	-20.9
F17	49.75	0	38.3	9.95	1	0	0	0.5	0	0	0	0	0.5	0	2	MES	90	5	PBS	158.7	171	-38.9
F18	49.75	0	38.3	9.95	1	0	0	0	0.5	0	0	0	0.5	0	2	MES	90	5	PBS	0	109.3	6.6
F19	49.75	0	38.3	9.95	1	0	0	0	0.5	0	0	0	0.5	0	2	MES	90	5	PBS	31.2	187.8	3.0
F20	49.75	0	38.3	9.95	1	0	0	0.5	0	0	0	0	0.5	0	2	MES	90	5	PBS	0	152.1	-13.1
F21	49.75	0	38.3	9.95	1	0	0	0.5	0	0	0	0	0.5	0	2	MES	90	5	PBS	20.7	150.2	-22.5
F22	49.75	0	38.3	9.95	1	0	0	0	0	0.5	0	0	0.5	0	2	MES	90	5	PBS	0	175.4	Missing
F23	49.75	0	38.3	9.95	1	0	0	0	0	0.5	0	0	0.5	0	2	MES	90	5	PBS	46.3	186.1	-15.9
F24	49.75	0	38.3	9.95	1	0	0	0.5	0	0	0	0	0.5	0	2	MES	90	5	PBS	0	129.6	-12.7
F25	49.75	0	38.3	9.95	1	0	0	0.5	0	0	0	0	0.5	0	2	MES	90	5	PBS	0	132.4	-13.9
F26	49.75	0	38.3	9.95	1	0	0	0.5	0	0	0	0	0.5	0	2	MES	90	5	PBS	0	139.8	-13.1
F27	49.75	0	38.3	9.95	1	0	0	0.5	0	0	0	0	0.5	0	2	MES	90	5	PBS	15.3	173	-15.9
F28	50.25	0	38.7	10.05	0	0	0	0.5	0	0	0	0	0.5	0	2	MES	90	5	PBS	0	240.8	Missing
F29	50.25	0	38.7	10.05	0	0	0	0.5	0	0	0	0	0.5	0	2	MES	90	5	PBS	5.1	251.7	-17.7
F30	48.23	0	37.13	9.65	0	4	0	0.5	0	0	0	0	0.5	0	2	MES	90	5	PBS	0	89.9	-12.5
F31	48.23	0	37.13	9.65	0	4	0	0.5	0	0	0	0	0.5	0	2	MES	90	5	PBS	4	104.1	-18.6
F32	48.23	0	37.13	9.65	3.38	0	0	1.13	0	0	0	0	0.5	0	2	MES	90	5	PBS	0	110.7	-1.7
F33	48.23	0	37.13	9.65	3.38	0	0	1.13	0	0	0	0	0.5	0	2	MES	90	5	PBS	2.4	131.8	-12.5
F34	48.23	0	37.13	9.65	3.38	0	0	1.13	0	0	0	0	0.5	0	2	MES	90	5	PBS	18.5	128.7	-26.6
F35	49.75	0	38.3	9.95	1.13	0	0	0.38	0	0	0	0	0.5	0	2	MES	90	5	PBS	24	154.2	-1.4
F36	49.75	0	38.3	9.95	1.13	0	0	0.38	0	0	0	0	0.5	0	2	MES	90	5	PBS	0	135.1	-8.8
F37	49.75	0	38.3	9.95	1	0	0	0.5	0	0	0	0	0.5	0	2	MES	90	5	PBS	0	127.1	-25.0
F38	49.75	0	38.3	9.95	1	0	0	0.5	0	0	0	0	0.5	0	2	MES	90	5	PBS	9.7	116.8	-18.5
F39	49.75	0	38.3	9.95	1	0	0	0.5	0	0	0	0	0.5	0	2	MES	90	5	PBS	9.7	125.2	-23.7
F40	49.75	0	38.3	9.95	1	0	0	0.5	0	0	0	0	0.5	0	2	MES	90	5	PBS	0	75.5	-19.1
F41	49.75	0	38.3	9.95	1	0	0	0.5	0	0	0	0	0.5	0	2	MES	90	5	PBS	36.3	180.4	-29.6
F42	0	49.75	38.3	9.95	0	1	0	0	0.5	0	0	0	0.5	0	2	MES	90	5	PBS	0	102.2	22.9
F43	44.68	0	34.39	8.94	1	0	0	0.5	0	0	10	0	0.5	0	2	MES	90	5	PBS	0	82.8	14.3
F44	44.68	0	34.39	8.94	0	1	0	0.5	0	0	10	0	0.5	0	2	MES	90	5	PBS	0	91.2	17.9
F45	44.68	0	34.39	8.94	0	1	0	0	0.5	0	10	0	0.5	0	2	MES	90	5	PBS	0	97.5	29.7
F46	0	44.68	34.39	8.94	0	1	0	0	0.5	0	10	0	0.5	0	2	MES	90	5	PBS	0	128.9	38.0
F47	0	44.68	34.39	8.94	0	1	0	0.5	0	0	10	0	0.5	0	2	MES	90	5	PBS	0	95.5	27.4
F48	0	44.68	34.39	8.94	0	1	0	0.5	0	0	10	0	0.5	0	2	MES	90	5	PBS	93	144.5	17.5
F49	49.75	0	38.3	9.95	1	0	0	0.5	0	0	0	0	0.5	0	2	MES	90	5	PBS	0	98.1	-7.1
F50	0	49.75	38.3	9.95	0	1	0	0.5	0	0	0	0	0.5	0	2	MES	90	5	PBS	0	101.7	8.6
F51	0	49.75	38.3	9.95	0	1	0	0	0.5	0	0	0	0.5	0	2	MES	90	5	PBS	0	114.8	26.7
F52	0	50	38.5	10	0	1	0	0.5	0	0	0	0	0	0	0.5	Citrate + s	90	5	PBS	0	92.7	-11.9
F53	0	50	38.5	10	0	1	0	0	0.5	0	0	0	0	0	0.5	Citrate + s	90	5	PBS	0	102.4	9.0
F54	50	0	38.5	10	1	0	0	0.5	0	0	0	0	0	0	0.5	Citrate + s	90	5	PBS	0	126.1	-6.5
F55	44.93	0	34.59	8.99	1	0	0	0.5	0	0	10	0	0	0	0.5	Citrate + s	90	5	PBS	0	120	4.2
F56	34.78	0	26.78	6.96	1	0	0	0.5	0	0	30	0	0	0	0.5	Citrate + s	90	5	PBS	0	159.3	-3.0
F57	24.63	0	18.96	4.93	1	0	0	0.5	0	0	50	0	0	0	0.5	Citrate + s	90	5	PBS	0	121	-0.1
F58	14.48	0	11.15	2.9	1	0	0	0.5	0	0	70	0	0	0	0.5	Citrate + s	90	5	PBS	0	127.8	-0.4
F59	44.93	0	34.59	8.99	0	1	0	0.5	0	0	10	0	0	0	0.5	Citrate + s	90	5	PBS	0	121	9.1
F60	44.93	0	34.59	8.99	1	0	0	0	0.5	0	10	0	0	0	0.5	Citrate + s	90	5	PBS	0	172.4	30.7
F61	0	44.93	34.59	8.99	1	0	0	0.5	0	0	10	0	0	0	0.5	Citrate + s	90	5	PBS	0	135.5	-8.4
F62	0	44.93	34.59	8.99	0	1	0	0	0.5	0	10	0	0	0	0.5	Citrate + s	90	5	PBS	0	102.5	20.0
F63	0	44.93	34.59	8.99	0	1	0	0.5	0	0	10	0	0	0	0.5	Citrate + s	90	5	PBS	0	110.2	-31.3
F64	0	44.93	34.59	8.99	0	1	0	0.5	0	0	10	0	0	0	0.5	Citrate + s	90	5	PBS	0	147.7	-10.9
F65	0	44.93	34.59	8.99	0	1	0	0.5	0	0	10	0	0	0	0.5	Citrate + s	90	5	PBS	0	103.3	-10.8
F66	44.93	0	34.59	8.99	1	0	0	0.5	0	0	10	0	0	0	0.5	Citrate + s	90	5	PBS	0	142.9	16.5
F67	44.93	0	34.59	8.99	0	1	0	0.5	0	0	10	0	0	0	0.5	Citrate + s	90	5	PBS	0	140.2	19.9
F68	44.93	0	34.59	8.99	0	1	0	0	0.5	0	10	0	0	0	0.5	Citrate + s	90	5	PBS	0	162.7	34.6

A	B	C	D	E	F	G	H	I	J	K	L	M	N	O	P	Q	R	S	T	U	V	W
	Inputs																				Outputs	
	Ionizable lipids				non-functionalized PEG			Functionalized-PEG			SORT lipid		Flourescent Lipic									
M.W	642	648	387	790	2780	2801	2509	2780	2790	2940	698	722.5	1300	1332								
LNPs ID	D-lin-MC3	DODAP	Cholesterol	DSPC	DSPE-PEG	DOPE-PEG	DMG-PEG	DSPE-PEG-COOH	DSPE-PEG-NH2	DSPE-PEG-Malimid	DOTAP	18:1 PA	DOPE-Rhodamine	DSPE-cv7	total lipid conc (mg/ml)	Buffer synthesis	total flow rate	flow rate ratio	Buffer disperesion	n of abs per one LNP	Size	zeta potential
F69	0	44.93	34.59	8.99	0	1	0	0.5	0	0	10	0	0	0	0.5	Citrate + s	90	5	PBS	0	103.5	-11.0
F70	0	44.93	34.59	8.99	0	1	0	0.5	0	0	10	0	0	0	0.5	Citrate + s	90	5	PBS		121.8	-14.8
F71	49.75	0	38.3	9.95	0	1.125	0	0	0.375	0	0	0	0.5	0	2	MES	90	5	PBS	0	159.7	0.8
F72	49.75	0	38.3	9.95	1.125	0	0	0	0.375	0	0	0	0.5	0	2	MES	90	5	PBS	0	112.9	-4.7
F73	24.88	0	19.2	4.98	0	1.125	0	0	0.375	0	49	0	0.5	0	2	MES	90	5	PBS	0	135.4	30.6
F74	25.0	0	19.3	5	1	0	0	0.5	0	0	49.25	0	0	0	0.5	Citrate + s	90	5	PBS	0	118.8	8.0
F75	24.6	0	19.0	4.93	0	0	1.5	0	0	0	50	0	0	0	0.5	Citrate + s	90	5	PBS	0	167	-1.7
F76	25.0	0	19.3	5	0	0	0.75	0	0	0	50	0	0	0	0.5	Citrate + s	90	5	PBS	0	174.3	13.0
F77	0	49.75	38.3	9.95	0	0.995	0	0	0.5	0	0	0	0	0.5	2	Acetate	90	4	PBS	0	96	18.7
F78	49	0	37.7	9.8	2.49	0	0	0	0.5	0	0	0	0	0.5	2	Acetate	90	4	PBS	0	68.3	-9.0
F79	49	0	37.7	9.8	0	2.49	0	0	0.5	0	0	0	0	0.5	2	Acetate	90	4	PBS	0	82.5	-4.5
F80	0	49	37.7	9.8	2.49	0	0	0	0.5	0	0	0	0	0.5	2	Acetate	90	4	PBS	0	81.4	-3.5
F81	0	49	37.7	9.8	0	2.49	0	0	0.5	0	0	0	0	0.5	2	Acetate	90	4	PBS	0	76.1	12.5
F82	0	24.75	19.1	4.95	0	0.25	0	0	0.5	0	50	0	0	0.5	2	Acetate	90	4	PBS	0	104.6	24.3
F83	24.35	0	18.7	4.87	1	0	0	0	0.5	0	50	0	0	0.5	2	Acetate	90	4	PBS	0	128.2	26.3
F84	24.35	0	18.7	4.87	0	1	0	0	0.5	0	50	0	0	0.5	2	Acetate	90	4	PBS	0	144.9	34.2
F85	0	24.35	18.7	4.87	1	0	0	0	0.5	0	50	0	0	0.5	2	Acetate	90	4	PBS	0	124.6	30.6
F86	0	24.35	18.7	4.87	0	1	0	0	0.5	0	50	0	0	0.5	2	Acetate	90	4	PBS	0	130.8	46.0
F87	49.75	0	38.3	9.95	0	0.995	0	0	0.5	0	0	0	0	0.5	2	Acetate	90	4	PBS	0	102.7	2.8
F88	24.75	0	19.1	4.95	0	0.25	0	0	0.5	0	50	0	0	0.5	2	Acetate	90	4	PBS	0	187.7	31.8
F89	24.88	0	19.2	4.98	0	0	1.5	0	0	0	49	0	0	0.5	2	MES	90	5	PBS	0	93	16.0
F90	24.88	0	19.2	4.98	1.5	0	0	0	0	0	49	0	0	0.5	2	MES	90	5	PBS	0	108	13.0
F91		24.88	19.2	4.98	0	0	1.5	0	0	0	49	0	0	0.5	2	MES	90	5	PBS	0	91	17.0
F92		24.88	19.2	4.98	1.5	0	0	0	0	0	49	0	0	0.5	2	MES	90	5	PBS	0	105	15.0
F93	49	0	37.7	9.8	0	0	0	3	0	0	0	0	0	0.5	2	MES	90	5	MES	0	75	-34.5
F94	49	0	37.7	9.8	0	0	0	3	0	0	0	0	0	0.5	2	MES	90	5	MES	0	87.5	-26.7
F95	49	0	37.7	9.8	3	0	0	0	0	0	0	0	0	0.5	2	MES	90	5	MES	0	74.7	7.0
F96	49	0	37.7	9.8	2.5	0	0	0.5	0	0	0	0	0.5	0	2	Acetate	90	4	PBS	0	87.4	-11.2
F97	48.76	0	37.5	9.75	2.49	0	0	0.50	0	0	0	0	1	0	2	Acetate	90	4	PBS	0	117.9	-14.0
F98	49.75	0	38.3	9.95	0	1	0	0.5	0	0	0	0	0	0.5	2	MES	90	5	MES	0	165	-6.3
F99	49	0	37.7	9.8	0	0	0	3	0	0	0	0	0	0.5	2	MES	90	5	MES	0	82.3	-17.9
F100	48.23	0	37.13	9.65	3.38	0	0	1.13	0	0	0	0	0.5	0	2	MES	90	5	MES	0	72.5	
F101	48.23	0	37.13	9.65	3.38	0	0	1.13	0	0	0	0	0.5	0	2	MES	90	5	PBS	0	98.9	-12.5
F102	48.23	0	37.13	9.65	3.38	0	0	1.13	0	0	0	0	0.5	0	2	MES	90	5	PBS	37	136.9	-25.1

Appendix 3: LNPs Placental Transport Dataset

A	B	C	D	E	F	G	H	I	J	K	L	M	N	O	P	Q	R	S	T	U	V	W
Input Featuers																			Outputs			
Cells Seeding density	Endothelial Cells	Syncytialization	FBS	Ionizable Lipid	Cationic molar %	Anionic molar %	PEG molar %	PEG Lipid Type	PEG end Group	Conj Linker	Ab Portion Pointing Outward	No. of Abs per LNP	D Between Abs	Mass of LNP per Cell	No. of LNPs per Cell	LNP Size	LNP Zeta Potential	LNPs pKa	**24 H Transport %**	**Average Permeability (cm/h)**	**T half (Hours)**	**K- values**
100000	0	0	1	0	0	0	1.5	0	-1	0	0	0	10000	0.65	333853	90	-14.4	6.26	32.4	0.00927	34.3	0.0625
100000	0	0	1	0	50	0	1.5	0	-1	0	0	0	10000	0.65	295381	118.3	10.83	11	31.5	0.00773	33.6	0.0700
100000	0	0	1	0	0	30	1.5	0	-1	0	0	0	10000	0.65	286241	106.6	-7.75	4.06	30.9	0.01088	36.6	0.0572
100000	0	0	1	1	0	0	1.5	0	-1	0	0	0	10000	0.65	363318	130	7.75	6.84	54.2	0.01765	19.6	0.0760
100000	0	0	1	0	0	0	4.5	1	-1	0	0	0	10000	0.65	311000	81	-19.58	5.94	18.4	0.00554	48.5	0.0600
100000	0	0	1	0	0	0	4.5	0	-1	0	0	0	10000	0.65	254647	79.5	-16.66	6.11	10.5	0.00267	61.2	0.0556
100000	0	0	1	0	0	0	1.5	0	-1	0	0	0	10000	0.65	467338	107.2	-21.21	6.13	15.4	0.00238	44.1	0.0825
100000	0	0	0	0	0	0	1.5	0	-1	0	0	0	10000	0.65	467338	107.2	-21.21	6.13	21.8	0.00283	36.7	0.0986
100000	0	0	0	0	0	0	1.5	0	-1	-1	-1	118.9	33.9	0.65	467338	117.6	-26.46	6.22	30.6	0.00550		
100000	0	0	0	0	0	0	1.5	0	-1	0	0	0	10000	0.21	105305	92.9	-20.9		30.0	0.01101	35.1	0.0662
100000	0	0	0	0	0	0	1.5	0	-1	-1	-1	158.7	42.7	0.21	105305	171	-38.9		23.5	0.00423	33.8	0.1224
100000	0	0	1	0	0	0	1.5	0	-1	0	0	0	10000	0.21	105305	92.9	-20.9		27.9	0.00923	36.5	0.0684
100000	0	0	1	0	0	0	1.5	0	-1	-1	-1	158.7	42.7	0.21	105305	171	-38.9		29.2	0.00548	33.1	0.0952
100000	0	0	1	0	0	0	1.5	0	1	0	0	0	10000	0.65	529412	109.3	6.56	6.25	74.4	0.01017	12.7	0.1120
100000	0	0	1	0	0	0	1.5	0	1	-1	1	31.2	105.7	0.65	529412	187.8	2.95		56.3	0.00847	16.3	0.0820
100000	0	0	1	0	0	0	1.5	0	-1	0	0	0	10000	0.65	609490	152.1	-13.1		49.1	0.01102	23.6	0.0732
100000	0	0	1	0	0	0	1.5	0	-1	-1	-1	20.7	103.8	0.65	609490	150.2	-22.46		87.5	0.01225	6.6	0.2453
100000	0	0	1	0	0	0	1.5	0	0	1	-1	46.3	86	0.65	597769	186.1	-15.86		69.3	0.00976	12.6	0.1102
100000	0	0	1	0	0	0	1.5	0	-1	0	0	0	10000	0.65	778097	129.6	-12.65		47.2	0.00558	24.7	0.0946
100000	0	0	1	0	0	0	1.5	0	-1	-1	0	0	10000	0.65	778097	132.4	-13.9		42.1	0.00519	27.0	0.0840
500000	0	0	1	0	0	0	1.5	0	-1	0	0	0	10000	0.13	198795	139.8	-13.12		15.8	0.00104		
500000	0	0	1	0	0	0	1.5	0	-1	-1	-1	15.3	139	0.13	198795	173	-15.87		9.2	0.00061		
500000	0	0	1	0	0	0	0.5	0	-1	-1	-1	5.1	350	0.13	121596	251.7	-17.74		1.0	0.00012	38.2	0.3281
500000	0	0	1	0	0	0	4.5	1	-1	0	0	0	10000	0.13	162349	89.9	-12.51		3.6	0.00055	46.9	0.1441
500000	0	0	1	0	0	0	4.5	1	-1	-1	-1	4	163.6	0.13	162349	104.1	-18.61		7.6	0.00132	42.4	0.1370
500000	0	0	1	0	0	0	4.5	0	-1	0	0	0	10000	0.13	92771	110.7	-1.73		4.3	0.00063	75.6	0.0626
500000	0	0	1	0	0	0	4.5	0	-1	-1	-1	2.4	267.4	0.13	92771	131.8	-12.49		0.9	0.00063	63.6	0.1106
500000	0	0	1	0	0	0	4.5	0	-1	-1	-1	18.5	94	0.13	92771	128.7	-26.6		1.0	0.00060	67.1	0.0928
500000	0	0	1	0	0	0	1.5	0	-1	-1	-1	24	98.9	0.13	155619	154.2	-1.4		48.7	0.01743	23.1	0.0714
500000	0	0	1	0	0	0	1.5	0	-1	0	0	0	10000	0.13	155619	135.1	-8.78		35.7	0.01548	29.8	0.0687
100000	0	0	1	0	0	0	1.5	0	-1	0	0	0	10000	0.65	592059	127.1	-25	6.14	20.0	0.00151		
100000	0	0	1	0	0	0	1.5	0	-1	-1	-1	9.7	117.9	0.65	592059	116.8	-18.5	6.06	23.6	0.00191	30.9	0.1723
100000	0	0	1	0	0	0	1.5	0	-1	-1	-1	9.7	126.3	0.65	592059	125.2	-23.7	6.15	21.7	0.00177	30.8	0.1904
100000	1	0	1	0	0	0	1.5	0	-1	0	0	0	10000	0.65	947443	75.5	-19.06	6.39	0.5	0.00004		
100000	1	0	1	0	0	0	1.5	0	-1	-1	-1	36.3	94.1	0.65	947443	180.4	-29.6	6.47	1.2	0.00010		
100000	1	0	1	1	0	0	1.5	1	1	0	0	0	10000	0.65	1068257	102.2	22.9	**7.7**	6.5	0.00064	48.5	0.1066
100000	1	1	1	0	0	0	1.5	0	-1	0	0	0	10000	0.65	947443	75.5	-19.06	**6.39**	17.3	0.00152	33.0	0.1716
100000	1	1	1	0	0	0	1.5	0	-1	-1	-1	36.3	94.1	0.65	947443	180.4	-29.6	**6.47**	21.7	0.00176	32.9	0.1409
100000	1	1	1	1	0	0	1.5	1	1	0	0	0	10000	0.65	1068257	102.2	22.9	**7.7**	39.4	0.00348	25.6	0.1071
100000	0	0	1	0	0	0	1.5	0	-1	0	0	0	10000	0.65	947443	75.5	-19.06	**6.39**	3.3	0.00032	57.2	0.1017
100000	0	0	1	0	0	0	1.5	0	-1	-1	-1	36.3	94.1	0.65	947443	180.4	-29.6	**6.47**	8.3	0.00101	48.5	0.0978
100000	0	0	1	1	0	0	1.5	1	1	0	0	0	10000	0.65	1068257	102.2	22.9	7.7	53.2	0.00507	19.7	0.1097
100000	0	0	1	0	10	0	1.5	0	-1	0	0	0	10000	0.15	337059	82.8	14.25		12.0	0.00277	57.9	0.0519
100000	0	0	1	0	10	0	1.5	1	-1	0	0	0	10000	0.15	270875	91.2	17.9		5.9	0.00071	58.4	0.0792
100000	0	0	1	0	10	0	1.5	1	1	0	0	0	10000	0.15	229933	97.5	29.7		19.2	0.00184	41.2	0.0798
100000	0	0	1	1	10	0	1.5	1	1	0	0	0	10000	0.15	198426	128.9	38		13.5	0.00132	44.1	0.0903
100000	0	0	1	1	10	0	1.5	1	-1	0	0	0	10000	0.15	175245	95.5	27.4		24.1	0.00257	37.1	0.0825
100000	0	0	1	1	10	0	1.5	1	-1	-1	-1	93	47	0.15	175245	144.5	17.5		35.7	0.00526	27.5	0.0712
Validation Formulations																						
100000	0	0	1	0	0	0	1.5	0	-1	0	0	0	10000	0.15	152941	98.1	-7.1		8.5	0.00184	68.5	0.0455
100000	0	0	1	1	0	0	1.5	1	-1	0	0	0	10000	0.65	550000	101.7	8.56		19.5	0.00233		
100000	0	0	1	1	0	0	1.5	1	1	0	0	0	10000	0.65	530790	114.8	26.7		61.4	0.00515	20.4	0.1499

Appendix 4: Chapter 3 Supplementary Tables and Figures

1. Microfluidic Synthesis Optimization

Total Flow Rate (TFR) and Flow Rate Ratio (FRR) were optimized to produce liposome sizes of the desired size range, while maintaining a low (<0.2) polydispersity index (PDI). The TFR and FRR of liposome formation with their corresponding size and PDI are reported in the tables below.

Supplementary Table 3*: Flow Rate Ratio and Total Flow Rate for Preliminary Synthesis Conditions*

Run	**Flow Rate Ratio**	**Total Flow Rate (µL/min)**	**Diameter (nm)**	**PDI**	**Zeta Potential (mV)**
1	16:1	30	44.3 ± 0.3*	0.197 ± 0.013	-4.76 ± 1.09
2	16:1	40	37.0 ± 0.4	0.123 ± 0.022	5.32 ± 3.65
3	16:1	50	40.3 ± 0.3	0.155 ± 0.025	6.42 ± 5.77
4	12:1	30	41.7 ± 0.9	0.143 ± 0.022	-6.62 ± 4.12
5	12:1	40	38.3 ± 0.4	O.143 ± 0.024	1.64 ± 1.31
6	12:1	50	41.0 ± 0.4	0.098 ± 0.030	-11.01 ± 2.57

*Mean ± Standard Error

2. Measuring CSA-bp Conjugation Efficiency

BCA Assay sensitivity to CSA peptide was measured by measuring different concentrations of CSA and comparing their measured value to the known value. These results are shown in Supplementary Figure 9 below. Assay sensitivity was found to be 64% and follows the equation:

(CSA Concentration measured by assay) = 0.6406mL*(the actual value of concentration)-3.5103

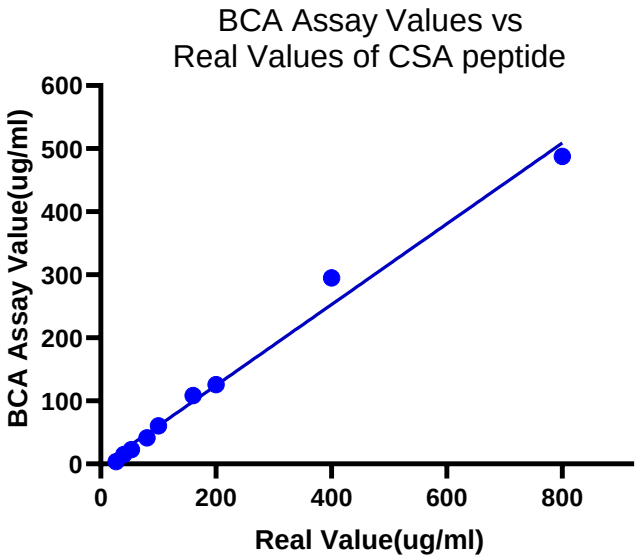

Figure S9: *BCA assay sensitivity to CSA. Known concentrations of CSA peptide were measured by BCA assay and the measured values(y-axis) are plotted against the Real Value(x-axis).*

3. Cell Viability using Calcein-AM Cell Permeant Dye

Cell viability was measured using calcein-AM cell permeant dye. Briefly, BeWo cells were seeded into a 96 well plate at a density of 50,000 cells per well. Once confluent, cells were exposed to either of unconjugated control liposomes or CSA-conjugated liposomes at a series of concentrations of $5x10^6$ –$5x10^{10}$ particle/mL, equivalent to 10 – 100,000 liposomes/cell, for 15 hours. Negative control conditions (100 % cell viability) were allowed to incubate with only cell media, free of any liposomes. Positive controls (0 % cell viability) were exposed to triton X-100 for 30 minutes. Following exposure time, cells were washed with DPBS to remove any unbound liposomes before cells incubation with 2 uM of the Calcein-AM dye for 30 minutes. Fluorescence was measured using a BioTek Synergy H1 Plate Reader (Agilent Technologies, Canada) at excitation and emission wavelengths of 494 and 517 nm, respectively. Percentage cell viability was calculated based on five replicates.

Supplementary Figure 3 shows the viability of BeWo b30 cells after incubation with unconjugated as well as CSA-conjugated liposomes at a series of concentrations within a range of $5x10^6$ to $5x10^{10}$ particles/mL, as determined by nanoparticle tracking analysis. These concentrations were equivalent to liposome: cell ratios ranging from 10 to 100,000 particles/cell. No significant difference ($p > 0.05$) in cell viability was observed for unconjugated liposomes or CSA-conjugated liposomes compared to non-treated control cells, indicating the safety of CSA-conjugated liposomes on the placental cells.

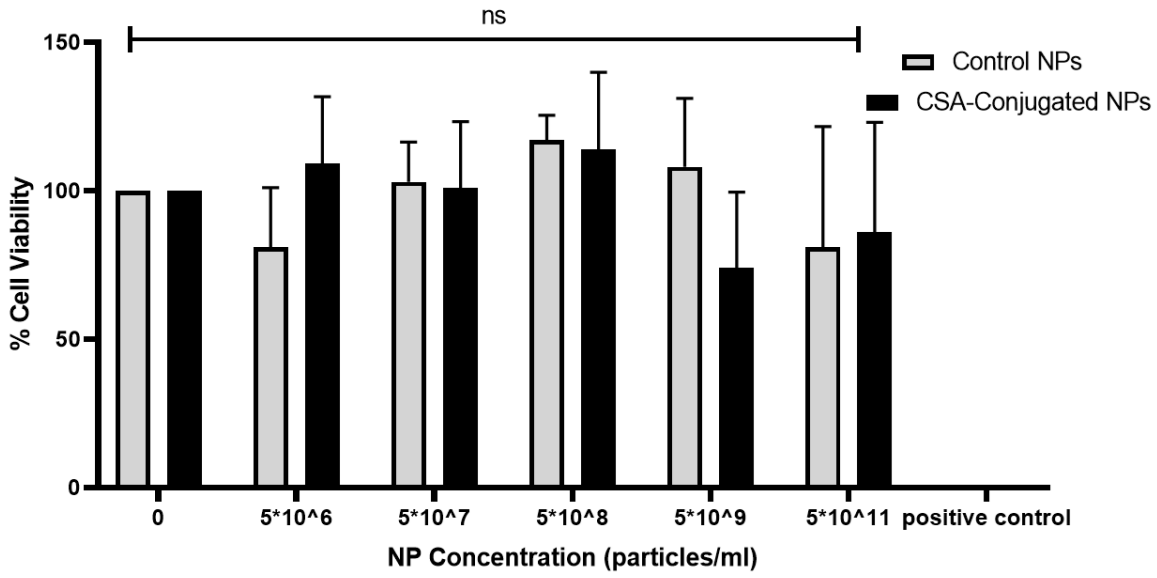

Figure S10: *Viability of BeWo b30 cells following cell exposure to control (unconjugated) and CSA-conjugated liposomes at different exposure concentrations for 15h, as determined using calcein-AM cell permeant dye. Triton X-100 was used as positive control. Data is presented as mean ± SD calculated from three experimental replicates; ns denotes non-significant differences.*

References:

1. Palanki R, Peranteau WH, Mitchell MJ. Delivery technologies for in utero gene therapy. *Adv Drug Deliv Rev*. Feb 2021;169:51-62. doi:10.1016/j.addr.2020.11.002
2. Yu L, Hernan RR, Wynn J, Chung WK. The influence of genetics in congenital diaphragmatic hernia. *Semin Perinatol*. Feb 2020;44(1):151169. doi:10.1053/j.semperi.2019.07.008
3. Lord J, McMullan DJ, Eberhardt RY, et al. Prenatal exome sequencing analysis in fetal structural anomalies detected by ultrasonography (PAGE): a cohort study. *Lancet*. Feb 23 2019;393(10173):747-757. doi:10.1016/S0140-6736(18)31940-8
4. Palanki R, Bose SK, Dave A, et al. Ionizable Lipid Nanoparticles for Therapeutic Base Editing of Congenital Brain Disease. *ACS Nano*. Jul 25 2023;17(14):13594-13610. doi:10.1021/acsnano.3c02268
5. Witt R, MacKenzie TC, Peranteau WH. Fetal stem cell and gene therapy. *Semin Fetal Neonatal Med*. Dec 2017;22(6):410-414. doi:10.1016/j.siny.2017.05.003
6. Shepherd SJ, Han X, Mukalel AJ, et al. Throughput-scalable manufacturing of SARS-CoV-2 mRNA lipid nanoparticle vaccines. *Proc Natl Acad Sci U S A*. Aug 15 2023;120(33):e2303567120. doi:10.1073/pnas.2303567120
7. Lind NA, Rael VE, Pestal K, Liu B, Barton GM. Regulation of the nucleic acid-sensing Toll-like receptors. *Nature Reviews Immunology*. 2022/04/01 2022;22(4):224-235. doi:10.1038/s41577-021-00577-0
8. Kulkarni JA, Witzigmann D, Thomson SB, et al. The current landscape of nucleic acid therapeutics. *Nature Nanotechnology*. 2021/06/01 2021;16(6):630-643. doi:10.1038/s41565-021-00898-0
9. Robbins PD, Ghivizzani SC. Viral Vectors for Gene Therapy. *Pharmacology & Therapeutics*. 1998/10/01/ 1998;80(1):35-47. doi:https://doi.org/10.1016/S0163-7258(98)00020-5
10. Yin H, Kanasty RL, Eltoukhy AA, Vegas AJ, Dorkin JR, Anderson DG. Non-viral vectors for gene-based therapy. *Nat Rev Genet*. Aug 2014;15(8):541-55. doi:10.1038/nrg3763
11. Ullrich SJ, Yung NK, Bauer-Pisani TJ, et al. delivery of miRNA induces epigenetic alterations and corrects pulmonary pathology in congenital diaphragmatic hernia. *Mol Ther Nucleic Acids*. Jun 13 2023;32:594-602. doi:10.1016/j.omtn.2023.04.018
12. Riley RS, Kashyap MV, Billingsley MM, et al. Ionizable lipid nanoparticles for in utero mRNA delivery. *Sci Adv*. Jan 2021;7(3)doi:10.1126/sciadv.aba1028
13. Swingle KL, Billingsley MM, Bose SK, et al. Amniotic fluid stabilized lipid nanoparticles for in utero intra-amniotic mRNA delivery. *J Control Release*. Jan 2022;341:616-633. doi:10.1016/j.jconrel.2021.10.031
14. Samaridou E, Heyes J, Lutwyche P. Lipid nanoparticles for nucleic acid delivery: Current perspectives. *Adv Drug Deliv Rev*. 2020;154-155:37-63. doi:10.1016/j.addr.2020.06.002
15. Mullard A. FDA approves mRNA-based RSV vaccine. *Nat Rev Drug Discov*. Jul 2024;23(7):487. doi:10.1038/d41573-024-00095-3
16. Verbeke R, Lentacker I, De Smedt SC, Dewitte H. The dawn of mRNA vaccines: The COVID-19 case. *J Control Release*. May 10 2021;333:511-520. doi:10.1016/j.jconrel.2021.03.043
17. Ali MS, Hooshmand N, El-Sayed M, Labouta HI. Microfluidics for Development of Lipid Nanoparticles: Paving the Way for Nucleic Acids to the Clinic. *ACS Appl Bio Mater*. Sep 18 2023;6(9):3566-3576. doi:10.1021/acsabm.1c00732
18. Chen W, Duša F, Witos J, Ruokonen SK, Wiedmer SK. Determination of the Main Phase Transition Temperature of Phospholipids by Nanoplasmonic Sensing. *Sci Rep*. Oct 04 2018;8(1):14815. doi:10.1038/s41598-018-33107-5

19. Wagner JP, Schreiner PR. London dispersion in molecular chemistry--reconsidering steric effects. *Angew Chem Int Ed Engl*. Oct 12 2015;54(42):12274-96. doi:10.1002/anie.201503476
20. Ni R, Feng R, Chau Y. Synthetic Approaches for Nucleic Acid Delivery: Choosing the Right Carriers. *Life (Basel)*. Jul 09 2019;9(3)doi:10.3390/life9030059
21. Sabnis S, Kumarasinghe ES, Salerno T, et al. A Novel Amino Lipid Series for mRNA Delivery: Improved Endosomal Escape and Sustained Pharmacology and Safety in Non-human Primates. *Mol Ther*. Jun 06 2018;26(6):1509-1519. doi:10.1016/j.ymthe.2018.03.010
22. Gruner SM, Cullis PR, Hope MJ, Tilcock CP. Lipid polymorphism: the molecular basis of nonbilayer phases. *Annu Rev Biophys Biophys Chem*. 1985;14:211-38. doi:10.1146/annurev.bb.14.060185.001235
23. Hafez IM, Cullis PR. Roles of lipid polymorphism in intracellular delivery. *Adv Drug Deliv Rev*. Apr 25 2001;47(2-3):139-48. doi:10.1016/s0169-409x(01)00103-x
24. Spadea A, Jackman M, Cui L, et al. Nucleic Acid-Loaded Lipid Nanoparticle Interactions with Model Endosomal Membranes. *ACS Appl Mater Interfaces*. Jul 06 2022;14(26):30371-30384. doi:10.1021/acsami.2c06065
25. Schlich M, Palomba R, Costabile G, et al. Cytosolic delivery of nucleic acids: The case of ionizable lipid nanoparticles. *Bioeng Transl Med*. May 2021;6(2):e10213. doi:10.1002/btm2.10213
26. Patel P, Ibrahim NM, Cheng K. The Importance of Apparent pKa in the Development of Nanoparticles Encapsulating siRNA and mRNA. *Trends Pharmacol Sci*. Jun 2021;42(6):448-460. doi:10.1016/j.tips.2021.03.002
27. Freeman EC, Weiland LM, Meng WS. Modeling the proton sponge hypothesis: examining proton sponge effectiveness for enhancing intracellular gene delivery through multiscale modeling. *J Biomater Sci Polym Ed*. 2013;24(4):398-416. doi:10.1080/09205063.2012.690282
28. Han X, Zhang H, Butowska K, et al. An ionizable lipid toolbox for RNA delivery. *Nat Commun*. Dec 13 2021;12(1):7233. doi:10.1038/s41467-021-27493-0
29. Mrksich K, Padilla MS, Joseph RA, et al. Influence of ionizable lipid tail length on lipid nanoparticle delivery of mRNA of varying length. *J Biomed Mater Res A*. Mar 15 2024;doi:10.1002/jbm.a.37705
30. Han EL, Padilla MS, Palanki R, et al. Predictive High-Throughput Platform for Dual Screening of mRNA Lipid Nanoparticle Blood-Brain Barrier Transfection and Crossing. *Nano Lett*. Feb 07 2024;24(5):1477-1486. doi:10.1021/acs.nanolett.3c03509
31. Safford HC, Swingle KL, Geisler HC, et al. Orthogonal Design of Experiments for Engineering of Lipid Nanoparticles for mRNA Delivery to the Placenta. *Small*. Aug 03 2023:e2303568. doi:10.1002/smll.202303568
32. Leung AK, Tam YY, Cullis PR. Lipid nanoparticles for short interfering RNA delivery. *Adv Genet*. 2014;88:71-110. doi:10.1016/B978-0-12-800148-6.00004-3
33. Ge X, Chen L, Zhao B, Yuan W. Rationale and Application of PEGylated Lipid-Based System for Advanced Target Delivery of siRNA. *Front Pharmacol*. 2020;11:598175. doi:10.3389/fphar.2020.598175
34. D'Souza A, Shegokar R. 16 - Polymer: Lipid Hybrid Nanostructures in Cancer Drug Delivery: Successes and Limitations. In: Holban AM, Grumezescu AM, eds. *Nanoarchitectonics for Smart Delivery and Drug Targeting*. William Andrew Publishing; 2016:431-463.
35. Zhu X, Tao W, Liu D, et al. Surface De-PEGylation Controls Nanoparticle-Mediated siRNA Delivery. *Theranostics*. 2017;7(7):1990-2002. doi:10.7150/thno.18136
36. Kulkarni JA, Witzigmann D, Leung J, Tam YYC, Cullis PR. On the role of helper lipids in lipid nanoparticle formulations of siRNA. *Nanoscale*. Nov 21 2019;11(45):21733-21739. doi:10.1039/c9nr09347h

37. Zhang R, El-Mayta R, Murdoch TJ, et al. Helper lipid structure influences protein adsorption and delivery of lipid nanoparticles to spleen and liver. *Biomater Sci*. Feb 21 2021;9(4):1449-1463. doi:10.1039/d0bm01609h
38. Hatit MZC, Dobrowolski CN, Lokugamage MP, et al. Nanoparticle stereochemistry-dependent endocytic processing improves in vivo mRNA delivery. *Nat Chem*. Apr 2023;15(4):508-515. doi:10.1038/s41557-023-01138-9
39. Dilliard SA, Cheng Q, Siegwart DJ. On the mechanism of tissue-specific mRNA delivery by selective organ targeting nanoparticles. *Proc Natl Acad Sci U S A*. Dec 28 2021;118(52)doi:10.1073/pnas.2109256118
40. Cheng Q, Wei T, Farbiak L, Johnson LT, Dilliard SA, Siegwart DJ. Selective organ targeting (SORT) nanoparticles for tissue-specific mRNA delivery and CRISPR-Cas gene editing. *Nat Nanotechnol*. Apr 2020;15(4):313-320. doi:10.1038/s41565-020-0669-6
41. Melamed JR, Yerneni SS, Arral ML, et al. Ionizable lipid nanoparticles deliver mRNA to pancreatic β cells via macrophage-mediated gene transfer. *Sci Adv*. Jan 27 2023;9(4):eade1444. doi:10.1126/sciadv.ade1444
42. Wang X, Liu S, Sun Y, et al. Preparation of selective organ-targeting (SORT) lipid nanoparticles (LNPs) using multiple technical methods for tissue-specific mRNA delivery. *Nat Protoc*. Jan 2023;18(1):265-291. doi:10.1038/s41596-022-00755-x
43. Kularatne RN, Crist RM, Stern ST. The Future of Tissue-Targeted Lipid Nanoparticle-Mediated Nucleic Acid Delivery. *Pharmaceuticals (Basel)*. Jul 20 2022;15(7)doi:10.3390/ph15070897
44. Wheeler JJ, Palmer L, Ossanlou M, et al. Stabilized plasmid-lipid particles: construction and characterization. *Gene Ther*. Feb 1999;6(2):271-81. doi:10.1038/sj.gt.3300821
45. Ali MS, Hooshmand N, El-Sayed M, Labouta HI. Microfluidics for Development of Lipid Nanoparticles: Paving the Way for Nucleic Acids to the Clinic. *ACS Applied Bio Materials*. 2021/09/08 2021;doi:10.1021/acsabm.1c00732
46. Ma J, Lee SM, Yi C, Li CW. Controllable synthesis of functional nanoparticles by microfluidic platforms for biomedical applications - a review. *Lab Chip*. Jan 17 2017;17(2):209-226. doi:10.1039/c6lc01049k
47. Kimura N, Maeki M, Sato Y, et al. Development of the iLiNP Device: Fine Tuning the Lipid Nanoparticle Size within 10 nm for Drug Delivery. *ACS Omega*. May 31 2018;3(5):5044-5051. doi:10.1021/acsomega.8b00341
48. Zhang L, Chen Q, Ma Y, Sun J. Microfluidic Methods for Fabrication and Engineering of Nanoparticle Drug Delivery Systems. *ACS Appl Bio Mater*. Jan 21 2020;3(1):107-120. doi:10.1021/acsabm.9b00853
49. Kimura N, Maeki M, Tokeshi M. Microfabrication and microfluidic devices for drug delivery. 2019:123-136.
50. Kulkarni MB, Goel S. Microfluidic devices for synthesizing nanomaterials—a review. *Nano Express*. 2020/11/30 2020;1(3):032004. doi:10.1088/2632-959X/abcca6
51. Belliveau NM, Huft J, Lin PJ, et al. Microfluidic Synthesis of Highly Potent Limit-size Lipid Nanoparticles for In Vivo Delivery of siRNA. *Mol Ther Nucleic Acids*. Aug 14 2012;1(8):e37. doi:10.1038/mtna.2012.28
52. Feng Q, Zhang L, Liu C, et al. Microfluidic based high throughput synthesis of lipid-polymer hybrid nanoparticles with tunable diameters. *Biomicrofluidics*. Sep 2015;9(5):052604. doi:10.1063/1.4922957
53. Krzysztoń R, Salem B, Lee DJ, Schwake G, Wagner E, Rädler JO. Microfluidic self-assembly of folate-targeted monomolecular siRNA-lipid nanoparticles. *Nanoscale*. Jun 08 2017;9(22):7442-7453. doi:10.1039/c7nr01593c

54. Abdelkarim M, Perez-Davalos L, Abdelkader Y, Abostait A, Labouta HI. Critical design parameters to develop biomimetic organ-on-a-chip models for the evaluation of the safety and efficacy of nanoparticles. *Expert Opin Drug Deliv*. Jan 2023;20(1):13-30. doi:10.1080/17425247.2023.2152000
55. Whitesides GM. The origins and the future of microfluidics. *Nature*. 2006/07/01 2006;442(7101):368-373. doi:10.1038/nature05058
56. Wautelet M. Scaling laws in the macro-, micro- and nanoworlds. *European Journal of Physics*. 2001/10/10 2001;22(6):601-611. doi:10.1088/0143-0807/22/6/305
57. Di Carlo D. Inertial microfluidics. *Lab on a chip*. 2009;9(21):3038-3046. doi:10.1039/b912547g
58. Capretto L, Cheng W, Hill M, Zhang X. Micromixing Within Microfluidic Devices. In: Lin B, ed. *Microfluidics: Technologies and Applications*. Springer Berlin Heidelberg; 2011:27-68.
59. Joseph X, Akhil V, Arathi A, Mohanan PV. Comprehensive Development in Organ-On-A-Chip Technology. *Journal of Pharmaceutical Sciences*. 2022;111(1):18-31. doi:10.1016/j.xphs.2021.07.014
60. Ortseifen V, Viefhues M, Wobbe L, Grünberger A. Microfluidics for Biotechnology: Bridging Gaps to Foster Microfluidic Applications. Review. *Frontiers in Bioengineering and Biotechnology*. 2020-November-13 2020;8doi:10.3389/fbioe.2020.589074
61. Fede C, Albertin G, Petrelli L, et al. Influence of shear stress and size on viability of endothelial cells exposed to gold nanoparticles. *Journal of Nanoparticle Research*. 2017/09/11 2017;19(9):316. doi:10.1007/s11051-017-3993-5
62. Kim D, Lin Y-S, Haynes CL. On-Chip Evaluation of Shear Stress Effect on Cytotoxicity of Mesoporous Silica Nanoparticles. *Analytical Chemistry*. 2011/11/15 2011;83(22):8377-8382. doi:10.1021/ac202115a
63. Mahto SK, Yoon TH, Rhee SW. A new perspective on in vitro assessment method for evaluating quantum dot toxicity by using microfluidics technology. *Biomicrofluidics*. 2010;4(3):034111. doi:10.1063/1.3486610
64. Sambale F, Stahl F, Bahnemann D, Scheper T. In vitro toxicological nanoparticle studies under flow exposure. *Journal of Nanoparticle Research*. 2015/07/11 2015;17(7):298. doi:10.1007/s11051-015-3106-2
65. Samuel SP, Jain N, O'Dowd F, et al. Multifactorial determinants that govern nanoparticle uptake by human endothelial cells under flow. *Int J Nanomedicine*. 2012;7:2943-2956. doi:10.2147/IJN.S30624
66. Yang H, Zhao F, Li Y, et al. VCAM-1-targeted core/shell nanoparticles for selective adhesion and delivery to endothelial cells with lipopolysaccharide-induced inflammation under shear flow and cellular magnetic resonance imaging in vitro. *Int J Nanomedicine*. 2013;8:1897-1906. doi:10.2147/IJN.S44997
67. Pimenta J, Ribeiro R, Almeida R, Costa PF, da Silva MA, Pereira B. Organ-on-Chip Approaches for Intestinal 3D In Vitro Modeling. *Cellular and Molecular Gastroenterology and Hepatology*. 2022;13(2):351-367. doi:10.1016/j.jcmgh.2021.08.015
68. Gude NM, Roberts CT, Kalionis B, King RG. Growth and function of the normal human placenta. *Thromb Res*. 2004;114(5-6):397-407. doi:10.1016/j.thromres.2004.06.038
69. Abostait A, Tyrrell J, Abdelkarim M, et al. Placental Nanoparticle Uptake-On-a-Chip: The Impact of Trophoblast Syncytialization and Shear Stress. *Mol Pharm*. Nov 07 2022;19(11):3757-3769. doi:10.1021/acs.molpharmaceut.2c00216
70. Al-Enazy S, Ali S, Albekairi N, El-Tawil M, Rytting E. Placental control of drug delivery. *Adv Drug Deliv Rev*. Jul 01 2017;116:63-72. doi:10.1016/j.addr.2016.08.002

71. Roopenian DC, Akilesh S. FcRn: the neonatal Fc receptor comes of age. *Nat Rev Immunol*. Sep 2007;7(9):715-25. doi:10.1038/nri2155
72. Tse WH, Higgins S, Patel D, et al. The maternal-fetal transfer of passive immunity as a mechanism of transplacental nanoparticle drug delivery for prenatal therapies. *Biomater Sci*. Sep 13 2022;10(18):5243-5253. doi:10.1039/d2bm00293k
73. Figueroa-Espada CG, Hofbauer S, Mitchell MJ, Riley RS. Exploiting the placenta for nanoparticle-mediated drug delivery during pregnancy. *Adv Drug Deliv Rev*. 2020;160:244-261. doi:10.1016/j.addr.2020.09.006
74. Aengenheister L, Keevend K, Muoth C, et al. An advanced human in vitro co-culture model for translocation studies across the placental barrier. *Sci Rep*. Mar 29 2018;8(1):5388. doi:10.1038/s41598-018-23410-6
75. Yin F, Zhu Y, Zhang M, Yu H, Chen W, Qin J. A 3D human placenta-on-a-chip model to probe nanoparticle exposure at the placental barrier. *Toxicology in vitro : an international journal published in association with BIBRA*. Feb 2019;54:105-113. doi:10.1016/j.tiv.2018.08.014
76. Aengenheister L, Dugershaw BB, Manser P, et al. Investigating the accumulation and translocation of titanium dioxide nanoparticles with different surface modifications in static and dynamic human placental transfer models. *Eur J Pharm Biopharm*. Sep 2019;142:488-497. doi:10.1016/j.ejpb.2019.07.018
77. Puligandla PS, Skarsgard ED. The Canadian Pediatric Surgery Network Congenital Diaphragmatic Hernia Evidence Review Project: Developing national guidelines for care. *Paediatr Child Health*. May 2016;21(4):183-6. doi:10.1093/pch/21.4.183
78. Khoshgoo N, Kholdebarin R, Pereira-Terra P, et al. Prenatal microRNA miR-200b Therapy Improves Nitrofen-induced Pulmonary Hypoplasia Associated With Congenital Diaphragmatic Hernia. *Ann Surg*. May 2019;269(5):979-987. doi:10.1097/SLA.0000000000002595
79. Amberger JS, Bocchini CA, Scott AF, Hamosh A. OMIM.org: leveraging knowledge across phenotype-gene relationships. *Nucleic Acids Res*. Jan 08 2019;47(D1):D1038-D1043. doi:10.1093/nar/gky1151
80. Dobrowsky T, Gianni D, Pieracci J, Suh J. AAV manufacturing for clinical use: Insights on current challenges from the upstream process perspective. *Current Opinion in Biomedical Engineering*. 2021;20
81. Shirley JL, de Jong YP, Terhorst C, Herzog RW. Immune Responses to Viral Gene Therapy Vectors. *Mol Ther*. Mar 04 2020;28(3):709-722. doi:10.1016/j.ymthe.2020.01.001
82. Paunovska K, Loughrey D, Dahlman JE. Drug delivery systems for RNA therapeutics. *Nat Rev Genet*. May 2022;23(5):265-280. doi:10.1038/s41576-021-00439-4
83. Ren S, Wang M, Wang C, et al. Application of Non-Viral Vectors in Drug Delivery and Gene Therapy. *Polymers (Basel)*. Sep 28 2021;13(19)doi:10.3390/polym13193307
84. Hald Albertsen C, Kulkarni JA, Witzigmann D, Lind M, Petersson K, Simonsen JB. The role of lipid components in lipid nanoparticles for vaccines and gene therapy. *Adv Drug Deliv Rev*. Sep 2022;188:114416. doi:10.1016/j.addr.2022.114416
85. Patel V, Lalani R, Bardoliwala D, Ghosh S, Misra A. Lipid-Based Oral Formulation Strategies for Lipophilic Drugs. *AAPS PharmSciTech*. Nov 2018;19(8):3609-3630. doi:10.1208/s12249-018-1188-8
86. Akinc A, Maier MA, Manoharan M, et al. The Onpattro story and the clinical translation of nanomedicines containing nucleic acid-based drugs. *Nat Nanotechnol*. Dec 2019;14(12):1084-1087. doi:10.1038/s41565-019-0591-y
87. Schoenmaker L, Witzigmann D, Kulkarni JA, et al. mRNA-lipid nanoparticle COVID-19 vaccines: Structure and stability. *Int J Pharm*. May 15 2021;601:120586. doi:10.1016/j.ijpharm.2021.120586

88. Bajoria R, Contractor SF. Effect of the size of liposomes on the transfer and uptake of carboxyfluorescein by the perfused human term placenta. *J Pharm Pharmacol*. Jul 1997;49(7):675-81. doi:10.1111/j.2042-7158.1997.tb06091.x
89. Yang H, Sun C, Fan Z, et al. Effects of gestational age and surface modification on materno-fetal transfer of nanoparticles in murine pregnancy. *Sci Rep*. 2012;2:847. doi:10.1038/srep00847
90. Aengenheister L, Favaro RR, Morales-Prieto DM, et al. Research on nanoparticles in human perfused placenta: State of the art and perspectives. *Placenta*. Jan 15 2021;104:199-207. doi:10.1016/j.placenta.2020.12.014
91. Bao Z, Bufton J, Hickman RJ, Aspuru-Guzik A, Bannigan P, Allen C. Revolutionizing drug formulation development: The increasing impact of machine learning. *Adv Drug Deliv Rev*. Nov 2023;202:115108. doi:10.1016/j.addr.2023.115108
92. Bao Z, Yung F, Hickman RJ, Aspuru-Guzik A, Bannigan P, Allen C. Data-driven development of an oral lipid-based nanoparticle formulation of a hydrophobic drug. *Drug Deliv Transl Res*. Jul 2024;14(7):1872-1887. doi:10.1007/s13346-023-01491-9
93. Dugershaw BB, Aengenheister L, Hansen SSK, Hougaard KS, Buerki-Thurnherr T. Recent insights on indirect mechanisms in developmental toxicity of nanomaterials. *Part Fibre Toxicol*. Jul 11 2020;17(1):31. doi:10.1186/s12989-020-00359-x
94. Mostafaei SH, Tanha J. OUBoost: boosting based over and under sampling technique for handling imbalanced data. *International Journal of Machine Learning and Cybernetics*. 2023/10/01 2023;14(10):3393-3411. doi:10.1007/s13042-023-01839-0
95. Miyake Y, Tse WH, Wang JQ, et al. The effect of tracheal occlusion in congenital diaphragmatic hernia in the nitrofen rat lung explant model. *Pediatr Surg Int*. Dec 23 2022;39(1):61. doi:10.1007/s00383-022-05340-7
96. Miyake Y, Tse WH, Wang JQ, et al. Microinjection With Nanoparticles to Deliver Drugs in Prenatal Lung Explants - A Pilot Study for Prenatal Therapy in Congenital Diaphragmatic Hernia. *J Pediatr Surg*. May 2024;59(5):847-853. doi:10.1016/j.jpedsurg.2024.01.046
97. Chen X, Lv H. Intelligent control of nanoparticle synthesis on microfluidic chips with machine learning. *NPG Asia Materials*. 2022/08/12 2022;14(1):69. doi:10.1038/s41427-022-00416-1
98. Geisler HC, Ghalsasi AA, Safford HC, et al. EGFR-targeted ionizable lipid nanoparticles enhance in vivo mRNA delivery to the placenta. *J Control Release*. Jun 10 2024;371:455-469. doi:10.1016/j.jconrel.2024.05.036
99. Cohen ZR, Ramishetti S, Peshes-Yaloz N, et al. Localized RNAi therapeutics of chemoresistant grade IV glioma using hyaluronan-grafted lipid-based nanoparticles. *ACS Nano*. Feb 24 2015;9(2):1581-91. doi:10.1021/nn506248s
100. Ramishetti S, Kedmi R, Goldsmith M, et al. Systemic Gene Silencing in Primary T Lymphocytes Using Targeted Lipid Nanoparticles. *ACS Nano*. Jul 28 2015;9(7):6706-16. doi:10.1021/acsnano.5b02796
101. Lundberg SM, Erion G, Chen H, et al. From Local Explanations to Global Understanding with Explainable AI for Trees. *Nat Mach Intell*. Jan 2020;2(1):56-67. doi:10.1038/s42256-019-0138-9
102. Zhou Z, Luo D, Li M, et al. A Novel Multicellular Placental Barrier Model to Investigate the Effect of Maternal Aflatoxin B. *Toxins (Basel)*. Apr 27 2023;15(5)doi:10.3390/toxins15050312
103. Kouthouridis S, Sotra A, Khan Z, Alvarado J, Raha S, Zhang B. Modeling the Progression of Placental Transport from Early- to Late-Stage Pregnancy by Tuning Trophoblast Differentiation and Vascularization. *Adv Healthc Mater*. Dec 2023;12(32):e2301428. doi:10.1002/adhm.202301428
104. Huang X, Lüthi M, Ontsouka EC, et al. Establishment of a confluent monolayer model with human primary trophoblast cells: novel insights into placental glucose transport. *Mol Hum Reprod*. Jun 2016;22(6):442-56. doi:10.1093/molehr/gaw018

105. Wong MK, Li EW, Adam M, Selvaganapathy PR, Raha S. Establishment of an in vitro placental barrier model cultured under physiologically relevant oxygen levels. *Mol Hum Reprod*. May 15 2020;26(5):353-365. doi:10.1093/molehr/gaaa018
106. Vaughn DE, Bjorkman PJ. Structural basis of pH-dependent antibody binding by the neonatal Fc receptor. *Structure*. Jan 15 1998;6(1):63-73. doi:10.1016/s0969-2126(98)00008-2
107. Clements T, Rice TF, Vamvakas G, et al. Update on Transplacental Transfer of IgG Subclasses: Impact of Maternal and Fetal Factors. *Front Immunol*. 2020;11:1920. doi:10.3389/fimmu.2020.01920
108. Labouta HI, Menina S, Kochut A, et al. Bacteriomimetic invasin-functionalized nanocarriers for intracellular delivery. *J Control Release*. 12/28/ 2015;220, Part A:414-424. doi:http://dx.doi.org/10.1016/j.jconrel.2015.10.052
109. Wang S, Wei X, Sun X, et al. A novel therapeutic strategy for cartilage diseases based on lipid nanoparticle-RNAi delivery system. *Int J Nanomedicine*. 2018;13:617-631. doi:10.2147/IJN.S142797
110. Mattson MP. Hormesis defined. *Ageing Res Rev*. Jan 2008;7(1):1-7. doi:10.1016/j.arr.2007.08.007
111. Wei X, Shao B, He Z, et al. Cationic nanocarriers induce cell necrosis through impairment of Na(+)/K(+)-ATPase and cause subsequent inflammatory response. *Cell Res*. Feb 2015;25(2):237-53. doi:10.1038/cr.2015.9
112. Hanafy MS, Dao HM, Xu H, Koleng JJ, Sakran W, Cui Z. Effect of the amount of cationic lipid used to complex siRNA on the cytotoxicity and proinflammatory activity of siRNA-solid lipid nanoparticles. *Int J Pharm X*. Dec 15 2023;6:100197. doi:10.1016/j.ijpx.2023.100197
113. Martinez DR, Fong Y, Li SH, et al. Fc Characteristics Mediate Selective Placental Transfer of IgG in HIV-Infected Women. *Cell*. Jun 27 2019;178(1):190-201.e11. doi:10.1016/j.cell.2019.05.046
114. Gruber MM, Hirschmugl B, Berger N, et al. Plasma proteins facilitates placental transfer of polystyrene particles. *J Nanobiotechnology*. Sep 09 2020;18(1):128. doi:10.1186/s12951-020-00676-5
115. Pridgen EM, Alexis F, Kuo TT, et al. Transepithelial transport of Fc-targeted nanoparticles by the neonatal fc receptor for oral delivery. *Sci Transl Med*. Nov 27 2013;5(213):213ra167. doi:10.1126/scitranslmed.3007049
116. Ducry L. *Antibody-drug conjugates*. Methods in molecular biology,. Humana Press ; Springer; 2013:x, 317 p.
117. Okyem S, Awotunde O, Ogunlusi T, Riley MB, Driskell JD. High-Affinity Points of Interaction on Antibody Allow Synthesis of Stable and Highly Functional Antibody-Gold Nanoparticle Conjugates. *Bioconjug Chem*. Aug 18 2021;32(8):1753-1762. doi:10.1021/acs.bioconjchem.1c00261
118. Jue R, Lambert JM, Pierce LR, Traut RR. Addition of sulfhydryl groups to Escherichia coli ribosomes by protein modification with 2-iminothiolane (methyl 4-mercaptobutyrimidate). *Biochemistry*. Dec 12 1978;17(25):5399-406. doi:10.1021/bi00618a013
119. Escareño N, Hassan N, Kogan MJ, Juárez J, Topete A, Daneri-Navarro A. Microfluidics-assisted conjugation of chitosan-coated polymeric nanoparticles with antibodies: Significance in drug release, uptake, and cytotoxicity in breast cancer cells. *J Colloid Interface Sci*. Jun 2021;591:440-450. doi:10.1016/j.jcis.2021.02.031
120. Cuatrecasas P, Parikh I. Adsorbents for affinity chromatography. Use of N-hydroxysuccinimide esters of agarose. *Biochemistry*. Jun 06 1972;11(12):2291-9. doi:10.1021/bi00762a013
121. Berg EA, Fishman JB. Labeling Antibodies. *Cold Spring Harb Protoc*. Jul 01 2020;2020(7):099242. doi:10.1101/pdb.top099242

122. Anselmo AC, Mitragotri S. Nanoparticles in the clinic: An update. *Bioeng Transl Med*. Sep 2019;4(3):e10143. doi:10.1002/btm2.10143
123. Waggoner LE, Miyasaki KF, Kwon EJ. Analysis of PEG-lipid anchor length on lipid nanoparticle pharmacokinetics and activity in a mouse model of traumatic brain injury. *Biomater Sci*. Jun 13 2023;11(12):4238-4253. doi:10.1039/d2bm01846b
124. Ryals RC, Patel S, Acosta C, McKinney M, Pennesi ME, Sahay G. The effects of PEGylation on LNP based mRNA delivery to the eye. *PLoS One*. 2020;15(10):e0241006. doi:10.1371/journal.pone.0241006
125. Yue T, Zhou H, Sun H, et al. Why are nanoparticles trapped at cell junctions when the cell density is high? *Nanoscale*. Apr 04 2019;11(14):6602-6609. doi:10.1039/c9nr01024f
126. Renaud SJ, Jeyarajah MJ. How trophoblasts fuse: an in-depth look into placental syncytiotrophoblast formation. *Cell Mol Life Sci*. Jul 20 2022;79(8):433. doi:10.1007/s00018-022-04475-z
127. Zhang B, Liang R, Zheng M, Cai L, Fan X. Surface-Functionalized Nanoparticles as Efficient Tools in Targeted Therapy of Pregnancy Complications. *Int J Mol Sci*. Jul 25 2019;20(15)doi:10.3390/ijms20153642
128. Kloet SK, Walczak AP, Louisse J, et al. Translocation of positively and negatively charged polystyrene nanoparticles in an in vitro placental model. *Toxicol In Vitro*. Oct 2015;29(7):1701-10. doi:10.1016/j.tiv.2015.07.003
129. Ouyang B, Poon W, Zhang YN, et al. The dose threshold for nanoparticle tumour delivery. *Nat Mater*. Dec 2020;19(12):1362-1371. doi:10.1038/s41563-020-0755-z
130. Mui BL, Tam YK, Jayaraman M, et al. Influence of Polyethylene Glycol Lipid Desorption Rates on Pharmacokinetics and Pharmacodynamics of siRNA Lipid Nanoparticles. *Mol Ther Nucleic Acids*. Dec 17 2013;2(12):e139. doi:10.1038/mtna.2013.66
131. Labouta HI, Sarsons C, Kennard J, et al. Understanding and improving assays for cytotoxicity of nanoparticles: what really matters? 10.1039/C8RA03849J. *RSC Advances*. 2018;8(41):23027-23039. doi:10.1039/C8RA03849J
132. Labouta HI, Kraus T, El-Khordagui LK, Schneider M. Combined multiphoton imaging-pixel analysis for semiquantitation of skin penetration of gold nanoparticles. *International journal of pharmaceutics*. 7/15/ 2011;413(1–2):279-282. doi:http://dx.doi.org/10.1016/j.ijpharm.2011.03.067
133. Young RE, Nelson KM, Hofbauer SI, et al. Systematic development of ionizable lipid nanoparticles for placental mRNA delivery using a design of experiments approach. *Bioact Mater*. Apr 2024;34:125-137. doi:10.1016/j.bioactmat.2023.11.014
134. Zhu Y, Shen R, Vuong I, et al. Multi-step screening of DNA/lipid nanoparticles and co-delivery with siRNA to enhance and prolong gene expression. *Nat Commun*. Jul 25 2022;13(1):4282. doi:10.1038/s41467-022-31993-y
135. Chaudhary N, Newby AN, Arral ML, et al. Lipid nanoparticle structure and delivery route during pregnancy dictate mRNA potency, immunogenicity, and maternal and fetal outcomes. *Proc Natl Acad Sci U S A*. Mar 12 2024;121(11):e2307810121. doi:10.1073/pnas.2307810121
136. Dugershaw-Kurzer B, Bossart J, Buljan M, et al. Nanoparticles Dysregulate the Human Placental Secretome with Consequences on Angiogenesis and Vascularization. *Adv Sci (Weinh)*. May 20 2024:e2401060. doi:10.1002/advs.202401060
137. Brentnall M, Rodriguez-Menocal L, De Guevara RL, Cepero E, Boise LH. Caspase-9, caspase-3 and caspase-7 have distinct roles during intrinsic apoptosis. *BMC Cell Biol*. Jul 09 2013;14:32. doi:10.1186/1471-2121-14-32
138. Cui S, Wang Y, Gong Y, et al. Correlation of the cytotoxic effects of cationic lipids with their headgroups. *Toxicol Res (Camb)*. May 08 2018;7(3):473-479. doi:10.1039/c8tx00005k

139. Yu Q, Qiu Y, Wang X, et al. Efficient siRNA transfer to knockdown a placenta specific lncRNA using RGD-modified nano-liposome: A new preeclampsia-like mouse model. *International journal of pharmaceutics*. Jul 30 2018;546(1-2):115-124. doi:10.1016/j.ijpharm.2018.05.001
140. Zhang B, Cheng G, Zheng M, et al. Targeted delivery of doxorubicin by CSA-binding nanoparticles for choriocarcinoma treatment. *Drug delivery*. 2018;25(1):461-471. doi:10.1080/10717544.2018.1435750
141. Shojaei S, Ali MS, Suresh M, et al. Dynamic placenta-on-a-chip model for fetal risk assessment of nanoparticles intended to treat pregnancy-associated diseases. *Biochimica et Biophysica Acta (BBA) - Molecular Basis of Disease*. 2021/07/01/ 2021;1867(7):166131. doi:https://doi.org/10.1016/j.bbadis.2021.166131
142. Anselmo AC, Mitragotri S. Nanoparticles in the clinic: An update. *Bioeng Transl Med*. 2019;4(3):e10143. doi:10.1002/btm2.10143
143. Griffiths SK, Campbell JP. Placental structure, function and drug transfer. *BJA Education*. 2014;15(2):84-89. doi:10.1093/bjaceaccp/mku013
144. Mansilla M, Wang Y, Lim R, Palmer K, Nie G. HtrA4 is up-regulated during trophoblast syncytialization and BeWo cells fail to syncytialize without HtrA4. *Scientific Reports*. 2021/07/13 2021;11(1):14363. doi:10.1038/s41598-021-93520-1
145. Wang R, Dang Y-L, Zheng R, et al. Live Cell Imaging of In Vitro Human Trophoblast Syncytialization1. *Biology of Reproduction*. 2014;90(6)doi:10.1095/biolreprod.113.114892
146. FAIMAN C, RYAN RJ, ZWIREK SJ, RUBIN ME. Serum FSH and HCG During Human Pregnancy and Puerperium1. *The Journal of Clinical Endocrinology & Metabolism*. 1968;28(9):1323-1329. doi:10.1210/jcem-28-9-1323
147. Conings S, Amant F, Annaert P, Van Calsteren K. Integration and validation of the ex vivo human placenta perfusion model. *Journal of Pharmacological and Toxicological Methods*. 2017/11/01/ 2017;88:25-31. doi:https://doi.org/10.1016/j.vascn.2017.05.002
148. Ingber DE. Human organs-on-chips for disease modelling, drug development and personalized medicine. *Nature Reviews Genetics*. 2022/03/25 2022;doi:10.1038/s41576-022-00466-9
149. Bhise NS, Ribas J, Manoharan V, et al. Organ-on-a-chip platforms for studying drug delivery systems. *Journal of controlled release : official journal of the Controlled Release Society*. Sep 28 2014;190:82-93. doi:10.1016/j.jconrel.2014.05.004
150. Folch i Folch A. *Introduction to bioMEMS*. CRC Press; 2013:xxxv, 492 p.
151. Ahadian S, Civitarese R, Bannerman D, et al. Organ-On-A-Chip Platforms: A Convergence of Advanced Materials, Cells, and Microscale Technologies. *Advanced healthcare materials*. Jan 2018;7(2)doi:10.1002/adhm.201700506
152. Yesil-Celiktas O, Hassan S, Miri AK, et al. Mimicking Human Pathophysiology in Organ-on-Chip Devices. *Advanced Biosystems*. 2018;2(10):1800109. doi:10.1002/adbi.201800109
153. Working PK, Newman MS, Huang SK, Mayhew E, Vaage J, Lasic DD. Pharmacokinetics, Biodistribution and Therapeutic Efficacy of Doxorubicin Encapsulated in Stealth® Liposomes (Doxil®). *Journal of Liposome Research*. 1994/01/01 1994;4(1):667-687. doi:10.3109/08982109409037065
154. Gabizon A, Shmeeda H, Barenholz Y. Pharmacokinetics of Pegylated Liposomal Doxorubicin. *Clinical Pharmacokinetics*. 2003/04/01 2003;42(5):419-436. doi:10.2165/00003088-200342050-00002
155. Almeida B, Nag OK, Rogers KE, Delehanty JB. Recent Progress in Bioconjugation Strategies for Liposome-Mediated Drug Delivery. *Molecules*. Dec 1 2020;25(23)doi:10.3390/molecules25235672

156. Gupta SK, Malhotra SS, Malik A, Verma S, Chaudhary P. Cell Signaling Pathways Involved During Invasion and Syncytialization of Trophoblast Cells. *American Journal of Reproductive Immunology*. 2016;75(3):361-371. doi:https://doi.org/10.1111/aji.12436
157. Gardiner C, Ferreira YJ, Dragovic RA, Redman CWG, Sargent IL. Extracellular vesicle sizing and enumeration by nanoparticle tracking analysis. *Journal of Extracellular Vesicles*. 2013/01/01 2013;2(1):19671. doi:10.3402/jev.v2i0.19671
158. Brugger BA, Guettler J, Gauster M. Go with the Flow-Trophoblasts in Flow Culture. *Int J Mol Sci*. 2020;21(13):4666. doi:10.3390/ijms21134666
159. James JL, Saghian R, Perwick R, Clark AR. Trophoblast plugs: impact on utero-placental haemodynamics and spiral artery remodelling. *Human Reproduction*. 2018;33(8):1430-1441. doi:10.1093/humrep/dey225
160. Leonard F, Collnot E-M, Lehr C-M. A Three-Dimensional Coculture of Enterocytes, Monocytes and Dendritic Cells To Model Inflamed Intestinal Mucosa in Vitro. *Molecular Pharmaceutics*. 2010/12/06 2010;7(6):2103-2119. doi:10.1021/mp1000795
161. Blundell C, Tess ER, Schanzer ASR, et al. A microphysiological model of the human placental barrier. *Lab Chip*. 2016;16(16):3065-3073. doi:10.1039/c6lc00259e
162. Pidoux G, Gerbaud P, Gnidehou S, et al. ZO-1 is involved in trophoblastic cell differentiation in human placenta. *American Journal of Physiology-Cell Physiology*. 2010;298(6):C1517-C1526. doi:10.1152/ajpcell.00484.2008
163. Jansen CHJR, Kastelein AW, Kleinrouweler CE, et al. Development of placental abnormalities in location and anatomy. *Acta Obstetricia et Gynecologica Scandinavica*. 2020;99(8):983-993. doi:https://doi.org/10.1111/aogs.13834
164. Li L, Yang H, Chen P, et al. Trophoblast-Targeted Nanomedicine Modulates Placental sFLT1 for Preeclampsia Treatment. *Front Bioeng Biotechnol*. 2020;8:64-64. doi:10.3389/fbioe.2020.00064
165. Costa MA. Scrutinising the regulators of syncytialization and their expression in pregnancy-related conditions. *Molecular and Cellular Endocrinology*. 2016/01/15/ 2016;420:180-193. doi:https://doi.org/10.1016/j.mce.2015.11.010
166. Morley LC, Beech DJ, Walker JJ, Simpson NAB. Emerging concepts of shear stress in placental development and function. *Molecular Human Reproduction*. 2019;25(6):329-339. doi:10.1093/molehr/gaz018
167. Miura S, Sato K, Kato-Negishi M, Teshima T, Takeuchi S. Fluid shear triggers microvilli formation via mechanosensitive activation of TRPV6. *Nature Communications*. 2015/11/13 2015;6(1):8871. doi:10.1038/ncomms9871
168. Drasler B, Vanhecke D, Rodriguez-Lorenzo L, Petri-Fink A, Rothen-Rutishauser B. Quantifying nanoparticle cellular uptake: which method is best? *Nanomedicine (Lond)*. May 2017;12(10):1095-1099. doi:10.2217/nnm-2017-0071
169. Gregoriadis G, Florence AT. Liposomes in Drug Delivery. *Drugs*. 1993/01/01 1993;45(1):15-28. doi:10.2165/00003495-199345010-00003
170. Jahn A, Vreeland WN, Gaitan M, Locascio LE. Controlled Vesicle Self-Assembly in Microfluidic Channels with Hydrodynamic Focusing. *Journal of the American Chemical Society*. 2004/03/01 2004;126(9):2674-2675. doi:10.1021/ja0318030
171. Baby T, Liu Y, Middelberg APJ, Zhao C-X. Fundamental studies on throughput capacities of hydrodynamic flow-focusing microfluidics for producing monodisperse polymer nanoparticles. *Chemical Engineering Science*. 2017/09/21/ 2017;169:128-139. doi:https://doi.org/10.1016/j.ces.2017.04.046
172. Ran R, Middelberg APJ, Zhao CX. Microfluidic synthesis of multifunctional liposomes for tumour targeting. *Colloids and surfaces B, Biointerfaces*. Dec 1 2016;148:402-410. doi:10.1016/j.colsurfb.2016.09.016

173. Danaei M, Dehghankhold M, Ataei S, et al. Impact of Particle Size and Polydispersity Index on the Clinical Applications of Lipidic Nanocarrier Systems. *Pharmaceutics*. 2018;10(2):57. doi:10.3390/pharmaceutics10020057
174. Zhang B, Tan L, Yu Y, et al. Placenta-specific drug delivery by trophoblast-targeted nanoparticles in mice. *Theranostics*. 2018;8(10):2765-2781. doi:10.7150/thno.22904
175. Hu R, Jin H, Zhou S, Yang P, Li X. Proteomic Analysis of Hypoxia-Induced Responses in the Syncytialization of Human Placental Cell Line BeWo. *Placenta*. 2007/05/01/ 2007;28(5):399-407. doi:https://doi.org/10.1016/j.placenta.2006.07.005
176. Moore KH, Murphy HA, Chapman H, George EM. Syncytialization alters the extracellular matrix and barrier function of placental trophoblasts. *American Journal of Physiology-Cell Physiology*. 2021;321(4):C694-C703. doi:10.1152/ajpcell.00177.2021
177. Liu F, Soares MJ, Audus KL. Permeability properties of monolayers of the human trophoblast cell line BeWo. *American Journal of Physiology-Cell Physiology*. 1997;273(5):C1596-C1604. doi:10.1152/ajpcell.1997.273.5.C1596
178. Shao X, Cao G, Chen D, et al. Placental trophoblast syncytialization potentiates macropinocytosis via mTOR signaling to adapt to reduced amino acid supply. *Proceedings of the National Academy of Sciences*. 2021;118(3):e2017092118. doi:doi:10.1073/pnas.2017092118
179. Zhang Q, Schulenborg T, Tan T, Lang B, Friauf E, Fecher-Trost C. Proteome analysis of a plasma membrane-enriched fraction at the placental feto-maternal barrier. *PROTEOMICS – Clinical Applications*. 2010;4(5):538-549. doi:https://doi.org/10.1002/prca.200900048
180. Agbor-Enoh ST, Achur RN, Valiyaveettil M, Leke R, Taylor DW, Gowda DC. Chondroitin sulfate proteoglycan expression and binding of Plasmodium falciparum-infected erythrocytes in the human placenta during pregnancy. *Infection and immunity*. 2003;71(5):2455-2461. doi:10.1128/IAI.71.5.2455-2461.2003
181. Foroozandeh P, Aziz AA. Insight into Cellular Uptake and Intracellular Trafficking of Nanoparticles. *Nanoscale Research Letters*. 2018/10/25 2018;13(1):339. doi:10.1186/s11671-018-2728-6
182. Li Y, Yu X-G, Fu J-J. Involvement of nephrin in human placental trophoblast syncytialization. 2015;